Behavior of laterally loaded piles in natural sandy gravels

Jagodnik, Vedran

Doctoral thesis / Disertacija

2014

Permanent link / Trajna poveznica: https://urn.nsk.hr/urn:nbn:hr:188:679713

Download date / Datum preuzimanja: **2025-02-20**

Repository / Repozitorij:

Repository of the University of Rijeka Library - SVKRI Repository

UNIVERSITY OF RIJEKA

FACULTY OF CIVIL ENGINEERING

Vedran Jagodnik

BEHAVIOR OF LATERALLY LOADED PILES IN NATURAL SANDY GRAVELS

DOCTORAL THESIS

Supervisor: prof. dr. sc. Željko Arbanas

Rijeka, 2014.

Mentor: prof. dr. sc. Željko Arbanas

Doktorski rad obranjen je dana _____

u/na _____, pred povjerenstvom u sastavu:

1. Izv. prof. dr. sc. Leo Matešić, Sveučilište u Rijeci, Građevinski fakultet, predsjednik povjerenstva

2. Izv. prof. dr. sc. Željko Arbanas, Sveučilište u Rijeci, Građevinski fakultet, član mentor

3. Prof. dr. sc. Meho - Saša Kovačević, Sveučilište u Zagrebu, Građevinski fakultet, vanjski član

Abstract

Field testing of laterally loaded single piles and group of piles in natural sandy gravels is presented. Testing is performed on monotonically loaded single pile, cyclicly loaded single pile, group of *2 by 1* piles monotonically loaded and group of *2 by 3* piles monotonically loaded. During the field testing, pile deflections were measured using inclinometer probe, which was placed in inclinometer casings installed in pile axis. Tests are performed for establishment of pile behaviour in natural sandy gravels and to try to depict the influence of dilatancy, in this type of soil material. Soil is tested in large direct shear box in order to obtain strength parameters needed for calculation of *p-y* curves proposed by Reese and Van Impe and for numerical analysis, by using simple *Mohr-Coulomb* and *Drucker-Prager* constitutive models.

Piles are loaded with hydraulic press, counter-bracing the massive concrete block, which will transfer the load on a steel frame and pile heads thus pulling the piles away from concrete block. Performed tests can be described as displacement control tests. Piles are displaced in increments of 2mm while the force on hydraulic press will be read out for each increment.

Measured results are compared with results of numerical analyses performed using Rocscience RS3 software package. Pile and soil material are described using Mohr-Coulomb constitutive material using associated and non-associated flow behaviours for soil material.

Based on field tests and numerical analyses, the conclusions and further research in the field of laterally loaded piles in coarse-grain material are presented.

Sažetak

U radu su prikazana terenska ispitivanja na horizontalo opterećenim pilotima izvedenim u prirodnim pjeskovitim šljuncima. Ispitivanja su provedena na jednom monotono opterećenom pilotu, jednom ciklički opterećenom pilotu, grupi od dva monotono opterećena pilota u nizu (dva reda i jedan stupac) i grupi od šest monotono opterećenih pilota (dva reda i tri stupca). Tijekom ispitivanja deformacije pilota mjerene su inklinometarskom sondom, koja se upuštala u inklinometarsku cijev izvedenu kroz uzdužnu os pilota. Ispitivanja su provedena kako bi se dobio uvid u ponašanje pilota u prirodnim pjeskovitim šljuncima te da li na ponašanje utječe dilatancija, u ovakvom materijalu. Materijal je ispitan smicanjem u velikom aparatu za izravan posmik kako bi se dobili parametri čvrstoće potrebni za proračun *p-y* krivulja prema Reesu i Van Impeu, ali i za primjenu numeričkog modela, korištenjem konstitutivnih modela prema *Mohr-Coulombu* ili *Drucker-Prageru*.

Piloti su opterećeni hidrauličkom prešom, razuprtom o masivni betonski blok, te prenoseći opterećenje na glave pilota čime se piloti pomiču od betonskog bloka. Ispitivanja se mogu okarakterizirati kao ispitivanja s kontroliranim pomakom. Piloti su pomicani u inkrementima od 2mm, a sila na preši se očitavala za svaki inkrement.

Dobiveni rezultati mjerenjem usporedeni su s rezultatima numeričkih analiza dobivenih korištenjem Rocsceience programskog paketa RS3. Pilot i materijal tla opisani su Mohr-Coulombovim konstitutivnim zakonom uz korištenje pridruženog i nepridruženog tečenja kod opisivanja ponašanja tla.

Na osnovu in-situ ispitanih pilota i provedenih numeričkih analiza dani su zaključci te preporuke za daljnja istraživanja o ponašanju horizontalno opterećenih pilota u krupnozrnatim materijalima.

Acknowledgements

Contents

Appendices

List of Figures

List of Tables

Abbreviations

ABS	**A**crylonitrile on **B**utadiene **S**tyrene
BEF	**B**eam on **E**lastic **F**oundation
CEI	**C**ivil on **E**ngineering **I**nstitute
ECM	**E**lastic **C**ontinuum **M**ethod
FDM	**F**inite **D**ifference **M**ethod
FEA	**F**inite **E**lement **A**nalysis
FEM	**F**inite **E**lement **M**ethod
LLP	**L**aterally **L**oaded **P**iles
MASW	**M**ultichannel **A**nalysis of **S**urface **W**aves
PDE	**P**artial **D**ifferential **E**quation
SSI	**S**oil **S**tructure **I**nteraction
USR	**U**ltimate **S**oil **R**esistance

Symbols

d	pile diameter	m
f_{uH}	flexibility coefficient for displacements due to horizontal force	m/kN
f_{uM}	flexibility coefficient for displacements due to bending moment	$1/kN$
$f_{\theta H}$	flexibility coefficient for rotations due to horizontal force	$rads/kN$
$f_{\theta M}$	flexibility coefficient for rotations due to bending moment	$rads/kNm$
k, k_{py}	modulus of subgrade reaction	kN/m^3
k_0	coefficient of lateral earth pressure at rest	

$$k_0 = 1 - \sin\phi$$

k_a	coefficient of active earth pressure according to Rankine	

$$k_a = \tan^2(45° - \tfrac{\phi}{2})$$

k_h	coefficient of horizontal subgrade reaction	kN/m^3
k_p	coefficient of passive earth pressure according to Rankine	

$$k_p = \tan^2(45° + \tfrac{\phi}{2})$$

k_s	coeffcient of earth pressure along the side of the pile group	

$$k_s = (1 - \sin\phi)\tan\phi$$

m	slope of the line between points defined by ultimate soil resistance above and below water	
n	exponential of parabolic part of *p-y* curve	
p	parabolic part of *p-y* curve	
p_m	ultimate soil resistance for depth below water	kPa
p_{st}	ultimate resistance of the soil at some depth D	kPa
p_{sd}	ultimate resistance of the soil at grater depth	kPa
p_{ult}	ultimate soil resistance for depth above water	kPa

q_u	uniaxial compressive strength	kPa
u_{GL}	horizontal displacement of pile head at ground level	m
y_k	starting part of *p-y* curve	m
$\overline{A}$	dimensionless coefficient for ultimate resistance	
$\overline{B}$	dimensionless coefficient for ultimate resistance	
C_c	coefficient of gradation	
C_u	coefficient of uniformity	
D	pile diameter	m
E	Young's modulus of pile material	kPa
E_s	Young's modulus of soil material	kPa
H	horizontal force at the pile head	kN
I	moment of inertia	m^4
K_{RS}	coefficient of flexural rigidity	
	$K_{RS} = \frac{EI}{EsL^4}$	
L	length of pile	m
L_{ell}	effective length of pile	m
M	bending moment at the pile head	kNm
$Q_{L,r}$	ultimate lateral force for rigid pile	kN
$Q_{L,f}$	ultimate lateral force for flexible pile	kN
γ	unit weight of the soil	kN/m^3
ϕ	angle of soil friction	$degrees\ °$
ψ	angle of soil dilatancy	$degrees\ °$
θ_{GL}	rotation of pile head at the ground level	$rads$

. . .

Chapter 1

Introduction

1.1 Short introduction to the Thesis

The use of shallow foundation in geotechnical engineering as a foundation solution is often impossible because of low bearing capacity and high soil deformability in near surface area. The alternative is to use some type of deep foundation construction. One of the types of foundation that transfers high stresses into deeper layers of soil continuum is pile foundation. Pile foundation is often described as a column like construction embedded in soil that transfers axial force from buildings to a soil with higher bearing capacity and lower deformability, achieving higher load capacity and bridging the high deformability soil. But because of the wind, earthquake and water waves on various constructions, piles are also subjected to horizontal, or lateral, forces. So, to fully determine the load capacity of a pile it is necessary to take into consideration the lateral behaviour of a pile, as well as lateral capacity.

Lateral testing of piles started in the 1960-es and was further tested in 1970-es. The theory of laterally loaded piles (herein **LLP**) is based on analytical theory of a beam on elastic foundation (herein **BEF**) [1]. Based on **BEF**, Poulous [2, 3] used finite difference method (herein **FDM**) to solve differential equation of the **LLP** balance and with that established the procedure how to use simple elastic analysis to obtain displacements of a laterally loaded pile. Two of the most significant papers are Reese et al. [4] and Cox et al. [5]. Based on these papers authors were suggesting the use of *p - y* curves as a procedure to dimensioning piles that will be subjected to lateral forces. The *p-y* curves are describing the

non-linear behaviour of soil resistance *p* versus pile displacement *y*. Based on tests conducted by Reese et al. [4] and Cox et al. [5], they developed equations for determining *p* - *y* curves for both clays and sands [6]. With development of technology and computers, the use of more advanced numerical methods, such as finite element method (herein **FEM**), are started to be used. Modelling a non-linear behaviour of soil and construction is becoming widely used. Basic Winkler's soil model is replaced with continuum and elastic - plastic soil models, like Mohr - Coulomb and Drucker - Prager models [7, 8].

Some of the authors used the possibility to model an interaction between piles and soil [9, 10, 11] which gave an insight into better understanding what is the soil-structure interaction (herein **SSI**) behaviour. Because of that, and the fact that the field testing is expensive, **FEM** is starting to be more and more used for determining *p* - *y* curves. The use of numerical modelling in two dimensions was widely spread but it couldn't capture the proper behaviour of an *out-of-plane* behaviour of pile, as it mentioned by Brødbæk et al. [12]. To fully emphasize the behaviour of pile and piles group, the full numerical analysis is necessary, which means the use of three dimensional modelling. Three dimensional modelling gives the opportunity to model group behaviour of **LLP** and their mutual interaction. Some minor disadvantages of three dimensional analysis are time and computer memory consuming. Some of authors like Koojiman [13] and Pavlovec [14] are modelling only the ground level, because at that point the soil will yield relatively quickly at small displacements. Present day, the high performance computers are giving us the possibility to conduct any kind of analysis very quickly, using two or three dimensional continuum model, and linear or non-linear material behaviour [8, 10, 11, 15].

Until now, simple constitutive models have been used. It is advisable to use constitutive models that can fully describe the behaviour of soil subjected to lateral pile loading. Two of the most widely used constitutive models, the Mohr-Coulomb model and Drucker-Prager model, could have a problem with describing real behaviour, especially if the volumetric behaviour of soil, like dilatancy, has significant influence. Fan et al. [16] showed that neglecting dilatancy behaviour of a soil material could have the increase of 50% in ultimate pile resistance, which is not neglectful.

Pile itself can be modelled as a continuum, and as beam elements. Very often it's modelled as continuum model [11, 17]. When using beam theory to represent a pile behaviour then the Euler-Bernoulli's theory beam is mostly used

[2, 6]. Using the Euler-Bernoulli's beam theory, the influence of shear force is neglected and the displacements can be smaller than the real ones, especially for large diameter piles. To cope with that issue, it is better to use Timoshenko's beam theory [18, 19]. Unlike Euler-Bernoulli's beam theory which has an assumption that after deformation, plane cross-section does not rotate, Timoshenko's beam theory takes into account that rotation which results additional shear forces and thus deformation.

1.2   Content of Thesis

The content of this Thesis can be divided into three parts. The first part is the theory part, showing the basic principles of laterally loaded piles and way of solving them. Chapter 2 Previous research of LLP and Chapter 3 Basic theory of laterally loaded piles behaviour in cohesionless soils are dealing with previous research regarding laterally loaded piles behaviour and basic theory of beam on elastic half-space, respectively. The laterally loaded piles field test planning and construction are presented in the second part of the Thesis, so as the results of performed field testing. In Chapter 4 Geotechnical test site characterization the location of field testing is described, and in Chapter 5 Experimental programme establishment of testing field is presented; how the piles and concrete counterweight block were constructed, and how the measurements using inclinometer probe were carried out during the testing. Chapter 6 Field test results presents results and analyses derived from the measurement results of testing of the mentioned piles. The third part of the Thesis consists of numerical comparison with field tests. Three dimensional numerical analysis is used and compared with field tests, which is presented in Chapter 7 Back analysis of LLP behaviour using FEM. In Chapter 8 Conclusions, short summary of presented research with commented results and ideas for further research are presented. Brief introduction in The Cesáro Sum-Technique, Loading Frame Joint Connections and Elements Calculation, Seismic refraction and Multichannel analysis of surface waves (MASW) are presented in research Appendices.

1.3 Hypothesis

Based on some preliminary research, the soil at the location of testing field is characterised as very dense natural sandy gravels. Due to previous large compaction during the shearing the cohesionless material can show the behaviour of dilatancy, which can be described as an increase in volume due to soil particles rearrangements. Because of dilatancy in soil, some additional strains may occur leading to larger ultimate load of laterally loaded pile. From this basic assumptions, the hypothesis can be defined as: *piles in natural sandy gravels exposed to lateral loads would show some influence of dilatancy in their behaviour*.

Chapter 2

Previous research of LLP

This chapter consists of an overview of some previous studies in which testing of laterally loaded piles were conducted. Cited papers are dealing with slender piles embedded in cohesionless soil, while pile material varies from study to study. Piles were constructed as a free-headed piles, and they are tested with applying of monotonic lateral loads, although there are some studies that analyses cyclic lateral loading of piles.

Chapter is divided into two sections. In the first section, studies regarding research on single piles have been analysed, while in the second section, group of piles behaviour has been analysed. These sections are divided into subsections dealing with field testing and numerical testing of a single pile and group of piles to distinguish the behaviour of single pile and group of piles.

2.1   Research of a single pile behaviour

Within this section, researches conducted on single pile are presented. As mentioned in chapter introduction, this section is separated into two subsections; the first one dealing with physical testing of piles, and the second one dealing with numerical modelling of piles behaviour.

2.1.1 Physical testing of a single pile

Physical testing of piles can be time and money consuming, but if it is planned wisely, it can provide accurate behaviour of piles in tested soil material.

2.1.1.1 Analysis conducted by Patra and Pise (2001)

Patra and Pise [20] performed analysis and comparison of laterally loaded piles to obtain ultimate horizontal force. Ultimate horizontal, or lateral, force is maximum force that the soil - structure can take before yielding. Tests were performed in laboratory. The tests were conducted on single piles and various arrangements of group of piles in sand. Piles were made of aluminium, with diameter of 19 mm and wall thickness of 0.81 mm. Piles were embedded into sand for 23 cm and 72 cm. Tested *length-to-diameter* values were 12 and 38 and axial spacing of piles was from 3 to 6 pile's diameter. Sand was assumed to have loose relative density with friction angle 20° and medium relative density with friction angle 31°. Analytical expression has been proposed to predict ultimate lateral capacity (herein **ULC**) of a single pile and group of piles. The authors have taken into consideration equation that was presented by Meyerhof et al. [21] for **ULC** and modified it with following considerations taken into account:

- passive earth pressure on the front face was determined according to Kerisel and Absi [22],

- Active earth pressure is neglected,

- Passive earth pressure at the failure was taken as for the wall multiplying it by a constant shape factor 3 [23].

Equations (2.1) and (2.2) show the expressions for ultimate lateral capacity for rigid and flexible free headed pile, respectively.

$$Q_{L,r} = 3 \cdot 0.12 \cdot \gamma \cdot d \cdot L^2 \cdot k_b \tag{2.1}$$

$$Q_{L,f} = 3 \cdot 0.12 \cdot \gamma \cdot d \cdot L_{eff}^2 \cdot k_b \tag{2.2}$$

From the performed tests and analysis, author gave the following conclusions [1]:

1. **ULC** goes along with author's predicted values based on equations (2.1) and (2.2),

2. Method suggested by Meyerhof et at. [21] is applicable to spacings from 3 - 4 pile diameter and has limitations regarding the values of friction angle,

3. **ULC** of a group of piles depends on *length-to-diameter* ratio, friction angle, group geometry, spacings within the group of piles and material density,

4. *p - y* curves are non-linear,

5. Observed displacements at ultimate load were $(0.1 - 0.4)d$ for $L/d = 12$ and $(0.35 - 0.6)d$ for $L/d = 38$,

6. Ultimate resistance per pile increases with an increasing in piles spacing,

7. Group efficiency increases with an increasing in piles spacing.

2.1.2 Numerical analysis of a single pile

Within this subsection, numerical analyses of laterally loaded single pile performed by some researchers are presented. Numerical analysis can give an insight how the pile would perform under lateral loading, but without accurate soil model, the pile-soil interaction behaviour cannot be modelled properly.

2.1.2.1 Analysis conducted by Brown and Shie (1990)

Brown and Shie [11], performed three dimensional numerical analysis of a single pile. Two types of soil were modelled, clay and sand. For the purpose of this Thesis, everything that follows is based on the results for sands. For the sand soil model, the extended Drucker - Prager non-associated criterion was used along the elements that modelled sliding and gaping. The idea was to obtain an insight of deformation patterns and the development of areas of plastic deformations that analytical elastic models couldn't obtain. Authors gave the following observations:

---

[1]Conclusions are mostly regarded to group of piles

1. Using the three-dimensional model, the nature of a problem can fully be modelled,

2. Development of yield zones at the ground surface and the distribution of soil resistance with depth can be calculated,

3. Modelling a soil non-linearity gives an insight how the soil would response and how the yield would occur near the ground surface at relatively small displacements,

4. The zone of yielding propagates laterally and deeply with increasing of pile diameter,

5. The use of friction elements that provide slippage and gaping can enable modelling of the stresses distribution from the pile to the soil,

6. Pattern of soil shear strength with depth is influenced by the confining pressure as well as the geometry of pile.

2.1.2.2   Analysis conducted by Yang and Jeremić (2002)

Yang and Jeremić [7] conducted numerical analyses using finite element method on single laterally loaded pile in elastic-plastic soil model. Pile behaviour was tested in uniform sand, clay and layered soil deposits. Based on the results obtained form numerical analysis authors developed p - y curves and compared them with p - y curves obtained by McVay et al. [24] and Reese et al. [4]. As a soil model, the Drucker - Prager model was used with non-associated flow rule. Young's modulus was assumed to vary with depth. Frictional elements were also used to simulate interaction of pile and soil. Pile was modelled to be made of aluminium, squared shape with 0.429 m in width and about 12 m long with 11.3 m embedded in the soil. The authors concluded that the use of three dimensional finite element model, with the use of very simple constitutive soil model can give good approximation of laterally loaded pile behaviour.

2.1.2.3   Analysis conducted by Fan and Long (2005)

Study of Fan and Long [16] gives the insight into advantages of performing three dimensional analysis in comparison to some other techniques for determining

pile behaviour under lateral loads. They classified existing methods of analysing pile behaviour into five categories and linked them with studies in which analyses of pile behaviour were carried out. These categories of **LLP** analyses itself are [16]: (i) Limit state method, (ii) Subgrade reaction method, (iii) *p-y* method, (iv) Elasticity method and (v) Finite element method.

Authors stated that stress-strain behaviour in cohesionless soil is affected by development of stress paths. It is important to identify and quantify the stress paths state in the soil around the piles.

In the numerical analysis, soil was assumed to be sand and it was modelled using the simple constitutive model defined by Desai et al. [25] with the internal friction of 39° and unit weight of 19 kN/m^3. Pile was modelled as a structural tube element with flexural rigidity **EI** of $1.71 \cdot 10^5 kNm^2$, with outside diameter of 0.61 m and thickness of 9.53 mm. Length of a pile was 21 m. Everything (soil and pile properties, results, etc.) regarding the soil and pile is based on the research made by Reese et al. [4]. Based on result of performed numerical analysis authors gave the following conclusions:

1. Stress concentration is formed in zone from 3-5 pile diameters in depth in the direction of pile loading. This part of a pile is the most important part for lateral capacity,

2. Stress path for the soil element directly in front of a pile is close to triaxial compression conditions with increasing of radial stress, and point between front and edge of a pile has stress path similar to conventional triaxial compression test, while the pile edge stress is behaving like in simple shear condition,

3. The *p-y* curves are not sensitive to the pile stiffness, which supports the assumption of *p-y* method,

4. The ultimate soil resistance is non-linear at any depth and it is not directly proportional to the pile diameter,

5. Initial stiffness of *p-y* curves increases with the coefficient of horizontal earth pressure, k_0, and it can be grater for materials with higher values of k_0 coefficient,

6. The dilatancy has a significant effect on the mobilisation of ultimate soil resistance. **USR** can significantly increase with soil dilatancy even if strength of the soil is constant.

2.1.2.4 Analysis conducted by Mardfekri et al. (2013)

Mardfekri et al. [17] performed analyses of a single pile, taking into account nonlinear soil-pile interaction and the results compared with some simpler analyses, like the analyses performed by Blaney et al. [26], Kausel [27] and Briaud [28]. Unlike some other authors [7, 10], Mardfekri et al. [17] modelled pile and soil using solid elements. Authors also modelled interaction between soil and pile using interface elements. Numerical analysis was performed for clay and sand. The following conclusions came out from the analyses:

1. Deflection of pile head is not only in relation with pile stiffness; it also depends on pile diameter,

2. Modelling of a pile using beam elements results in smaller contribution of the surrounding soil to the lateral stiffness, and an increasing up to 200 % in the maximum displacement of pile head.

2.2 Research of group of piles behaviour

Although the field testing is very expensive, some of the researches performed physical testing of laterally loaded group of piles. Numerical modelling is not fully able to caption the behaviour of materials when they are loaded in the field. Beside field test of group of piles, it is common to perform test of a single pile in the same field in order to compare the measured results of group of piles with the measured results of the single pile.

2.2.1 Physical testing of a group of piles

2.2.1.1 Analysis conducted by Parakash (1962)

Prakash [29] conducted tests in laboratory on cylinders made of aluminium. Outer diameter was 13 mm, thickness 0.89 mm and length 760 mm. Material in which piles were tested has been described as loose and dense sands. Axial distance of a pile to pile was 2 - 8 pile diameters with free head. Conclusions produced from that study are:

1. Efficiency of piles in line is equal to one if axial distance among the piles are equal or larger than 8 pile diameters,

2. Efficiency of sided piles is equal to one if axial distance among piles are equal or larger than 3 pile diameters.

2.2.1.2 Analysis conducted by Schmit (1981,1985)

Field tests were conducted by Schmit [30, 31] on a piles 1.2 m in diameter made of concrete. Two series of tests were performed each one having different depth of a pile. In first tests the depth was 16 m while in second depths were 28 m [30] and 8.5 m [31]. Field test were performed on piles in line with different axial distance (1.33 and 2.42 pile diameters). Material in which piles were embedded is described as a weathered granite type of rock. Based on results of described tests, Schmit proposed following conclusions:

1. Efficiency of group of piles should be calculated based on individual conditions in a field and axial distance of piles, including pile characteristics,

2. Effects of group of piles are not so high as some methods shown (shadowing effects), referred by author,

3. Effect of a pile in group dissipates when the axial distance from pile to pile is equal or bigger than 3 times diameter of pile,

4. With axial distance between piles bigger than three diameters, leading piles are behaving as a single pile. Efficiency of group of piles is then determined by trailing piles,

5. Because of a fixed-head, displacements are the same for all the piles, and consequently bending moments are more or less the same for all the piles.

2.2.1.3 Analysis conducted by Franke (1988)

Franke [32] conducted his tests in laboratory, in a box filled with sand. Spacing of piles was in square shape with distance from axis from 2 - 6 pile diameter. Pile material has not been mentioned. Test on a single pile as a reference test has not been conducted. Instead of that, author assumed that the piles in first row of piles (piles in leading row) are behaving like single piles. Piles were tested in sands with different relative density (from 58 - 88%). Some conclusions that author came up with from results of the tests are:

1. Leading pile of group of piles is behaving as a single pile,

2. The relationship of load between trailed pile, in line of a piles, and a load of leading pile can be approximated with a line in a s/b - p_m plane, where s is axial distance, b is pile diameter and p_m is the relation of ultimate force of trailing and leading row of group of piles

3. Loads on side piles is not varying that much within the group. Efficiency of those piles are equal to single pile if axial distance from pile to pile is equal or bigger than 3 diameters.

2.2.1.4 Analysis conducted by Brown et al. (1988)

Brown et al. [33] tested a group of piles made of steel tube in a 3 by 3 group formation (three rows of piles in three columns). Piles were tested under monotonic and cyclic loading. Piles were made of steel tubes with outside diameter of 27.3 cm and wall thickness of 9.27 mm. The length of piles was 9 m and were embedded in sand with relative density of 50% from 0 to 3 m and underlined with a clay from 3 to 9 m depth. Measuring instruments were installed inside pile which provided measuring data.
The following conclusions were given by authors for monotonic type of loading:

1. Deflection of group of piles was significantly bigger than a single pile for equivalent load per pile,
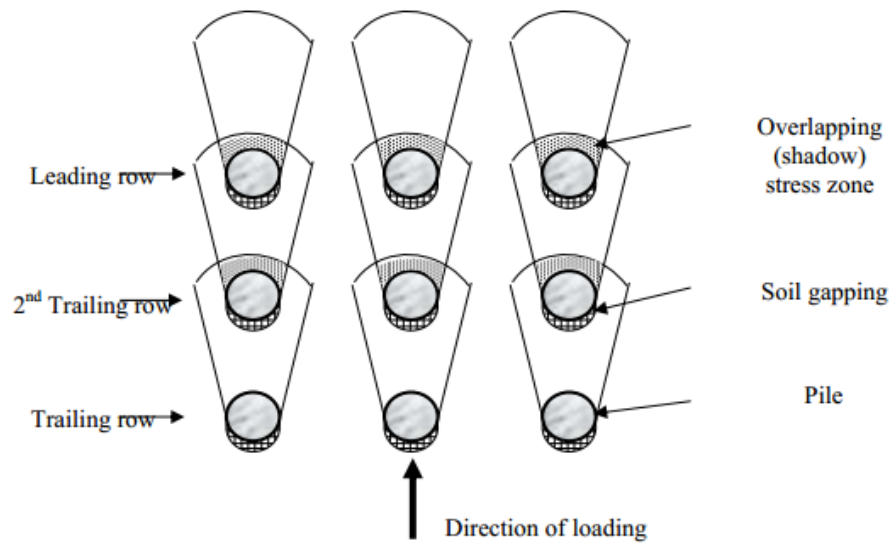
FIGURE 2.1: "Shadowing" effect of pile group [34]

2. The reduced efficiency of a group of piles was mainly caused by "shadowing" (figure 2.1),

3. Bending curves of the piles in a leading row are similar as a curve of an isolated single pile.

2.2.1.5 Analysis conducted by Shibata et al. (1989)

Shibata et al. [35] conducted two series of testing in laboratory on piles made of aluminium, diameters of 20mm and 22mm and length of 800mm. Rotation of a pile head was possible (free head). Tests were performed on piles in line and group of piles with axial distance form 2, 2.5 and 5 pile diameters. Single pile test was performed as well. Piles were embedded in sand with void ratio 0.76 and water content 3.1 %. Based on described results, authors gave the following conclusions:

1. For test conducted on squared shaped group of piles, results showed that axial distance from pile to pile is 3 pile diameters when the piles in the group start to behave as a single piles,

2. For test conducted on a piles in line, piles start to behave as single piles after it's axial distance is 5 pile diameters.

2.2.1.6 Analysis conducted by McVay et al. (1995)

McVay et al. [24] performed detailed centrifuge analysis of **LLP** in loose ($D_r = 33\%$) and medium dense sands ($D_r = 55\%$) on 3 by 3 group of piles with an axial spacing of 3 and 5 pile diameters. Piles were made of aluminium 430 mm long and 13 mm in diameter with wall thickness of 0.4 mm. All tests were performed on free headed piles. Results were compared with tests performed by Reese et al. [4]. The conclusions obtained from the tests results are:

1. Percentage of load carried by an individual row did not change with soil density,

2. "p-multiplier"[2] is independent of soil density,

3. Efficiency of piles spaced at 3 pile diameters is smaller than 5 pile diameters,

4. In the tests on 3 pile diameters spacing, leading row had more than 40% of total load on itself, medium row 32% and trailed row 27%. Total load distribution is influenced on soil density,

5. In the tests on 5 pile diameters spacing, leading load was loaded with 36%, medium row by 33% and trailing row by 31% of total load, for loose and dense sand which means that the load on the group of piles is more or less evenly distributed on pile rows.

2.2.1.7 Analysis conducted by Rollins et al. (2005)

Rollins et al. [36] performed full scaled tests of a 3 by 3 group of piles with axial distance of 3.3 pile diameters. Piles were embedded in loose to medium sands underlay with clay. Piles were made of steel tubes, 0.342 m in diameter with thickness of 9.5 mm and length of 11.5 m. Single pile test has been also conducted. Based on test results, and test results performed by Ashford and Rollins [37], authors gave the following conclusions:

---

[2]"p-multiplier" is the ratio between ultimate soil resistance of a pile in group of piles with regards to the single pile for test conducted in same manner in same material

1. Group efficiency significantly reduced lateral resistance, which was also consistently lower for middle piles within each row,

2. Trailing rows carried less load then leading row,

3. Lateral resistance was found to be a function of both row locations and a position of a pile within each row. Leading piles were carrying largest load than trailing piles. Outer piles carried 20 - 40 % grater loads then middle piles.

Authors are assuming that observed results are caused due to interaction of wider failure wedges for adjacent piles in sands.

2.2.2 Numerical analysis of a group of piles

2.2.2.1 Analysis conducted by Brown and Shie (1990)

Brown and Shie [10] performed numerical 3D analysis of a **LLP** group of piles in one or two rows with axial distance of 10 pile diameters. Soil was modelled as the extended Drucer-Prager material, while piles were modelled as a linear elastic material. Stiffness of elements which simulate piles was calculated from real stiffness of a pile material. Frictional elements were used to simulate slippage and gaping. Details regarding the model are presented in paper by Brown and Shie [11]. Conclusions that arose from numerical analyses are:

1. The influence of spacing is small for spacings of 3 pile diameters and larger in a single row of piles,

2. Soil resistance can increase by the effect of back row of piles which tend to increase confinement of a soil in front of row of piles,

3. Group effect (shadowing effect) is most significantly influenced by row position,

4. Trailing row of piles are subjected to significantly less soil resistance compared to the piles in leading row,

5. Group effect is significant to axial spacings of 3 pile diameters.

2.2.2.2   Analysis conducted by Wakai et al. (1999)

Wakai et al. [8] conducted laboratory tests and numerical analysis of later-
ally loaded group of piles. Most of the numerical analyses were performed
as a three dimensional analysis on the group of piles. Group of 3 by 3 piles
was tested with an axial distance of 3 pile diameters. Analyses were per-
formed on both single and a group of piles. Piles in numerical model were
modelled as beam elements. Soil was modelled as a continuum element with
non-associative Mohr - Coulomb - Drucker - Prager criterion and interaction
between a pile and soil was modelled as a 3D joint element that could simu-
late friction induced by vertical pile displacement. Dilatancy was plugged into a
model. Based on results performed analyses, authors gave the following con-
clusions:

1. Load for a group of piles is less then a load for a single pile multiplied by
   number of piles because of "shadowing" effect. Hence, the "shadowing"
   effect in a group of piles is very significant,

2. Authors noticed that trailing row (last row of the group of piles) has a ten-
   dency of vertical displacement. Because of that vertical resistance of pile
   is also important for the evaluation of **LLP** behaviour,

3. Soil resistance for fixed head **LLP** are larger than for free head pile after
   large deformations.

Chapter 3

Basic theory of laterally loaded piles behaviour in cohesionless soils

3.1 Governing differential equation

LLP can be analysed as an elastic beam foundation. Governing equation of an beam on elastic foundation (3.1) can be found in any book regarding geotechnical engineering [6, 38, 39]. The equation (3.1) consists of a part regarding the behaviour of a beam, and the part that regards the soil. Formulation of equation (3.1) can be depicted from Figure 3.1 as:

$$EI \cdot \frac{d^4y}{dx^4} - E_p \cdot y + q(x) = 0 \qquad (3.1)$$

The part that includes the axial force is neglected because it has a small influence on lateral load and bending moments distribution in a pile.

It has been noted that there are some assumptions regarding the development of differential equation for the beam elastic foundation and they are noted in the following text, according to Reese and Van Impe [6].

- Pile is straight; there is no change in pile shape cross-section,

17
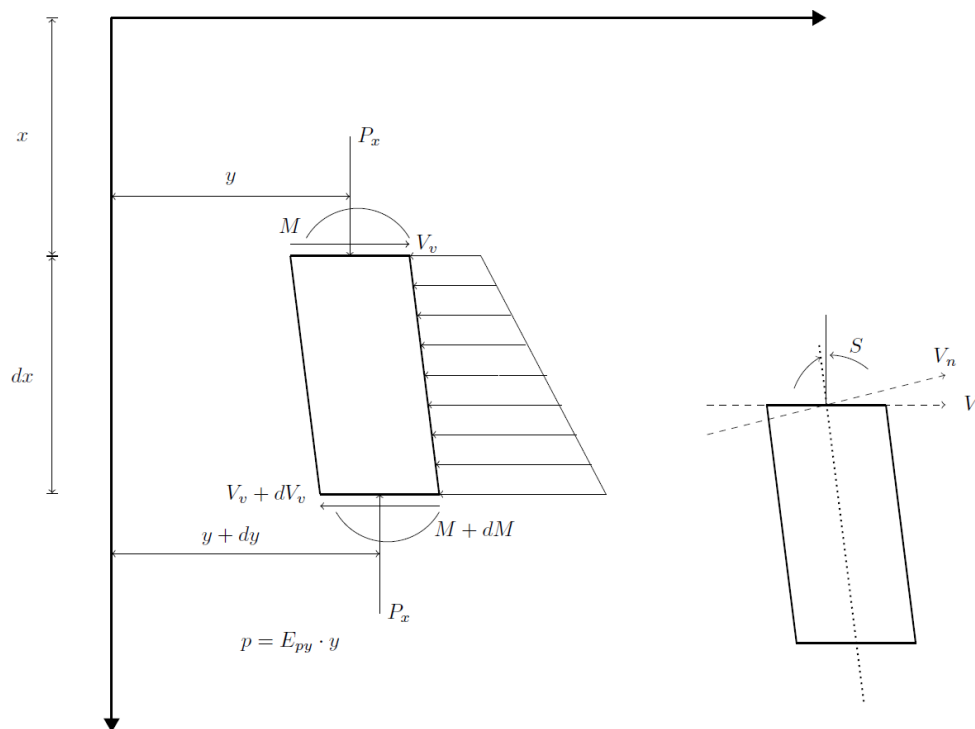
FIGURE 3.1: Element of a beam on elastic foundation [6]

- Loads and reactions lie in the pile longitudinal plane of symmetry,

- Material is homogeneous and has isotropic behaviour,

- The elastic limit of a pile material is not exceeded ,

- Elastic modulus of pile is the same in tension and in compression,

- Transversal displacements are negligible,

- Loading of the pile is monotonic ,

- Displacements due to shear stress are small, and could be neglected.

The closed form solution of differential equation (3.1) can be written in the trigonometric form as the equation (3.2). The coefficients A,B,C and D can be obtained from the boundary conditions plugged in the equation. Boundary conditions for a pile loaded with the horizontal force at the top of the pile are:

- for $x = 0 \rightarrow M = 0$

- for $x = L \rightarrow M = 0$

- for $x = 0 \rightarrow P = F$ and $EI \cdot \frac{\partial^3 y}{\partial x^3} = P$

Equation (3.2) can then be reduced to the equation (3.3).

$$y(x) = e^{\beta x} \left(A \cdot \cos \beta x + B \sin \beta x \right) + e^{-\beta x} \left(C \cdot \cos \beta x + D \sin \beta x \right) \tag{3.2}$$

$$y(x) = \frac{2 \cdot \beta \cdot e^{-\beta x}}{k(x)} \cdot F \cdot \cos \beta x \tag{3.3}$$

with $\beta = \sqrt{\frac{k(x)}{4EI}}$, where:

$k(x)$ - coefficient of subgrade reaction as a function of depth $[kN/m^3]$,

E - Young's modulus of the beam material $[kPa]$,

I - coment of inertia $[m^4]$.

The parameter $k(x)$ is called modulus of subgrade reaction [40] and it usually varies with depth. That is usually true for cohesionless material while when dealing with cohesive material, the modulus of subgrade reaction can be constant.

Many researchers [40, 41, 42, 43, 44, 45, 46, 47] have investigated the modulus of subgrade reaction and it was found that the geometry, the foundation dimensions and soil layers below the foundation structure are the most important parameters which have influence on this modulus. Terzaghi made recommendations how to obtain the modulus of subgrade reaction from 1 x 1 ft rigid plate test placed on different soil layers [40]. The modulus of subgrade reaction may be measured from different experiments such as the plate load test, the oedometer test, the triaxial compression test and the California Bearing Ratio (**CBR**) test. The ranges of values for the modulus of subgrade reaction for typical soil groups are given in Table 3.1.

The above mentioned equations can be solved numerically using **FDM** and **FEM**. The biggest advantages of numerical approximation is that it is possible to use the non-linearity in behaviour of both soil and pile materials. Soil

TABLE 3.1: Range of values of modulus of subgrade reaction k_s [38]

Soil	$k_s\ [kN/m^3]$
Loose sand	$4800 - 16000$
Medium dense sand	$9600 - 80000$
Dense sand	$64000 - 128000$
Clayey medium dense sand	$32000 - 80000$
Silty medium dense sand	$24000 - 48000$
Clayey soil:	
$q_u \leq 200$ kPa	$12000 - 24000$
$200 < q_u \leq 400$ kPa	$24000 - 48000$
$q_u > 400$ kPa	> 48000

(q_u = uniaxial compressive strength)

non-linearity is modelled as a non-linear dependency between displacement and soil resistance usually presented by *p-y* curves.

Most of authors who are dealing with this problem, represented the soil as spring with linear or non-linear behaviour that are placed in a node of beam elements [38].

3.2 Analytical studies of soil-pile interaction

In this section a short overview of analytical methods used in analyses of **LLP** will be presented. The presented methods are recently replaced with significantly numerical methods and analyses but are still very useful for quick calculation of soil - pile interaction in geotechnical practice.

3.2.1 Winkler's solution

Winkler's hypothesis [48] is that the soil is represented with the set of equally spaced springs with defined stiffness. The stiffness is usually represented with the modulus of subgrade reaction, $k(x)$. The drawback of the hypothesis is that only the springs in the contact of loaded foundation would be deformed. That is good assessment regarding beam behaviour but it is not so good presentation of the soil behaviour. Modulus of subgrade reaction can be determined from the field test of **LLP** from the curves those show the soil resistance versus pile displacement. The basic Winkler solution doesn't involve the non-linear behaviour

of spring but it could be easily done. Springs are usually placed in the nodes of the beam. The shorter beam elements, influence on the approximation better, especially if we compare results of an analytical foundation for linear - elastic type of problem with the same type of problem solved numerically. One of the simplest numerical procedure is to use **FDM**, which procedure is described in [38], [2] and many other papers.

Another type of numerical procedure is **FEM**. Spring finite elements are placed in the nodes of beam finite elements. It is essentially the similar procedure like **FDM** but with different element formulation. Jagodnik et al. [19] presented a mixed formulation of a beam on elastic foundation using Winkler's assumption, but instead placing the spring elements only in nodes, the elements are formulated as the springs combined with the beam element. Authors compared the basic types of beam elements, Euler-Bernoulli type with mixed formulation with Timoshenko type of beam foundation and show that Timoshenko's beam on elastic foundation with mixed formulation gives the best results compared with the true analytical solution for linear type problem. The formulation of mixed finite element and its application to pile modelling is given in Section 3.3 in detail.

3.2.2   Development of *p - y* curves for sand

Within this chapter, some basic features of *p-y* curves and procedure for developing *p - y* curves is going to be discussed. Procedure was developed by Reese et al. [4] and it consists of nine steps for *p-y* curves of piles in sandy material. After completing the procedure, the generated *p - y* curves can then be compared either with curves obtained from measuring, or curves obtained from other numerical analyses. As a result of the procedure it is possible to obtain *p - y* curves as it presented on Figure 3.5. Procedure distinguishes dry density and submerged density of soil. The whole procedure is presented in Reese and Van Impe [6]. In this chapter the procedure for determining *p - y* curves for monotonically loaded piles will be discussed.

Basic features of theoretical *p-y* curves are (Figure 3.2):

- from 0 to point (a) $\Rightarrow$ the assumption of small deformation, hence behaviour is linear elastic,

- from point (a) to point (b) $\Rightarrow$ non-linear behaviour of soil,
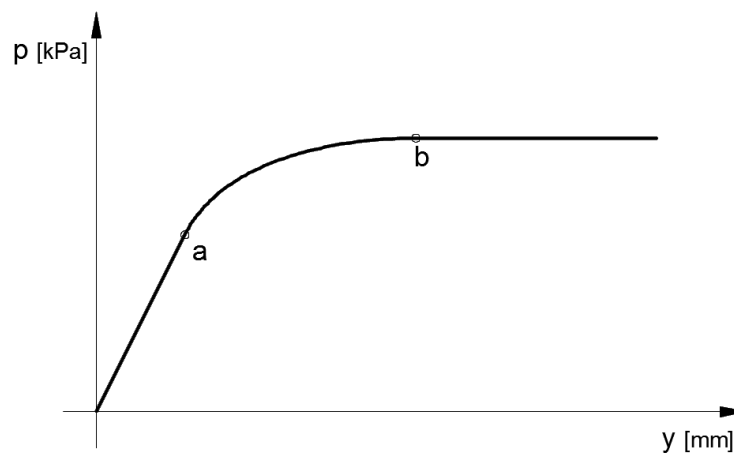
FIGURE 3.2: Theoretical p-y curve

- from (b) $\Rightarrow$ full plastification of soil surrounding the pile.

The ultimate resistance of soil consists of two coupled mechanisms. The first mechanism describes behaviour of pile at depth H. It is formed as a resultant lateral force obtained from a difference between passive force, due to passive wedge formed in a soil where Mohr - Coulomb criterion is reached on passive wedge planes, and active force obtained in Rankine condition (Figure 3.3). The second mechanism is concerned below the ground level and it is obtained from the stress condition in soil around the pile, Figure 3.4. Differentiating the resultant force by depth, ultimate soil resistance for near ground and below ground level can be obtained. Ultimate soil resistance for near ground and below ground level are presented in the equations (3.4) and (3.5).

$$p_{st} = \gamma \cdot z \cdot \left[\frac{k_0 \cdot z \tan \phi \sin \beta}{\tan(\beta - \phi) \cdot \cos \alpha} + \frac{\tan \beta}{\tan(\beta - \phi)} \cdot (b \right. \tag{3.4}$$
$$\left. + z \cdot \tan \beta \cdot \tan \alpha) + k_0 \cdot z \cdot \tan \beta \cdot (\tan \phi \cdot \sin \beta - \tan \alpha) - k_a \cdot b \right]$$

$$p_{sd} = k_a \cdot b \cdot \gamma \cdot z \cdot \left(\tan^8 \beta - 1 \right) + k_0 \cdot b \cdot \gamma \cdot z \tan \phi \cdot \tan^4 \beta \tag{3.5}$$

Procedure for determining *p-y* curve is as follows:
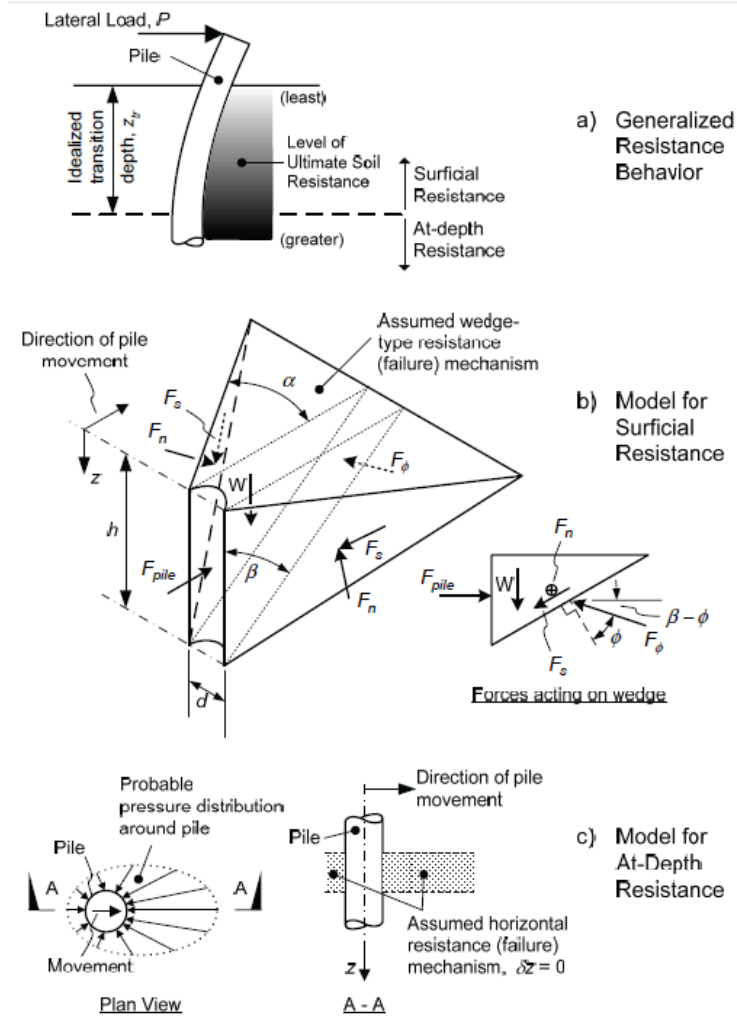
FIGURE 3.3: Passive wedge infront of a **LLP** [49]

1. Determination of internal friction angle of material, ϕ, with a unit weight γ. For unit weight use dry unit weight above the water table and submerged unit weight below the water table,

2. Calculation of the following parameters:

$$\alpha = \frac{\phi}{2}; \beta = 45° + \alpha; k_0 = 1 - \sin\phi; k_a = \tan^2\left(45° - \frac{\phi}{2}\right);$$

3. Calculation of the ultimate soil resistance using the smaller of values obtained from equations (3.4) and (3.5),

4. Calculation of the characteristic depth z_t as an intersection of the equations (3.4) and (3.5). Equation (3.4) above the critical depth should be used and equation (3.5) below critical depth should be used,
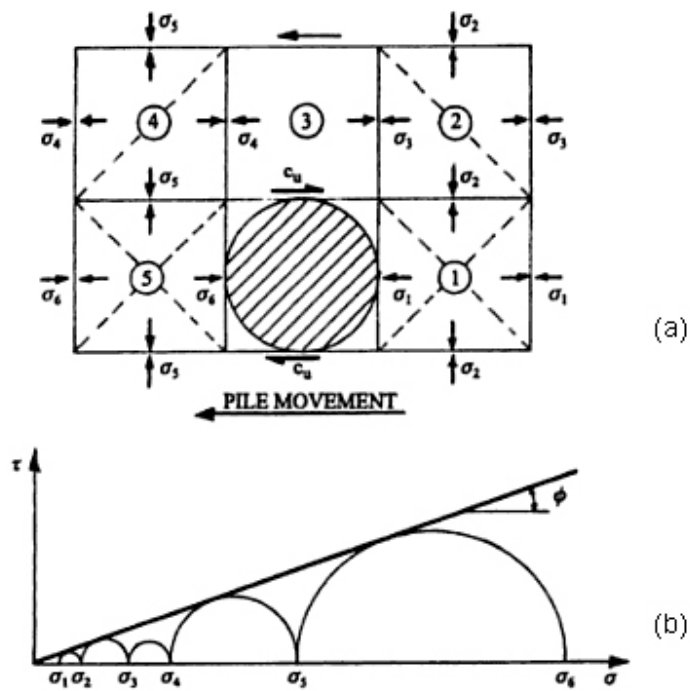
FIGURE 3.4: Assumed model of failure [6]
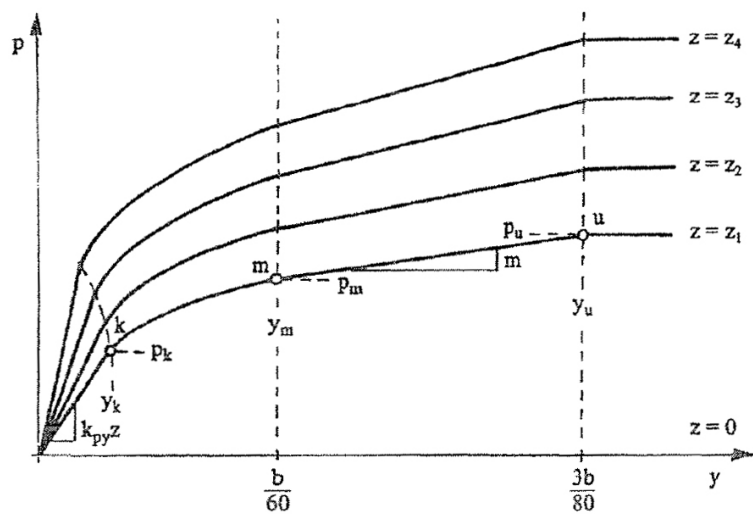
FIGURE 3.5: Characteristic shape of *p - y* curves for sand, [6]

5. Selecting the depth at which *p* - *y* curve should be calculated,

6. Determination of y_u as a $\frac{3 \cot b}{80}$ and calculate p_{ult} as:

$$p_{ult} = \overline{A_s} \cdot p_s \tag{3.6}$$

Parameter $\overline{A_s}$ can be read out from diagram on Figure 3.6 and it is depending on *depth to diameter* ratio.

7. Determination y_m as a $\frac{b}{60}$ and calculate p_m as:

$$p_m = \overline{B_s} \cdot p_s \tag{3.7}$$

Parameter $\overline{B_s}$ can be read out from diagram on Figure 3.6 and it is depending on *depth to diameter* ratio.

8. Calculation of the starting part of a curve:

$$p = k_{py} \cdot z \cdot y_k \tag{3.8}$$

$$y_k = \left(\frac{\overline{C}}{k_{py} \cdot z} \right)^{\frac{n}{n-1}} \tag{3.9}$$

The average values of k_{py} for sand can be found in Table 3.2 or 3.1.

9. Calculation of the parabolic part of *p* - *y* curve:

$$p = \overline{C} \cdot y^{\frac{1}{n}} \tag{3.10}$$

Parabola has to be defined between points k and m:

- Determination the slope of a line between points m an u

$$m = \frac{p_u - p_m}{y_u - y_m} \tag{3.11}$$

- Calculation the exponent of parabolic part

$$n = \frac{p_m}{m \cdot y_m} \tag{3.12}$$

- Calculation the coefficient $\overline{C}$:

$$\overline{C} = \frac{p_m}{y_m^{\frac{1}{n}}} \tag{3.13}$$

TABLE 3.2: Average values of k_{py} for sand [6]

Modulus of subgrade reaction	Relative density		
	Loose	Medium dense	Dense
k_{py} $[MN/m^3]$	5.4	16.3	34

- Calculation of the displacement y_k in point *k* based on equation (3.9).

- Calculation a good amount of data points that fits the parabola using the equation (3.10).

(a) Dimensionless coefficient A_s

(b) Dimensionless coefficient B_s
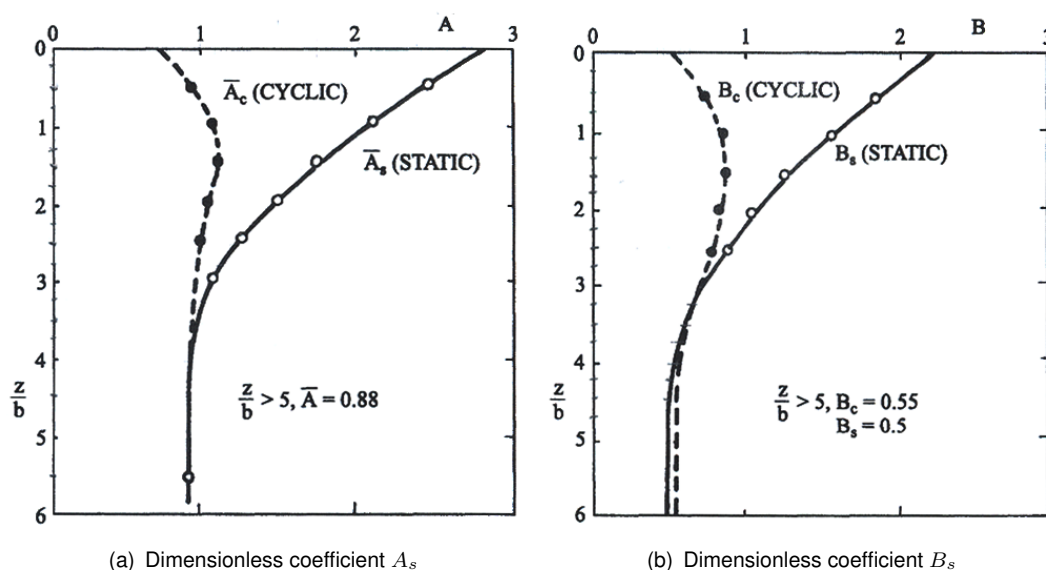
FIGURE 3.6: Dimensionless coeficients A_s and B_s [6]

The previous described procedure is the basic procedure from which *p-y* curves can be calculated. Another type of *p-y* curves development is based on hyperbolic behaviour of curves and it was established by API [50] and DNV [51]. Equations (3.4) and (3.5) are represented with the coefficients C_1, C_2 and C_3 based on a internal friction angle of soil. Curves obtained using coefficients C_1, C_2 and C_3 are presented in Figure 3.7.

The ultimate soil resistance according to this method can be obtained using the equation (3.14) [12].

$$p_u = min \begin{pmatrix} p_{us} = (C_1 x + C_2 D)\,\gamma' x \\ p_{ud} = C_3 D \gamma' x \end{pmatrix} \tag{3.14}$$
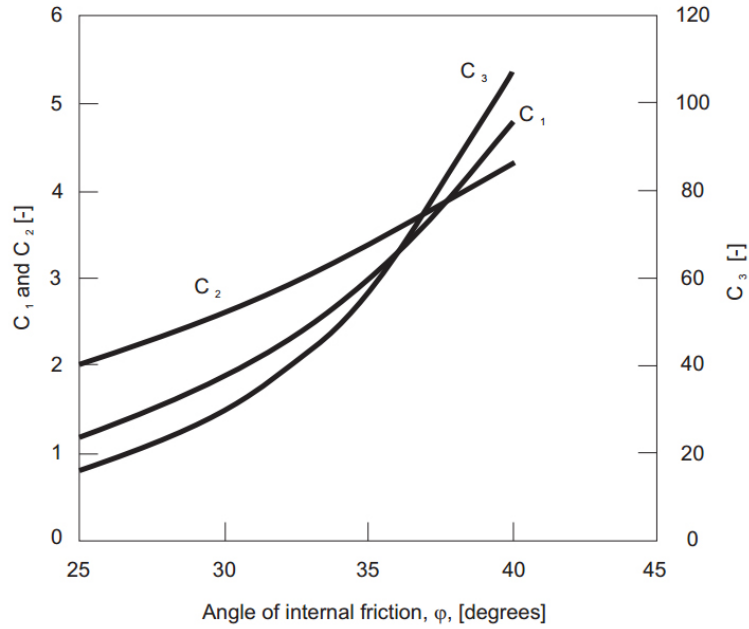
FIGURE 3.7: Variation of the parameters C_1, C_2 and C_3 as function of angle of internal friction angle [12]

To describe relation between the soil resistance and pile deflection, the hyperbolic formula is used, as it shown in equation (3.15) , unlike piecewise formulation previously proposed. The difference between these two proposed formulation is shown in Figure 3.8.

$$p(y) = A \cdot p_u \tanh \left(\frac{kx}{Ap_u} \right) \tag{3.15}$$

where A is defined as:

$$A = \left(3 - 0.8 \cdot \frac{H}{D} \right) \leq 0.9. \tag{3.16}$$

3.2.3 Broms' method

The method is devised by Broms [23] and it is mainly used in cohesive soils, although it has a usage in cohesionless soils. It is formulated for both short and long piles. In further text, the Broms' findings will be limited only to cohesionless soils and long piles.
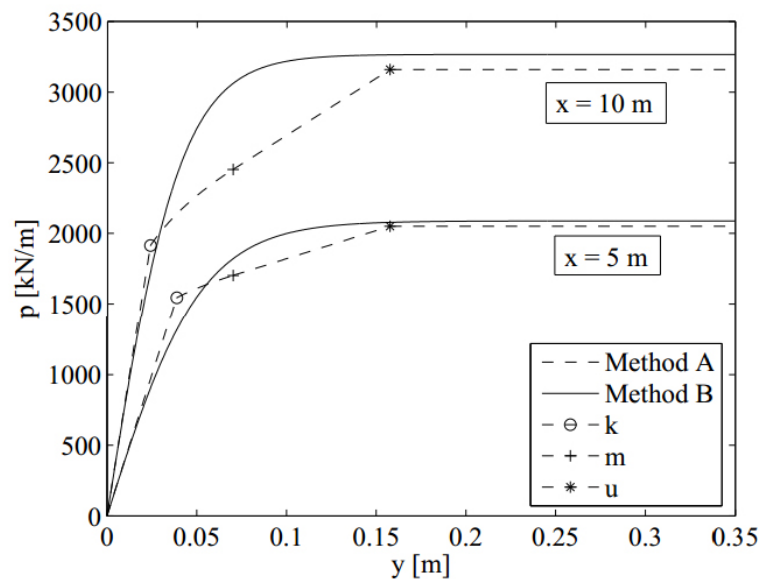
FIGURE 3.8: Difference between Reese's and API's method [12]

According to Broms [23], the assumption made for short piles is that the ultimate lateral resistance would be governed by passive earth pressure activated along the pile. For long piles, the ultimate lateral resistance is governed by the ultimate or yield resistance of pile. The ultimate lateral pressure at the failure of pile can be safely estimated as a three times passive earth pressure according to the Rankine's condition.

Ultimate lateral resistance of soil-pile interaction is governed by ultimate lateral resistance of surrounding soil and by resistance moment of the pile section. The ultimate lateral resistance of long pile is found to be governed by the ultimate bending resistance of the pile, according to Broms [23]. Failure models can be seen in Figure 3.9. If it is not clear that the pile is short or long, then it should be necessary to check the ultimate lateral resistance for short and long pile.

It is assumed that the pile is classified as a long pile. To calculate the ultimate load, the yield moment of the pile should be calculated first. By dividing the yield force with the $k_p \cdot D^3 \cdot \gamma$ the *x* axis values at the diagram on Figure 3.10 will be obtained. By knowing the pile fixation and diameter to length ratio, the ultimate load P_{ult} would be calculated.

Broms' method can be used to approximate lateral deflection of a pile. Lateral deflection is determined by the assumption of soil reaction varying linearly with
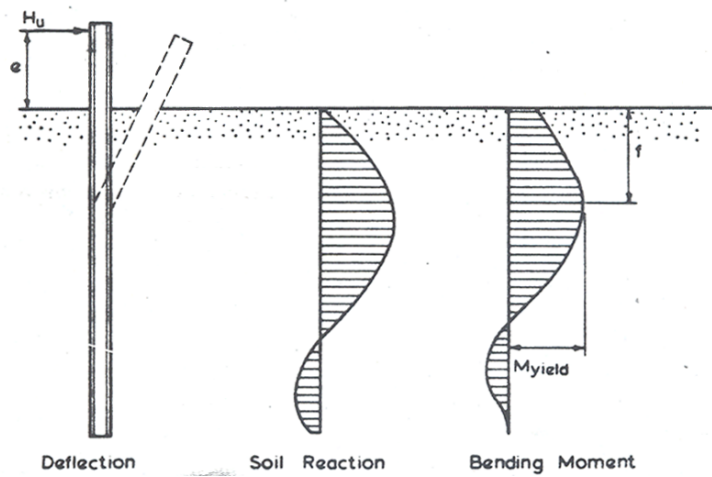
FIGURE 3.9: Failure modes of long piles in cohesionless soil [23]
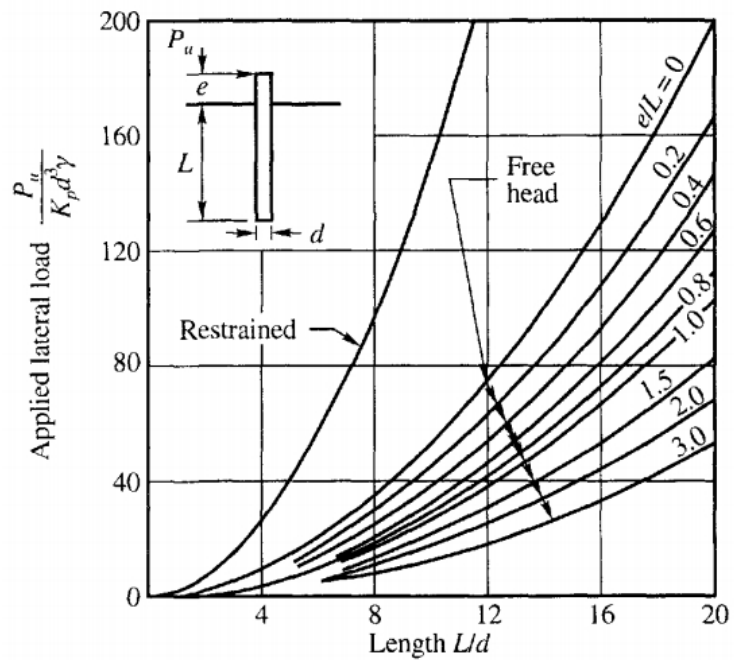
FIGURE 3.10: Ultimate load based on Broms' method [23]

the depth. By assuming the modulus of soil reaction as it is proposed in equation 3.17, the parameter for dimensionless length would be calculated based on equation 3.18.

$$k_h = \frac{n_h \cdot z}{D} \qquad (3.17)$$

where:

k_h - the modulus of horizontal subgrade reaction [kN/m^3],

z - depth below the ground level [m],

n_h - coefficient that depends on relative density of soil [kN/m^3],

D - pile diameter [m].

$$\eta = \sqrt[5]{\frac{n_h}{EI}} \qquad (3.18)$$

After determinating the value η from equation 3.18, and multiplying η with the length of the pile, the first parameter for ground level deflection is obtained. That value is the *x* axis value on Figure 3.11. If the fixation condition and diameter to length ratio are known then the ground deflection can be evaluated.

3.2.4   Pile in elastic continuum model

The solutions of pile behaviour in elastic continuum model, herein **ECM**, was proposed by Mindlin [52] and was developed for a point force acting on a semi-infinite elastic half space. Elastic continuum model was the one of starting points in Poulos' [2, 3] approach when he investigated laterally loaded piles behaviour in elastic soil model. However, it has to be noted there are several limitations on **ECM**. The main limitation is the assumption of homogeneous isotropic elastic soil behaviour. It could be assumed that soil is behaving elastically, but it is correct for only extremely small strains. In order to overcome the above mentioned problem, Poulos [2, 3] adopted Mindlin's solutions. That allowed to vary the Young's modulus with depth, and also to compensate the
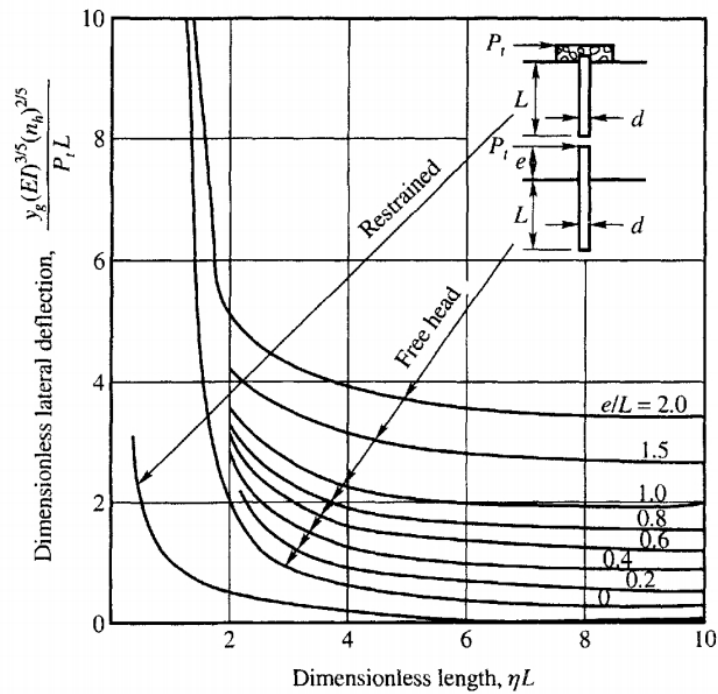
FIGURE 3.11: Ground level deflection based on Broms method, [23]

non-linear response of soil due to high pressures developed at the ground level. Gazetas [53] stated that the soil response of laterally loaded piles and moments in the pile are independent of their length, because the upper part of flexible pile, which is called effective or active length, experiences significant deformation. The imposed load is transmitted to the surrounding soil in order of 5 to 10 pile diameters.

ECM is based on the elastic soil modulus, E_s, which can be determined by testing or estimated from guidelines presented by several authors [53, 54, 55]. Based on some previous testing, [54, 55], the best way to determine E_s is from results of back analyses of full scaled test.

The **ECM** equations presented later are those for three different soil distributions with depth as it is tabulated in Table 3.3. Also, these equations can be used only for long and flexible piles, which are of interest in this Thesis. These equations are based on the study of Davies and Budhu [54] for constant stiffness distribution and for linearly increasing stiffness, [56], and Gazetas [53] for three types of stiffness distribution through the depth of the pile. **ECM** is one of the useful methods in analysing the pile-soil interaction by taking into account the continuity of the soil model around the pile.

In the first step of **ECM**, pile and soil are assumed to have elastic behaviour. With that assumption, pile displacements at the ground level, u_{GL}, and pile rotation at the ground level, θ_{GL}, can be determinate from the equation (3.19) and (3.20):

$$u_{GL} = f_{uH}H + f_{uM}M \tag{3.19}$$

$$\theta_{GL} = f_{\theta H}H + f_{\theta M}M \tag{3.20}$$

where:

H - applied lateral load at a pile head [kN]

M - applied moment at a pile head [kNm]

f_{uH}, f_{uM} - flexibility coefficients for displacements of pile given in Table 3.3

$f_{\theta H}$, $f_{\theta M}$ - flexibility coefficients for rotations of pile given in Table 3.3

Total lateral displacement and rotation, u_{total} and θ_{total} can be calculated using the following equations (3.21) and (3.22):

$$u_{total} = \frac{H \cdot L^3}{3EI} + \frac{M \cdot L^2}{2EI} + u_{GL} + u_{\theta,GL} \tag{3.21}$$

$$\theta_{total} = \frac{H \cdot L^3}{2EI} + \frac{M \cdot L}{EI} + \theta_{GL} \tag{3.22}$$

where:

H - lateral force applied at the head of pile construction [kN],

M - lateral moment applied at the head ofpile construction [kNm],

L - length of a pile [m],

EI - flexural rigidity of a pile [kNm^2].

The next step is to calculate the flexibility coefficients for the pile at the ground level. These coefficients are available for various types of soil profiles. The definitions of these types are summarised in Table 3.3. The components of the pile stiffness at the ground level are defined by equation (3.23):

$$
\begin{pmatrix} K_{HH} & K_{HM} \\ K_{MH} & K_{MM} \end{pmatrix} = \frac{1}{f_{\theta M} f_{uH} - fuM^2} \begin{pmatrix} f_{\theta M} & -f_{uM} \\ -f_{\theta H} & f_{uH} \end{pmatrix}
\tag{3.23}
$$

where: K_{HH}, K_{HM}, K_{MH} and K_{MM} are pile stiffness matrix components at the ground level. Equivalent unrestrained stiffness of a pile at ground level can be determined using equations (3.24) and (3.25):

$$
K_h = \frac{K_{HH} K_{MM} - K_{HM}^2}{K_{MM} - e K_{HM}}
\tag{3.24}
$$
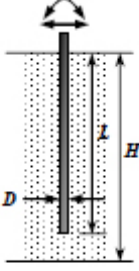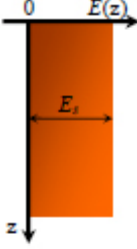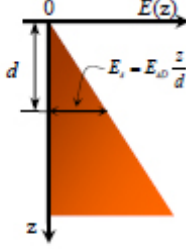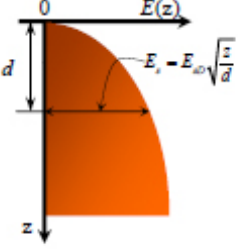
$$
K_\theta = \frac{K_{HH} K_{MM} - K_{HM}^2}{K_{HH} - K_{HM}/e}
\tag{3.25}
$$

To compensate the soil and pile, non-linearity is achieved by applying modification factors to elastic predictor as it was suggested by Davies and Budhu [54]. Equations (3.26) give the pile head deflection, pile head rotation, maximum moment of the free headed pile with non-linear behaviour. The details of the equations can be depicted in Table 3.3.

$$
\begin{aligned}
u_y &= I_{uy} \cdot u_{GL} \\
\theta_y &= I_{\theta y} \cdot \theta_{GL} \\
M_{My} &= I_{My} \cdot M_{ME}
\end{aligned}
\tag{3.26}
$$

where: I_{uy}, $I_{\theta y}$ and I_{My} are yield influence factors.

TABLE 3.3: Static response of single free-head piles for three different soil distributions with depth, [57]

Pile in ground	E_s Constant with Depth	E_s Linear with Depth	E_s Parabolic with Depth
Stiffness Ratio	$K_{con} = \dfrac{E_p}{E_s}$	$E_s = md \qquad K_{lin} = \dfrac{E_p}{md}$	$E_s = E_{sd}\sqrt{\dfrac{z}{d}} \qquad K_{par} = \dfrac{E_p}{E_{sd}}$
Static Active Pile Length	$L_{ar\_con} = 0.50\,D\,K_{con}^{0.36}$	$L_{ar\_lin} = 1.3\,D\,K_{lin}^{0.222}$	
Length of Max. Moment	$L_{M\,max} = 0.40\,L_{ar\_con}$	$L_{M\,max} = 0.41\,L_{ar\_lin}$	
Coefficients of Flexibility	$f_{uH} = \dfrac{1.3K_{con}^{-0.18}}{E_s D}$ $\quad$ $f_{uM} = f_{\theta H} = \dfrac{2.2K_{con}^{-0.45}}{E_s D^2}$ $\quad$ $f_{\theta M} = \dfrac{9.2K_{con}^{-0.73}}{E_s D^3}$	$f_{uH} = \dfrac{3.2K_{lin}^{-0.333}}{mD^2}$ $\quad$ $f_{uM} = f_{\theta H} = \dfrac{5.0K_{lin}^{-0.556}}{mD^3}$ $\quad$ $f_{\theta M} = \dfrac{13.6K_{lin}^{-0.778}}{mD^4}$	$f_{uH} = \dfrac{2.14K_{par}^{-0.29}}{E_{sd} D}$ $\quad$ $f_{uM} = f_{\theta H} = \dfrac{3.43K_{par}^{-0.53}}{E_{sd} D^2}$ $\quad$ $f_{\theta M} = \dfrac{12.16K_{par}^{-0.77}}{E_{sd} D^3}$
Maximum Bending Moment	$M_{ME} = I_{MH} DH$ $I_{MH} = aK^b$ $a = 0.12 + 0.24f + 0.1f^2$ $b = \exp(-1.3 - 0.34f)$ if $I_{MH} > 6$; $I_{MH} = f = M/DH$	$M_{ME} = I_{MH} DH$ $I_{MH} = aK^b$ $a = 0.6f$ $b = 0.17f^{-0.3}$ if $I_{MH} > 8$; $I_{MH} = 8$	Not available for this case
Yield Influence Factors	Over-consolidated soil: $I_{uy} = 1 + \dfrac{h - 2.9k^{0.2}}{10.5k^{0.45}}$ where: $I_{\theta y} = 1 + \dfrac{h - 2.9k^{0.2}}{12.5k^{0.33}}$ $\quad h = \dfrac{H}{s_u D^2}$ $I_{My} = 1 + \dfrac{h - 2.9k^{0.2}}{20k^{0.29}}$ $\quad k = \dfrac{K}{1000}$	Normally-consolidated soil: $I_{uy} = 1 + \dfrac{h - 14k^{0.32}}{40k^{0.53}}$ where: $I_{\theta y} = 1 + \dfrac{h - 14k^{0.32}}{54k^{0.53}}$ $\quad h = \dfrac{H}{s_u D^3}$ $I_{My} = 1 + \dfrac{h - 8k^{0.32}}{96k^{0.48}}$ $\quad k = \dfrac{K}{1000}$	Not available for this case
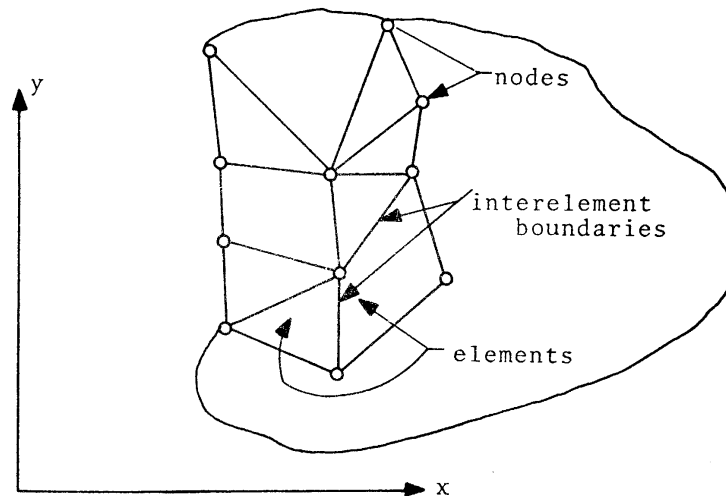
FIGURE 3.12: Elements in continuum [58]

3.3 Finite element analyses

Finite element analysis, **FEA**, is a numerical procedure that uses mathematical technique called finite element method, **FEM**, to solve partial differential equations, **PDE**. The analysed space is discretized with points that are connected with the finite number of elements, called finite elements (Figure 3.12).

There are many books that describe the procedures of the method, how does it work, how can it be implemented, its' linear and non-linear solutions [58, 59, 60, 61, 62, 63]. This section will be more focused on the use of **FEM** and **FEA** from the geotechnical point of view, especially for the problem of laterally loaded piles.

3.3.1 Basic features of FEM

In the structural and geotechnical engineering the main problem is to determine stresses and displacements caused from the forces applied on the analysed body. The nature of distribution of the effects in observed body depends on force system and body characteristics. It can be also stated that three types of balance equations should be defined: force equations, constitutive equations and kinematic equations.

Formulation of **FEM** can be divided in approximately eight steps, as mentioned by Desai et al. [62]. These steps are:

1. **Discretization and element configuration**
   This first step is discretization of the analysed domain with finite number of nodes. Nodes are then connected with the finite number of elements, called finite elements. With this step, number of finite elements, hence nodes, are defined. By knowing what type of analyses would be performed (1-dimensional, 2-dimensional or 3-dimensional), different shape of those elements can be chosen. For each of finite element used in analysis, appropriate shape function that describes the behaviour of element between two nodes has to be defined.

2. **Selection of approximation model or functions**
   Definition of element shape function is one of the most important step in finite element analysis. General displacement function in an element is defined as a scalar product of node unknowns and shape functions, thus making the shape functions essential variables for finite element accuracy.

3. **Defining constitutive and kinematics relations**
   Basically, within this step the stress-strain and strain-displacement relationship should be defined. Depending on the type of an problem, the constitutive matrix should be defined in this step. For the linear behaviour of material, the procedure is very simple, but if the non-linearity is taken into consideration, on the procedures tend to be more complicated. The non-linearity problem in finite element analyses will be discussed in the section later.

4. **Deriving the element equations**
   This step is the second most important part in the finite element procedure. Within this step, the element equations are defined either by using energy methods or method of weighted residuals. The result of this step is the stiffness matrix, in literature also known as $\underline{\mathbf{K}}$.

5. **Assembling the elements and defining the boundary conditions**
   The elements of discretize body are assembled into the global stiffness matrix $\underline{\mathbf{K}}$. The size of matrix is the same as it is the number of unknowns and external forces. But by applying the boundary condition, the size of

matrix can be reduced. Stiffness matrix after boundary conditions are applied is sometimes known as constrained stiffness matrix $\underline{\mathbf{K}}$.

6. **Solving the primary unknowns**

   In this step, the system of equations defined in previous step will be solved using the system of equation defined as:

   $$\underline{u} = \underline{\mathbf{K}}^{-1}\underline{R}. \tag{3.27}$$

   As it was said before, the primary unknowns are only displacements, displacements and rotations, pressure etc.

7. **Solution of the second unknowns**

   In this step usually the stresses and strains would be calculated using the constitutive and kinematic equations and relations.

8. **Interpretation of the results**

   The step is used for the presentation of the results calculated in previous steps.

3.3.2 Constitutive models used in geotechnical engineering related to the LLP modelling

Proper behaviour of soil is very hard to describe with any of well known constitutive models. The best way to identify proper soil behaviour is to test the soil, and try to find which constitutive model is the best to fit tested data. That is possible, but the number of parameters needed to be described for soil behaviour can be significant. That is the reason why engineers are trying to use simpler models to describe the soil behaviour. One of the most simplest constitutive model is Von Mises model. This constitutive model is often used to describe behaviour of clayly soil because it is described using the ultimate stress state which is associated with undrained strength of clay.

In Chapter 2, Section 2.1.2 and 2.2.2 a short discussion regarding some of constitutive models in analysing of **LLP** behaviour is presented. Most of researchers utilize simpler models [7, 10, 11, 15], using the non-associated or associated flow behaviour, while some of researchers utilize a little bit more sophisticated constitutive models [8, 16, 25, 35]. If it is possible, the sliding or

gaping interface elements can be used as an enhancement in simpler models. The following text will concern the constitutive models that are used in modelling of cohesionless material of soil such as a sand behaviour. One of the simplest and very often used constitutive model, the Mohr-Coulomb constitutive model, will be used as a computer verification in Chapter 7.

3.3.2.1   Mohr-Coulomb constitutive model

The Mohr-Coulomb (**MC**) constitutive model can be defined as elastic-perfectly plastic constitutive model of material behaviour. It is defined with only two parameters that would be obtained from conventional soil testing techniques: cohesion and friction angle. Those two parameters are sufficient to describe the basic **MC** model of soil behaviour. An extended **MC** constitutive model can be formulated by adding a one new parameter, angle of dilation, thus making it possible to model behaviour more accurate.

The failure surface of **MC** criterion is given with the equation (3.28) while the plastic potential is represented with equation (3.29). All equations are written in the form of stress invariants.

$$ f\left(I_1, J_2, \Theta, \phi\right) = -\frac{1}{3}I_1 \sin(\phi) + \sqrt{J_2}\left(\frac{\sin(\Theta)\sin(\phi)}{\sqrt{3}} + \cos(\Theta)\right) - c\cos(\phi) \quad \text{(3.28)} $$

$$ g\left(I_1, J_2, \Theta, \phi, \phi_{\text{dil}}\right) = -\frac{1}{3}I_1 \sin\left(\phi_{\text{dil}}\right) + \sqrt{J_2}\left(\frac{\sin(\Theta)\sin(\phi)}{\sqrt{3}} + \cos(\Theta)\right) - c\cos(\phi) $$
$$ \text{(3.29)} $$

The most of commercial softwares in geotechnical engineering use **MC** model failure surface and associated plastic potential for stress and deformation analyses.
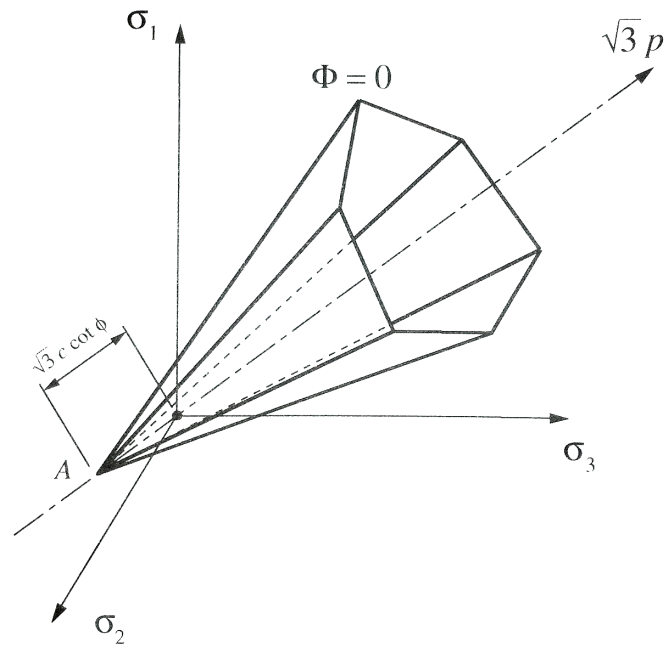
FIGURE 3.13: The Mohr-Coulomb failure surface in the principle stresses plane space [64]

3.3.2.2 The Drucker - Prager constitutive model

The Drucker-Prager (**DP**) constitutive model can be described as elasto - plastic constitutive model and can be considered as an approximation of the Mohr-Coulomb model [65]. Plot of the failure criterion in the space of principle stresses is presented in Figure 3.14. Approximation of the Mohr-Coulomb criterion with the Drucke-Prager criterion is shown on Figure 3.15. Here it should be noticed that this approximation can be very rough.

Very often, the Drucker-Prager criterion is also expressed using the stress invariants as presented in equation (3.30). In this equation the parameters α and k represent material parameters of failure criterion.

$$f\left(J_2, I_1, \alpha, k\right) = \sqrt{J_2} - \alpha I_1 - k \tag{3.30}$$

Parameters α and k should be properly described because **DP** criterion corresponds to different points of intersection which are shown in Figure 3.15. In Table 3.4 the expressions for the mentioned parameters are given in correlation to their position in the space of principle stresses [65].
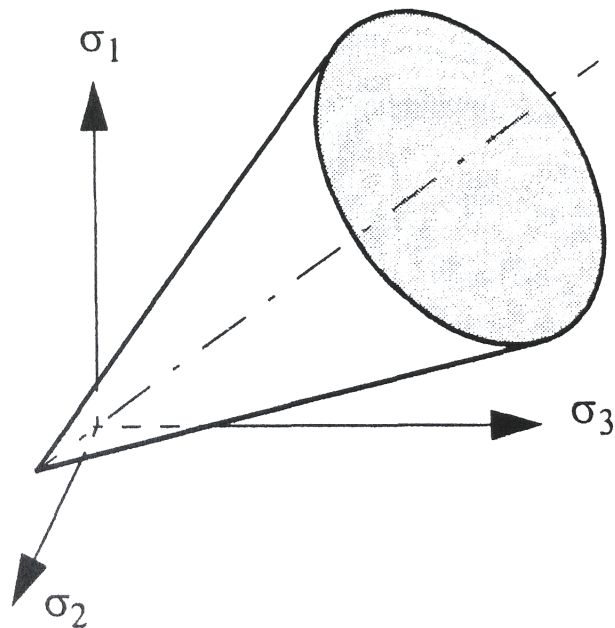
FIGURE 3.14: The Drucker-Prager failure surface in the principle stresses plane space [65]
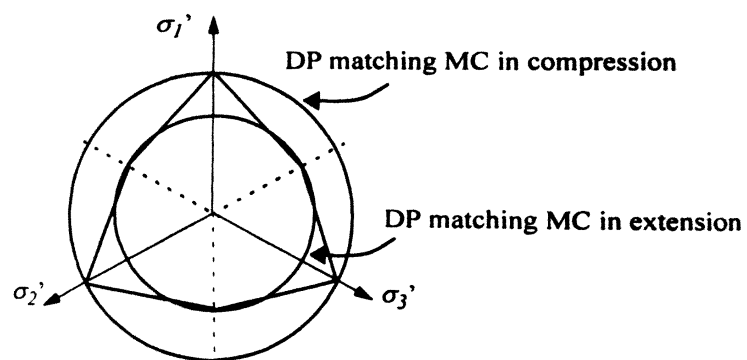
FIGURE 3.15: Alternative Drucker-Prager failure surfaces compared to Mohr-Coulomb failure surface [65]

TABLE 3.4: Material parameters α and k, [65]

Coinciding for	α	k
Triaxial compression $(\sigma_2' = \sigma_3')$	$\dfrac{2\sin\phi}{\sqrt{3}(3-\sin\phi)}$	$\dfrac{6c\cos\phi}{\sqrt{3}(3-\sin\phi)}$
Triaxial extension $(\sigma_2' = \sigma_1')$	$\dfrac{2\sin\phi}{\sqrt{3}(3+\sin\phi)}$	$\dfrac{6c\cos\phi}{\sqrt{3}(3+\sin\phi)}$
Tangential inner circle	$\dfrac{\sin\phi}{\sqrt{3}\sqrt{3+\sin^2\phi}}$	$\dfrac{6c\cos\phi}{\sqrt{3}\sqrt{3+\sin^2\phi}}$

3.3.3 Application of mixed FEM approach to beam on elastic foundation

To avoid complex soil behaviour, the subgrade reaction model is often used how it is proposed by Winkler [48]. Solution of a beam resting on an elastic soil model is considerably changed with respect to the beam with no solid. Although, there is a solution for an "exact" beam-soil element, equations are designed for situations of limited applicability and because that the non-standard shape functions may contain some singularities [66]. Jagodnik et al. [19] performed some analyses, which showed that resulting soil-stiffness contribution becomes different, even though the beam stiffness contribution is the same, depending on type and field interpolation. If the soil-reaction field is interpolated independently from the interpolation of the displacement using the mixed type **FEM** technique, the soil-stiffness contribution should be changed. In the following text, the summary of mixed **FEM** approach to beam resting on elastic soil is presented.

3.3.3.1 Displacement based approach to Bernoulli beam

Focusing on beam part of an equation (3.1) from variational point of view it will satisfy the solution if the total potential energy of a problem is stationary $V = V_{def} - U$. Here $V_{def} = \frac{1}{2}\int_0^L EIw''^2$ is the strain energy and U is the work of applied load. From variation $\delta V = 0$ it follows:

$$\int_0^L \left(\delta w'' EIw''\right) dx - U = 0 \tag{3.31}$$

Dividing the beam into N_{el} finite element of length l_i and assuming the distribution of the displacement field within each element as $w_i(\xi) = N_i(\xi)p_i$ with $p_i^t = \langle w_i \; \theta_i \; w_{i+1} \; \theta_{i+1} \rangle = \langle w(x_i) \; w'(x_i) \; w(x_{i+1}) \; w'(x_{i+1}) \rangle$ the following equation is obtained:

$$\sum_{i=1}^{N_{el}} \delta p_i^T \left(K_{b,i} p_i - R_i \right) = 0 \tag{3.32}$$

Matrix $\mathbf{K}_{b,i}$ is defined by satisfying the C^1 continuity because of the presence of second derivatives using Hermitean polynomial interpolation [60] and it is shown in integration form by equation (3.33) while the matrix after integration is defined with equation (3.34) for a random length of element.

$$K_{b,i} = \int_{-1}^{1} \frac{8EI}{l_i^3} \frac{d^2 N_i^T}{d\xi^2} \frac{d^2 N_i}{d\xi^2} d\xi \tag{3.33}$$

$$K_{b,i} = \frac{EI}{l_i^3} \begin{bmatrix} 12 & -6l_i & -12 & -6l_i \\ -6l_i & 4l_i^2 & 6l_i & 2l_i^2 \\ -12 & 6l_i & 12 & 6l_i \\ -6l_i & 2l_i^2 & 6l_i & 4l_i^2 \end{bmatrix}. \tag{3.34}$$

3.3.3.2 Bernoulli's beam as a shear-rigid Timoshenko's beam

The main difference between the Bernoulli's and Timoshenko's beam theories is in the assumption of rotation of the centroid line by a shear angle $\gamma(x)$, which is resulting with the shear-stress resultant $T(x) = GA\gamma(x)$. Total potential energy of the problem must be stationary at equilibrium ($V = V_{def} - U$). Strain energy of the system is defined as $V_{def} = \frac{1}{2} \int_0^L \left(EI\theta'^2 + GA\gamma^2 \right) dx$, variational form can be expressed with the following equation:

$$\delta V = \int_0^L \delta \theta' EI\theta' dx + \int_0^L \delta \left(w' + \theta \right) GA \left(w' + \theta \right) dx - \delta U = 0 \tag{3.35}$$

If the beam is divided into N_{el} finite elements, and assembling the unknown kinematic fields, defining them with the interpolation vector, system could lead to the well-known and documented phenomena called *shear-locking* [37, 60]

which arises from the fact that the order of interpolating polynomial is the same for displacements and rotations, making it unable for the element to describe the state of constant shear. One of the solution is to consider the shear-stress resultant T as an independent field. Mixed energy functional then would be $V = V_d + V_{dT} - V_T - U$ with $V_d = \frac{1}{2}\int_0^L EI\theta'^2 dx$, $V_{dT} = \int_0^L (w' + \theta) T dx$ and $V_T = \frac{1}{2}\int_0^L \frac{T^2}{GA} dx$. Variational equation is given with equation :

$$\delta V = \int_0^L \delta\theta' EI\theta' dx + \int_0^L \delta(w' + \theta) T dx + \int_0^L \delta T(w' + \theta) dx - \int_0^L \delta T \frac{T}{GA} dx - \delta U = 0 \tag{3.36}$$

Performing the step mentioned in text earlier, but with additional shear-stress interpolation as $T = N_T T_i$, for N_{el} number of elements, the equation (3.36) turns into:

$$\sum_{i=1}^{N_{el}} \left\{ \delta p_i^t \left(K_{d,i} p_i + K_{dT,i} T_i - R_i \right) + \delta T_i^t \left(K_{dT,i}^t p_i + K_{T,i} T_i \right) \right\} = 0 \tag{3.37}$$

where

$$K_{d,i} = \frac{2}{l_i} \int_{-1}^1 \frac{dN^t}{d\xi} \begin{bmatrix} 0 & 0 \\ 0 & EI \end{bmatrix} \frac{dN}{d\xi} d\xi \tag{3.38}$$

$$K_{dT,i} = \int_{-1}^1 \left(\langle \frac{d}{d\xi} \frac{l_i}{2} \rangle N \right)^t N_T d\xi \tag{3.39}$$

$$K_{T,i} = -\frac{l_i}{2GA} \int_{-1}^1 N_T^t N_T d\xi. \tag{3.40}$$

$$K_{b,i} = K_{d,i} - K_{dT,i} K_{T,i}^{-1} K_{dT,i}^T \tag{3.41}$$

Beam stiffness equation can be defined as it is shown in the equation (3.41). Stiffness matrix can be calculated using the Lagrangian functions for three-node element interpolation for displacements and rotations and liner for shear-stress resultant. By considering out the mid-node degrees of freedom it can be obtained the following matrix:

$$K_{b,i} = \frac{EI}{(1+\phi)l_i^3} \begin{bmatrix} 12 & -6l_i & -12 & -6l_i \\ -6l_i & (4+\phi)l_i^2 & 6l_i & (2-\phi)l_i^2 \\ -12 & 6l_i & 12 & 6l_i \\ -6l_i & (2-\phi)l_i^2 & 6l_i & (4+\phi)l_i^2 \end{bmatrix},$$ (3.42)

with $\phi = \frac{12EI}{GAl_i^2}$. When $GA \to \infty$ then $\phi = 0$ and the equation (3.42) becomes as (3.34).

3.3.3.3 Displacement based approach to Bernoulli-Winkler beam – one-field interpolation

The problem may be approached in the same way as presented before with the only difference in strain energy that has a part influenced from soil, $V_{def} = \frac{1}{2} \int_0^L \left(EIw''^2 + kw^2 \right) dx$. The stiffness matrix can be separated into two parts: (i) the first defining the stiffness of beam and (ii) the second defining the stiffness of soil. Soil stiffness matrix can be easily obtained using the equation (3.43) using Hermitean polynomials as shape functions. Soil stiffness matrix is given with equation 3.44.

$$K_{s,i} = \int_{-1}^1 \frac{kl_i}{2} N_i^T N_i d\xi$$ (3.43)

$$K_{s,i} = k \cdot l_i \begin{bmatrix} \frac{13}{35} & -\frac{11}{210}l_i & \frac{9}{70} & \frac{13}{420}l_i \\ -\frac{11}{210}l_i & \frac{1}{105}l_i^2 & -\frac{13}{420}l_i & -\frac{1}{140}l_i^2 \\ \frac{9}{70} & -\frac{13}{420}l_i & \frac{13}{35} & \frac{11}{210}l_i \\ \frac{13}{420}l_i & -\frac{1}{140}l_i^2 & \frac{11}{210}l_i & \frac{1}{105}l_i^2 \end{bmatrix}$$ (3.44)

3.3.3.4 Mixed FEM approach to Bernoulli-Winkler problem – two-field interpolation

Using the mixed approach by introducing the new function $f(x)$ that represents distributed soil reaction field, potential function can be rewritten now as $V = V_b + V_{bf} - V_f - U$, where $V_b = \frac{1}{2} \int_0^L EIw''^2 dx$, $V_{bf} = \int_0^L fw \, dx$ and $V_f = \frac{1}{2k} \int_0^L f^2 dx$. Function $w(x)$ and $f(x)$ can be treated separately. Dividing the beam into N_{el}

elements and assuming an additional interpolation for distributed soil reaction field, the variation equation turns into:

$$\sum_{i=1}^{N_{el}} \left[\delta p_i^t \left(K_{b,i} p_i + K_{bf,i} f_i - R_i \right) + \delta f_i^t \left(K_{bf,i}^t p_i + K_{f,i} f_i \right) \right] = 0 \qquad (3.45)$$

Soil stiffness contribution from the element stiffness matrix is as follow:

$$K_{s,i} = -K_{bf,i} K_{f,i}^{-1} K_{bf,i}^t \qquad (3.46)$$

Depending on the degree of interpolation for soil reaction field, soil-stiffness contribution differs and it is presented by Jagodnik et al. [19].

3.3.3.5 Bernoulli-Winkler beam as shear-rigid Timoshenko's beam on Winkler's soil – three-field interpolation

Formulation of shear-rigid Timoshenko's beam element on Winkler's foundation follows the same principle of derivation of the Timoshenko's beam element as presented in Section 3.3.3.2 but with an addition of soil behaviour. Soil element equation can be written as:

$$K_{s,i} = \frac{kl_i}{2} \int_{-1}^{1} N^t \begin{bmatrix} 1 & 0 \\ 0 & 0 \end{bmatrix} N d\xi \qquad (3.47)$$

It has noted that although the stiffness matrix of a Bernoulli's beam element is the same as condensed mid-node shear-rigid Timoshenko's beam, soil contribution matrices are different [19].

3.3.3.6 Dual mixed FEM approach to Timoshenko's beam on Winkler's soil – four-field interpolation

Using the mixed **FEM** approach, the displacement, rotation, shear-stress resultant and distributed soil-reaction field have been interpolated as independent fields. Element equation can be written as:

$$\sum_{i=1}^{N_{el}} \Big[\delta p_i^t \left(K_{d,i} p_i + K_{dT,i} T_i + K_{bf,i} p_i \right. \tag{3.48}$$

$$\left. - R_i \right) + \delta T_i^t \left(K_{dT,i}^t p_i + K_{T,i} T_i \right) + \delta f_i^t \left(K_{bf,i}^t p_i + K_{f,i} f_i \right) \Big] = 0$$

After condensing out the mid node, the soil stiffness equation can be written as:

$$K_{s,i} = -K_{bf,i} K_{f,i}^{-1} K_{bf,i}^t. \tag{3.49}$$

Equation (3.50) shows the stiffness matrix for condensed mid-node of shear-rigid beam based on the equation (3.49) for the linear approximation of the distributed soil-reaction field, which gives best result compared to the analytical solution [19].

$$K_{s,i} = \frac{k l_i}{144} \begin{bmatrix} 48 & -6l & 24 & 6l \\ -6l & l^2 & -6l & -l^2 \\ 24 & -6l & 48 & 6l \\ 6l & -l^2 & 6l & l^2 \end{bmatrix}. \tag{3.50}$$

3.3.3.7 One-field interpolation of non-linear Winkler's soil

For a hyperelastic Winkler's soil, the total potential energy is given as $V = \frac{1}{2} \int_0^L EI(w'')^2 dx + \int_0^L u(w) dx - U$, where $u(w)$ is the one-dimensional strain-energy density of the deformation soil and U is the work of the applied loading. Applying the variational principle, and dividing the beam into N_{el} elements, from the principle of stationary total potential energy $\delta V = 0$ there follows:

$$\sum_{i=1}^{N_{el}} \delta \mathbf{p}_i^T \left(\mathbf{K}_{b,i} \mathbf{p}_i + \mathbf{F}_i - \mathbf{R}_i \right) = 0, \tag{3.51}$$

where, for an element i, $\mathbf{p}_i = \langle w_i, \theta_i, w_{i+1}, \theta_{i+1} \rangle^T$, $\mathbf{K}_{b,i} = \frac{8EI}{l_i} \int_{-1}^{1} \frac{d^2 \mathbf{N}_h^T}{d\xi^2} \frac{d^2 \mathbf{N}_h}{d\xi^2} d\xi$, $\mathbf{F}_i = \frac{l_i}{2} \int_{-1}^{1} \mathbf{N}_h^T f(w(\xi)) d\xi$, $\mathbf{N}_h$ is the matrix of Hermitean interpolation polynomials, $\mathbf{N}_i = \left\langle \frac{2(1-\xi)-\xi(1-\xi^2)}{4} \quad -\frac{l_i(1-\xi^2)(1-\xi)}{8} \quad \frac{(1+\xi)+\xi(1-\xi^2)}{4} \right.$

$\frac{l_i\left(1-\xi^2\right)(1+\xi)}{8}\Big\rangle$ and $\mathbf{R}_i$ is the nodal vector of the applied loading, while $f(w) = \frac{du(w)}{dw}$. $\mathbf{K}_{b,i}$ defined in this way, of course, yields the result already given in Section 3.3.3.1. Using (3.51), a non-linear element equilibrium can be expressed as:

$$\mathbf{g} \equiv \underbrace{\mathbf{K}_b\mathbf{p} + \mathbf{F}}_{\mathbf{q}_i} - \underbrace{\mathbf{R}}_{\mathbf{q}_e} = \mathbf{0}, \tag{3.52}$$

with $\mathbf{g}$ as the residual force vector and $\mathbf{K}_b$, $\mathbf{F}$ and $\mathbf{R}$ as the global beam stiffness matrix, the global soil-reaction vector and the global applied force vector. This residual force vector is non-linear in $\mathbf{p}$ through $\mathbf{F}$ and it my be expanded in a Taylor's series as:

$$\mathbf{g}(\mathbf{p} + \Delta\mathbf{p}) = \mathbf{g}(\mathbf{p}) + \Delta\mathbf{q}_i + O(\|\Delta\mathbf{p}\|^2), \tag{3.53}$$

from where the linearised equilibrium $\Delta\mathbf{q}_i = -\mathbf{g}$ follows as:

$$\Delta\mathbf{q}_i^i = \mathbf{K}_{b,i}\Delta\mathbf{p}_i + \frac{l_i}{2}\int_{-1}^{1}\mathbf{N}_h^T\frac{df}{dw}\mathbf{N}_h d\xi\Delta\mathbf{p}_i, \tag{3.54}$$

the contribution to $\Delta\mathbf{q}_i$ of element i. From (3.54) it can be easily concluded that the non-linear element stiffness matrix of the soil part of the mechanical system is

$$\mathbf{K}_{s,i} = \int_{-1}^{1}\frac{l_i}{2}\frac{df}{dw}\mathbf{N}_h^T\mathbf{N}_h d\xi. \tag{3.55}$$

Since $\mathbf{p}_i = 0$ in the initial configuration, both $\mathbf{K}_{b,i}\mathbf{p}_i$ the soil-reaction force vector $\mathbf{F}_i$ vanish and $-\mathbf{g} = \mathbf{R}$ are as in the linear analysis. Additionally, the value of the initial soil stiffness matrix $\mathbf{K}_{s,i}$ will be exactly the same as in the linear analysis with $\frac{df}{dw} = k_s$. The Newton-Raphson solution process to establish the equilibrium in the presently considered non-linear setting is given in Table 3.5.

3.3.3.8 Two-field interpolation on non-linear Winkler's soil

If the one field formulation is expanded by defining a two-field potential as $V^\star = V_b + V_{bf} - V_f - U$, where $V_b = \frac{1}{2}\int_0^L EI(w'')^2dx$, $V_{bf} = \int_0^L fwdx$ and

TABLE 3.5: Outline of the solution algorithm for one-field interpolation

Step	Description
(i)	Set the initial state for each element i
	$\mathbf{p}_i = \mathbf{0} \Rightarrow w = 0 \Rightarrow \mathbf{f} = 0 \Rightarrow \mathbf{F}_i = \mathbf{0}$ and $\frac{df}{dw}\big|_{w=0}$
(ii)	Calculate the element beam stiffness matrix $\mathbf{K}_{b,i}$ (Section 3.3.3.1) and the initial element soil stiffness matrix for each element i as:
	$\mathbf{K}_{s,i} = \int\limits_{-1}^{1} \frac{l_i}{2} \frac{df}{dw}\big|_{w=0} \mathbf{N}_h^T \mathbf{N}_h d\xi$
(iii)	Assemble the global stiffness and force vector and calculate the initial displacement:
	$\mathbf{K}\Delta\mathbf{p} = \mathbf{R}$
	where $\mathbf{K} = \mathbf{K}_s + \mathbf{K}_b$ and $\mathbf{R}$ are obtained from the element contributions
(iv)	Update the initial displacement vector
	$\mathbf{p} := \mathbf{p} + \Delta\mathbf{p}$ and extract the element new contributions $\mathbf{p}_i$
(v)	Calculate the displacement function and the soil-reaction and its derivative for element i
	$w(\xi)_i = \mathbf{N}_h \mathbf{p}_i$
	$f(w), \frac{df}{dw}$
(vi)	Calculate the soil-reaction vector for element i as:
	$\mathbf{F}_i = \frac{l_i}{2} \int\limits_{-1}^{1} \mathbf{N}_h^T \mathbf{f}(w) d\xi$
(vii)	Calculate the new soil stiffness matrix $\mathbf{K}_{s,i}$ for element i as $\mathbf{K}_{s,i} = \int\limits_{-1}^{1} \frac{l_i}{2} \frac{df}{dw}\big|_{w(\xi)} \mathbf{N}_h^T \mathbf{N}_h d\xi$
$(viii)$	Calculate the element unbalanced force vector as:
	$\mathbf{g}_i = \mathbf{K}_{b,i}\mathbf{p}_i^{(n+1)} + \mathbf{F}_i^{(n+1)} - \mathbf{R}_i$
(ix)	Assemble the global stiffness and residual and solve the equation of the system:
	$\mathbf{K}\Delta\mathbf{p} = -\mathbf{g}$
	where $\mathbf{K}$ and $\mathbf{g}$ are assembled from the element residual $\mathbf{q}_i$ and the element stiffness matrix $\mathbf{K}_i = \mathbf{K}_{b,i} + \mathbf{K}_{s,i}$
(x)	Repeat the procedure from step (iv) to step (ix) until the norm of the displacement increment $\|\Delta\mathbf{p}\|$ or the norm of the unbalanced force $\|\mathbf{g}\|$ is smaller than a prescribed tolerance

$V_f = \int_0^L u^\star(f)dx$ and where $u^\star(f) = \int_0^L w(\phi)d\phi$ is the one-dimensional comple-mentary strain energy density of the soil deformation. As it's explained in paper [19], it can be defined different interpolation functions for the displacement w and for the soil reaction f now. From $\delta V^\star = 0$, it follows:

$$\sum_{i=1}^{N_{\text{el}}} \left(\delta \mathbf{p}_i^T \mathbf{g}_i + \delta \mathbf{f}_i^T \mathbf{d}_i \right) = 0 \tag{3.56}$$

and where

$$\mathbf{g}_i = \mathbf{K}_{b,i}\mathbf{p}_i + \mathbf{F}_i - \mathbf{R}_i$$
$$\mathbf{d}_i = \mathbf{D}_i + \mathbf{D}_{f,i}$$

where

$$\mathbf{F}_i = \frac{l_i}{2} \int\limits_{-1}^{1} N_h^T f d\xi \tag{3.57}$$

$$\mathbf{D}_i = \frac{l_i}{2} \int\limits_{-1}^{1} N_f^T w d\xi \tag{3.58}$$

$$\mathbf{D}_{f,i} = -\frac{l_i}{2} \int\limits_{-1}^{1} N_h^T \frac{du^{star}}{df} d\xi \tag{3.59}$$

Since no derivation on f with respect to x (or ξ) exists in the mixed formulation $V^\star$, there is no need to establish continuity of f between the elements. For this reason, the equation (3.56) may be written as:

$$\delta \mathbf{p}^T \mathbf{q} + \sum_{i=1}^{N_{\text{el}}} \delta \mathbf{f}_i^T \mathbf{d}_i = 0 \tag{3.60}$$

which must hold true for any variations $\delta \mathbf{p}$ and $\delta \mathbf{f}_i$ thus leading to

$$\mathbf{g} = \mathbf{0}$$

$$\mathbf{d}_i = \mathbf{0}; \quad i = 1, \ldots, N_{\text{el}}.$$

In [19] it has been shown that the most efficient choice for N_f is the two-field formulation in linear analyses is $N_f = \langle 1 \;\; \xi \rangle$, which allows for a linear change of the soil-reaction field over an element.

A Newton-Raphson solution procedure may now be defined in the same manner as in the previous section starting from:

$$\Delta \mathbf{g} = -\mathbf{g} \tag{3.61}$$

$$\Delta \mathbf{d}_i = -\mathbf{d}_i, \quad i = 1, \ldots, N_{\text{el}}$$

where as described, the global residual g consists of the overlapping element contributions $\mathbf{g}_i$ owing to continuity of the displacement field. Likewise, its linear part Δg consists of the element contribution is:

$$\Delta \mathbf{g}_i = \mathbf{K}_{b,i} \Delta \mathbf{p}_i + \mathbf{K}_{bf,i} \Delta \mathbf{f}_i \tag{3.62}$$

where $\mathbf{K}_{bf,i} = \frac{l_i}{2} \int_{-1}^{1} \mathbf{N}_h^T \mathbf{N}_f d\xi$.

Also,

$$\Delta \mathbf{d}_i = \mathbf{K}_{bf,i}^T \Delta \mathbf{p}_i + \mathbf{K}_{f,i} \Delta \mathbf{f}_i \tag{3.63}$$

where $\mathbf{K}_{f,i} = -\frac{l_i}{2} \int_{-1}^{1} \frac{d^2 u^\star}{df^2} \mathbf{N}_f^T \mathbf{N}_f d\xi$.

Since $\Delta \mathbf{d}_i = -\mathbf{d}_i$ for every $i = 1, \ldots, N_{\text{el}}$ from (3.63) the increment of the soil-reaction force can be obtained as:

$$\Delta \mathbf{f}_i = -\mathbf{K}_{f,i}^{-1} \left(\mathbf{d}_i + \mathbf{K}_{bf,i}^T \Delta \mathbf{p}_i \right) \tag{3.64}$$

and substitute in 3.62 to obtain $\Delta \mathbf{g}_i$ in terms of $\Delta \mathbf{p}_i$ only as

$$\Delta \mathbf{g}_i = \mathbf{K}_i \Delta \mathbf{p}_i - \mathbf{e}_i \tag{3.65}$$

where

$$\mathbf{K}_i = \mathbf{K}_{b,i} - \mathbf{K}_{bf,i} \mathbf{K}_{f,i}^{-1} \mathbf{K}_{b,i}^T \tag{3.66}$$

$$\mathbf{e}_i = \mathbf{K}_{bf,i} \mathbf{K}_{f,i}^{-1} \mathbf{d}_i \tag{3.67}$$

Applying the assembly procedure employed to form the global residual $\mathbf{g}$ from the elemental residuals $\mathbf{g}_i$ to the linear part of the element residuals $\Delta \mathbf{g}_i$ and substituing the result in 3.61 we obtain:

$$\mathbf{K} \Delta \mathbf{p} = -\mathbf{g} + \mathbf{e} \tag{3.68}$$

where the global $\mathbf{e}$ is obtained from the element vectors $\mathbf{e}_i$ in the same way and the global stiffness matrix $\mathbf{K}$ is obtained from the element contributions $\mathbf{K}_i$ in the standard way. An outline of the solution process is given with Table 3.6.

TABLE 3.6: Outline of solution algorithm for two-field interpolation

Step	Description
(i)	Set the initial state for each element i
	$\mathbf{p}_i = \mathbf{0} \Rightarrow w = 0 \Rightarrow \mathbf{D}_i = \mathbf{0}$
	$\mathbf{f}_i = \mathbf{0} \Rightarrow f = 0 \Rightarrow \mathbf{F}_i = \mathbf{0}$
	$\frac{du^\star}{df}\big|_{f=0} = 0 \Rightarrow \mathbf{D}_{f,i} = \mathbf{0}$
	$\frac{d^2 u^\star}{df^2}\big|_{f=0} = \cdots$
(ii)	Calculate the matrix $\mathbf{K}_{bf,i}$ and $\mathbf{K}_{f,i}$ which arises from equations (3.62) and (3.63) for each element
(iii)	Calculate the element stiffness matrix $\mathbf{K}_{b,i}$ (Section 3.3.3.1) and the initial element soil stiffness matrix for each element i as:
	$\mathbf{K}_{s,i} = -\mathbf{K}_{bf,i} \mathbf{K}_{f,i}^{-1} \mathbf{K}_{bf,i}^T \Rightarrow \mathbf{K}_i = \mathbf{K}_{b,i} + \mathbf{K}_{S,i}$
(iv)	Assemble the global stiffness matrix and force vector and calculate the initial displacements by solving the system equation:

$$\mathbf{K}\Delta\mathbf{p} = \mathbf{R}$$

where $\mathbf{K}$ and $\mathbf{R}$ are obtained from the respective element contributions

(v) Calculate the increment of the soil-reaction vector of degrees of freedom $\Delta\mathbf{f}_i$ using equation (3.64) for each element i

(vi) Update the displacement vector

$\mathbf{p} := \mathbf{p} + \Delta\mathbf{p}$ and extract the element contributions and update the soil reaction vector

$\mathbf{f}_i := \mathbf{f}_i + \Delta\mathbf{f}_i$ for each element i

(vii) Calculate the displacement function and the soil-reaction function for each element i

$w = \mathbf{N}_h\mathbf{p}_i$

$f = \mathbf{N}_f\mathbf{f}_i$

as well as $\frac{du^\star}{df} \equiv w(f)$ and $\frac{d^2u^\star}{df^2} \equiv \frac{dw}{df}$

$(viii)$ Calculate the soil-reaction vector $\mathbf{F}_i$ for each element i using the updated soil-reaction function from step $(viii)$ using equation (3.57)

(ix) Compute the non-linear compatibility vector $\mathbf{d}_i$ using relations (3.58) and (3.59) for the updated soil-reaction function calculated in step $(viii)$ for each element i

(x) Calculate the soil-reaction matrix $\mathbf{K}_{f,i}$ using $\frac{d^2u^\star}{df^2}$ from step $(viii)$ for each element i

(xi) Calculate the new element stiffness matrix

$\mathbf{K}_i = \mathbf{K}_{b,i} - \mathbf{K}_{bf,i}\mathbf{K}_{f,i}^{-1}\mathbf{K}_{bf,i}^T$

(xii) Compute the condensed element unbalanced force vector as:

$\bar{\mathbf{g}}_i = \mathbf{K}_{b,i}\mathbf{p}_i + \mathbf{F}_i - \mathbf{R}_i - \mathbf{e}_i$

$(xiii)$ Assemble the global stiffness matrix and the unbalanced force vector and solve the system:

$\mathbf{K}\Delta\mathbf{p} = \bar{\mathbf{g}}$

(xiv) Repeat the procedure from step (vii) to step $(xiii)$ until the norm of the displacement increment $\|\Delta\mathbf{p}_i\|$, each of the norms of soil-reaction force increment $\|\Delta\mathbf{f}_i\|$ and/or the norm of the condensed unbalanced force vector $\|\bar{\mathbf{g}}_i\|$ is smaller than a prescribed tolerance

3.3.3.9 Three-field interpolation on non-linear Winkler's soil

If the two-field formulation is expanded into three-field formulation as $V^* = V_d + V_{dT} - V_T + \int_0^L u(w)dx - U$ where $u(w)$ is one-dimensional strain energy such as presented in Subsection 3.3.3.7. From the stationary total potential energy $\delta V^* = 0$ it follows:

$$\sum_{i=1}^{N_{\text{el}}} \left[\delta \mathbf{p}_i^T \left(\mathbf{K}_{d,i}\mathbf{p}_i + \mathbf{K}_{dT,i}\mathbf{T}_i + \mathbf{K}_{s,i}\mathbf{p}_i - \mathbf{R}_i \right) + \delta \mathbf{T}_i^T \left(\mathbf{K}_{dT,i}^T \mathbf{p}_i + \mathbf{K}_{T,i}\mathbf{T}_i \right) \right] = 0 \quad (3.69)$$

Because $\mathbf{p}$ and $\mathbf{T}$ must hold true for any variation, equation (3.69) can be summarized into:

$$\sum_{i=1}^{N_{\text{el}}} \left(\mathbf{K}_{b,i}\mathbf{p}_i + \mathbf{F}_i^\star - \mathbf{R}_i \right) = 0 \quad (3.70)$$

where $\mathbf{F}_i^\star = \frac{l_i}{2} \int_{-1}^{1} \mathbf{N}^T \begin{bmatrix} 1 & 0 \\ 0 & 0 \end{bmatrix} \frac{du}{dw} d\xi$, and $\mathbf{N}$ stands for matrix of Lagrangian interpolation polynomials [19, 59, 67]. Non-linear element equilibrium can be expressed as:

$$\mathbf{g} \equiv \underbrace{\mathbf{K}_b\mathbf{p} + \mathbf{F}^\star}_{q_i} - \underbrace{\mathbf{R}}_{q_e} = \mathbf{0} \quad (3.71)$$

From the linearised equilibrium, such as in Subsection 3.3.3.7, $\Delta\mathbf{q}_i = -\mathbf{g}$, it follows as:

$$\Delta\mathbf{q}_i = \mathbf{K}_{b,i}\Delta\mathbf{p}_i + \frac{l_i}{2} \int_{-1}^{1} \mathbf{N}^T \begin{bmatrix} 1 & 0 \\ 0 & 0 \end{bmatrix} \mathbf{N} \frac{df}{dw} d\xi \Delta\mathbf{p}_i \quad (3.72)$$

the contribution to $\Delta\mathbf{q}_i$ of element i. From equation (3.72) it can be easily concluded what is the non-linear stiffness matrix of soil part of system.

$$\mathbf{K}_{s,i} = \frac{l_i}{2} \int_{-1}^{1} \mathbf{N}^T \begin{bmatrix} 1 & 0 \\ 0 & 0 \end{bmatrix} \mathbf{N} \frac{df}{dw} d\xi \quad (3.73)$$

The procedure to obtaining $\Delta \mathbf{p}_i$ is a little bit more complex than the one in sections 3.3.3.7 and 3.3.3.8 since the matrices $\mathbf{K}_{b,i}$ and $\mathbf{K}_{s,i}$ are *6 by 6* matrix, thus the vector $\Delta \mathbf{p}_i$ is *6 by 1* vector. In order to calculate using shear-rigid finite element, so that the beam stiffness matrix can be comparable to Bernoulli's beam stiffness matrix, internal node of Timoshenko's beam-soil element has to be condensed out. An outline of solution process for this type of element is presented with Table 3.7.

TABLE 3.7: Outline of solving algorithm for three-field interpolation

Step	Description
(i)	Set the initial state for each element i
	$\mathbf{p}_i = \mathbf{0} \Rightarrow w = 0$
	$\mathbf{f}_i = \mathbf{0} \Rightarrow \mathbf{F}_i^\star = \mathbf{0}$
(ii)	Calculate tbe beam stiffness matrix $K_{b,i}$ (Section 3.3.3.1) and the initial element soil stiffness matrix for each element i as:
	$\mathbf{K}_{s,i} = \frac{l_i}{2} \int_{-1}^{1} \mathbf{N}^T \begin{bmatrix} 1 & 0 \\ 0 & 0 \end{bmatrix} \mathbf{N} \frac{df}{dw}\vert_{\mathbf{f}=0} \; d\xi$
	and caculate the beam-soil stiffness matrix as:
	$\mathbf{K} = \mathbf{K}_b + \mathbf{K}_s$ and $\mathbf{R}$ for each element contributions
(iii)	Preform the condensation of *6 by 6* system of beam-soil stiffness matrix for each element i using the relation $\begin{bmatrix} \mathbf{K}_{11} & \mathbf{K}_{12} & \mathbf{K}_{13} \\ \mathbf{K}_{21} & \mathbf{K}_{22} & \mathbf{K}_{23} \\ \mathbf{K}_{31} & \mathbf{K}_{32} & \mathbf{K}_{33} \end{bmatrix} \xrightarrow{conde.} \begin{bmatrix} \mathbf{A} & \mathbf{B} \\ \mathbf{B}^T & \mathbf{K}' \end{bmatrix}$
	with $\mathbf{A} = \mathbf{K}_{22}$, $\mathbf{B} = \begin{bmatrix} \mathbf{K}_{12}^T & \mathbf{K}_{23} \end{bmatrix}$, $\mathbf{K}' = \begin{bmatrix} \mathbf{K}_{11} & \mathbf{K}_{13} \\ \mathbf{K}_{13}^T & \mathbf{K}_{33} \end{bmatrix}$
	thus obtaining the system of equation $\left(\underbrace{\mathbf{K}'_m - \mathbf{B}_m^T \mathbf{A}_m^{-1} \mathbf{B}_m}_{\mathbf{K}_{sk,i}} \right) \Delta \mathbf{p}_{v,i} = \delta \mathbf{q}_i$

where $K_{sk,i}$ is *4 by 4* initial stiffness matrix of a condense-out three-noded Timoshenko element, $\delta \mathbf{q}_i$ is unbalanced element force vector and is defined as $\delta \mathbf{q}_i^{ini} = \left(\mathbf{B}_m^T \mathbf{A}_m^{-1} \mathbf{A}_b - \mathbf{B}_b^T \right) \mathbf{p}_{u,i} + \left(\mathbf{B}_m^T \mathbf{A}_m^{-1} \mathbf{B}_b - \mathbf{K}_b' \right) \mathbf{p}_{v,i} - \mathbf{B}_m^T \mathbf{A}_m^{-1} \left(\mathbf{R}_{u,i} - \mathbf{F}_{u,i} \right) + \mathbf{R}_{v,i} - \mathbf{F}_{v,i}$ and $\Delta \mathbf{p}_{v,i} = \left\{ \begin{array}{c} \Delta \mathbf{p}_{v,1} \\ \Delta \mathbf{p}_{v,2} \end{array} \right\}$ is the displacement vector of two noded shear rigid Timoshenko beam element Applying the limit $GA \rightarrow \infty$ to above relations we can obtain *4 by 4* beam-soil shear-rigid stiffness matrix. Assemble the global stiffness matrix of the beam-soil element and force vector $\delta \mathbf{q}$ for each element contributions

(iv) From step (iii) $\Delta \mathbf{p}_v$ is obtained which represents the outer node unknowns of an element. Extract the element contributions $\Delta \mathbf{p}_{v,i}$

(v) Calculate the displacement of internal element node for each element i as:
$$\Delta \mathbf{p}_{u,i} = -\mathbf{A}_m^{-1} \mathbf{A}_b \mathbf{p}_{u,i} - \mathbf{A}_m^{-1} \mathbf{B}_b \mathbf{p}_{v,i} + \mathbf{A}_m^{-1} \left(\mathbf{R}_{u,i} - \mathbf{F}_{u,i} \right) - \mathbf{A}_m^{-1} \mathbf{B}_m \Delta \mathbf{p}_{v,i}$$

(vi) Assemble the increment of *6 by 1* displacement vector $\Delta \mathbf{p}_i$ as:
$$\Delta \mathbf{p}_i = \left\{ \begin{array}{c} \Delta \mathbf{p}_{v,1} \\ \Delta \mathbf{p}_u \\ \Delta \mathbf{p}_{v,2} \end{array} \right\}$$

(vii) Update the initial displacement vector for each element
$$\mathbf{p}_i := \mathbf{p}_i + \Delta \mathbf{p}_i$$

$(viii)$ Calculate the displacement function and the soil-reaction function for each element
$$w = \mathbf{N} \left\{ \begin{array}{c} 1 \\ 0 \end{array} \right\} \mathbf{p}_i$$
and f_i

(xi) Calculate the soil-reaction vector as for each element i:

$$F_i^\star = \tfrac{l_i}{2} \int\limits_{-1}^{1} \mathbf{N}^T \begin{Bmatrix} 1 \\ 0 \end{Bmatrix} f_i d\xi$$

(x) Calculate the updated soil stiffness matrix from updated values in step (xi) for each element i:

$$\mathbf{K}_{s,i} = \tfrac{l_i}{2} \int_{-1}^{1} \mathbf{N}^T \begin{bmatrix} 1 & 0 \\ 0 & 0 \end{bmatrix} \mathbf{N} \tfrac{df}{dw}|_{\mathbf{f}_i} \ d\xi$$

(xi) Calculate the unbalanced force vector as:
$\delta\mathbf{q}_i^n = \left(\mathbf{B}_m^T \mathbf{A}_m^{-1} \mathbf{A}_b - \mathbf{B}_b^T\right) \mathbf{p}_{u,i} + \left(\mathbf{B}_m^T \mathbf{A}_m^{-1} \mathbf{B}_b - \mathbf{K}_b'\right) \mathbf{p}_{v,i} - \mathbf{B}_m^T \mathbf{A}_m^{-1} \left(\mathbf{R}_{u,i} - \mathbf{F}_{u,i}\right) + \mathbf{R}_{v,i} - \mathbf{F}_{v,i}$
for each element i

(xii) Perform the condensation of a system according to step (iii) thus obtaining updated condensed beam-soil stiffness matrix $\mathbf{K}_{sk,i}$ and unbalanced forced vector $\delta\mathbf{q}_i$, for each element i

$(xiii)$ Assemble the global system of equation and solve it:
$\mathbf{K}_{sk}\Delta\mathbf{p}_v = -\delta\mathbf{q}$

(xiv) Repeat the procedure from step (iv) to step $(xiii)$ until the norm of the displacement increment $\|\Delta\mathbf{p}_i\|$, or the norm of the unbalanced force $\|\delta\mathbf{q}_i\|$ is smaller than prescribed tolerance

3.3.3.10   Four-field interpolation on non-linear Winkler's soil

Four-field potential can be defined as the combination of two-field potential and three-field potential. Interpolation function for beam is considered to be as in previous section 3.3.3.9 described with Lagrangian polynomials, $\mathbf{N}$, while soil can be considered with constant or linear interpolation function $\mathbf{N}_f$ [19]. Following the conclusions from [19], the most efficient choice for four-field formulation is also $N_f = \langle 1 \ \xi \rangle$ such as described in Subsection 3.3.3.8. Energy potential can be defined as: $V^{**} = V_d + V_{dT} - V_T + \int_0^L fw dx + \int_0^L u^*(f) dx - U$ where $u^*(f) = \int_0^f w(f) df$ is one-dimensional complementary strain energy density such as presented in Subsection 3.3.3.8. Applying the variational principle, from $\delta V^{**} = 0$ it follows:

$$\sum_{i=1}^{N_{\text{el}}} \left[\delta \mathbf{p}_i^T \left(\mathbf{K}_{d,i} \mathbf{p}_i + \mathbf{K}_{dT,i} \mathbf{T}_i + \mathbf{K}_{bf,i} \mathbf{p}_i - \mathbf{R}_i \right) \right. \tag{3.74}$$
$$\left. + \delta \mathbf{T}_i^T \left(\mathbf{K}_{dT,i}^T \mathbf{p}_i + \mathbf{K}_{T,i} \mathbf{T}_i \right) + \delta \mathbf{f}_i^T \left(\mathbf{K}_{bf,i}^T \mathbf{p}_i + \mathbf{K}_{f,i} \mathbf{f}_i \right) \right] = 0$$

or shortly

$$\sum_{i=1}^{N_{\text{el}}} \left(\delta \mathbf{p}_i^T \mathbf{g}_i + \delta \mathbf{f}_i^T \mathbf{d}_i \right) = 0 \tag{3.75}$$

where

$$\mathbf{g}_i = \mathbf{K}_{b,i} \mathbf{p}_i + \mathbf{F}_i^* - \mathbf{R}_i$$
$$\mathbf{d}_i = \mathbf{D}_i + \mathbf{D}_{f,i}$$

and where

$$\mathbf{F}_i^\star = \frac{l_i}{2} \int_{-1}^{1} \mathbf{N}^T \begin{Bmatrix} 1 \\ 0 \end{Bmatrix} \frac{du}{dw} d\xi \tag{3.76}$$

$$\mathbf{D}_i = \frac{l_i}{2} \int_{-1}^{1} \mathbf{N}_{f,i}^T w \, d\xi \tag{3.77}$$

$$\mathbf{D}_{f,i} = -\frac{l_i}{2} \int_{-1}^{1} \mathbf{N}_{f,i}^T \frac{du^\star}{df} d\xi. \tag{3.78}$$

Such as presented in Subsection 3.3.3.8, since no derivation on f with respect to x (or ξ) exists in the mixed formulation V^{**}, there is no need to establish continuity of f between the elements. For this reason, equation (3.75) may be written as:

$$\delta \mathbf{p}^T \mathbf{q} + \sum_{i=1}^{N_{\text{el}}} \delta \mathbf{f}_i^T \mathbf{d}_i = 0 \tag{3.79}$$

which must hold true for any variations $\delta \mathbf{p}$ and $\delta \mathbf{f}_i$ thus leading to

$$\mathbf{g} = \mathbf{0}$$

$$\mathbf{d}_i = \mathbf{0}; \quad i = 1, \ldots, N_{\text{el}}.$$

A Newton-Raphson solution procedure may be defined now in the same manner as in the previous section starting from:

$$\Delta \mathbf{g} = -\mathbf{g} \tag{3.80}$$

$$\Delta \mathbf{d}_i = -\mathbf{d}_i, \quad i = 1, \ldots, N_{\text{el}}$$

where as it is described, the global residual $\mathbf{g}$ consists of the overlapping element contributions $\mathbf{g}_i$ owing to continuity of the displacement field, as it is stated in Subsection 3.3.3.8. Likewise, its linear part $\Delta \mathbf{g}$ consists of the element contributions:

$$\Delta \mathbf{g}_i = \mathbf{K}_{b,i} \Delta \mathbf{p}_i + \mathbf{K}_{bf,i} \Delta \mathbf{f}_i \tag{3.81}$$

where $\mathbf{K}_{bf,i} = \frac{l_i}{2} \int_{-1}^{1} \mathbf{N}^T \mathbf{N}_f d\xi$.

Here also,

$$\Delta \mathbf{d}_i = \mathbf{K}_{bf,i}^T \Delta \mathbf{p}_i + \mathbf{K}_{f,i} \Delta \mathbf{f}_i \tag{3.82}$$

where $\mathbf{K}_{f,i} = -\frac{l_i}{2} \int_{-1}^{1} \frac{d^2 u^*}{df^2} \mathbf{N}_f^T \mathbf{N}_f d\xi$.

Since again $\Delta \mathbf{d}_i = -\mathbf{d}_i$ now for every $i = 1, \ldots, N_{\text{el}}$ it can be obtained from 3.82 the increment of the soil-reaction force as:

$$\Delta \mathbf{f}_i = -\mathbf{K}_{f,i}^{-1} \left(\mathbf{d}_i + \mathbf{K}_{bf,i}^T \Delta \mathbf{p}_i \right) \tag{3.83}$$

and substitute in the same manner such as presented in Subsection 3.3.3.8 in (3.81) to obtain $\Delta \mathbf{g}_i$ in terms of $\Delta \mathbf{p}_i$ as

$$\Delta \mathbf{g}_i = \mathbf{K}_i \Delta \mathbf{p}_i - \mathbf{e}_i \tag{3.84}$$

where

$$\mathbf{K}_i = \mathbf{K}_{b,i} - \mathbf{K}_{bf,i}\mathbf{K}_{f,i}^{-1}\mathbf{K}_{b,i}^T \tag{3.85}$$

$$\mathbf{e}_i = \mathbf{K}_{bf,i}\mathbf{K}_{f,i}^{-1}\mathbf{d}_i \tag{3.86}$$

Applying the assembly procedure employed to form the global residual $\mathbf{g}$ from the elemental residuals $\mathbf{g}_i$ to the linear part of the element residuals $\Delta\mathbf{g}_i$ and substituting the result in 3.80 it will be obtained:

$$\mathbf{K}\Delta\mathbf{p} = -\mathbf{g} + \mathbf{e} \tag{3.87}$$

where the global $\mathbf{e}$ is obtained from the element vectors $\mathbf{e}_i$ in the same way and the global stiffness matrix $\mathbf{K}$ is obtained from the element contributions $\mathbf{K}_i$ in the standard way. It has to be noted that the obtained matrices are in size *6 by 6* and vectors are in size *6 by 1*. In order to compare Bernoulli's beam element and Timoshenko's beam element, the internal node of Timoshenko's beam element has to be condensed out in certain point of calculation, thus making the stiffness matrix in size *4 by 4*. An outline of the solution process is given with Table 3.8.

TABLE 3.8: Outline of solution algorithm for four-field interpolation

Step	Description
(i)	Set the initial state for each element i
	$\mathbf{p}_i = \mathbf{0} \Rightarrow w = 0 \Rightarrow \mathbf{D}_i = \mathbf{0}$
	$\mathbf{f}_i = \mathbf{0} \Rightarrow f = 0 \Rightarrow \mathbf{F}_i = \mathbf{0}$
	$\frac{du^\star}{df}\big|_{f=0} = 0 \Rightarrow \mathbf{D}_{f,i} = \mathbf{0}$
	$\frac{d^2u^\star}{df^2}\big|_{f=0} = \cdots$
(ii)	Calculate the matrices $\mathbf{K}_{bf,i}$ and $\mathbf{K}_{f,i}$ which arises from equations (3.81) and (3.82) for each element i
(iii)	Calculate the the beam element stiffness matrix $\mathbf{K}_{b,i}$ and the initial soil stiffness matrix for each ekement i as: $\mathbf{K}_{s,i} = -\mathbf{K}_{bf,i}\mathbf{K}_{f,i}^{-1}\mathbf{K}_{bf,i}^T$

The soil stiffness matrix $\mathbf{K}_{s,i}$ and beam-soil stiffness matrix $\mathbf{K}_i = \mathbf{K}_{s,i} + \mathbf{K}_{b,i}$ are *6 by 6* stiffness matrices like the ones in section 3.3.3.9. Thus, the similar procedure for obtaining increments of displacement has to be performed with the addition of beam-soil vector force 3.86

(iv) Preform the condensation of *6 by 6* system of equations on the equation (3.87) to form *4 by 4* system of equations using the following relation

$$\begin{bmatrix} \mathbf{K}_{11} & \mathbf{K}_{12} & \mathbf{K}_{13} \\ \mathbf{K}_{21} & \mathbf{K}_{22} & \mathbf{K}_{23} \\ \mathbf{K}_{31} & \mathbf{K}_{32} & \mathbf{K}_{33} \end{bmatrix} \xrightarrow{conde.} \begin{bmatrix} \mathbf{A} & \mathbf{B} \\ \mathbf{B}^T & \mathbf{K}' \end{bmatrix}$$

with $\mathbf{A} = \mathbf{K}_{22}$, $\mathbf{B} = \begin{bmatrix} \mathbf{K}_{12}^T & \mathbf{K}_{23} \end{bmatrix}$, $\mathbf{K}' = \begin{bmatrix} \mathbf{K}_{11} & \mathbf{K}_{13} \\ \mathbf{K}_{13}^T & \mathbf{K}_{33} \end{bmatrix}$

thus obtaining the system of equation

$$\left(\underbrace{\mathbf{K}'_m - \mathbf{B}_m^T \mathbf{A}_m^{-1} \mathbf{B}_m}_{\mathbf{K}_{sk,i}} \right) \Delta \mathbf{p}_v = \delta \mathbf{q}_i$$

where $\bar{\mathbf{g}}_i = \left(\mathbf{B}_m^T \mathbf{A}_m^{-1} \mathbf{A}_b - \mathbf{B}_b^T \right) \mathbf{p}_{u,i} + \left(\mathbf{B}_m^T \mathbf{A}_m^{-1} \mathbf{B}_b - \mathbf{K}'_b \right) \mathbf{p}_{v,i} - \mathbf{B}_m^T \mathbf{A}_m^{-1} \left(\mathbf{R}_{u,i} + \mathbf{e}_{u,i} - \mathbf{F}_{u,i} \right) + \mathbf{R}_{v,i} - \mathbf{F}_{v,i} + \mathbf{e}_{v,i}$

and $\Delta \mathbf{p}_{v,i} = \left\{ \begin{array}{c} \Delta \mathbf{p}_{v,1} \\ \Delta \mathbf{p}_{v,2} \end{array} \right\}$

Applying the limit $GA \to \infty$ to above relations we can obtain *4 by 4* stiffness matrix for shear-rigid system.

Assemble the global stiffness matrix, displacement vector and force vector and solve the system

$$\mathbf{K}_{sk} \Delta \mathbf{p}_v = \bar{\mathbf{g}}$$

where $\mathbf{K}_{sk}$ and $\bar{\mathbf{g}}$ are obtained from the respectable element contributions.

(v) From step (iv) we obtain $\Delta \mathbf{p}_v$ which represents the outer node unknowns of an element. Extract the element contributions $\Delta \mathbf{p}_{v,i}$

(vi) Calculate the displacement of internal element node as:

$$\Delta \mathbf{p}_{u,i} = -\mathbf{A}_m^{-1}\mathbf{A}_b\mathbf{p}_{u,i} - \mathbf{A}_m^{-1}\mathbf{B}_b\mathbf{p}_{v,i} + \mathbf{A}_m^{-1}\left(\mathbf{R}_{u,i}\right.$$
$$\left. - \mathbf{F}_{u,i} + \mathbf{e}_{u,i}\right) - \mathbf{A}_m^{-1}\mathbf{B}_m\Delta\mathbf{p}_{v,i}$$

(vii) Assemble the increment of *6 by 1* displacement vector $\Delta\mathbf{p}_i$ as:

$$\Delta\mathbf{p}_i = \left\{ \begin{array}{c} \Delta\mathbf{p}_{v,1} \\ \Delta\mathbf{p}_u \\ \Delta\mathbf{p}_{v,2} \end{array} \right\} \text{ for each element contribution}$$

$(viii)$ Calculate the increment of soil-reaction function using the relation $\Delta\mathbf{f}_i$ given with equation (3.83) for each element contribution

(ix) Update the initial displacement vector
$$\mathbf{p} := \mathbf{p}_i + \Delta\mathbf{p}_i$$
$$\mathbf{f}_i = \mathbf{f}_i + \Delta\mathbf{f}_i$$
as well as $\frac{du^*}{df} \equiv w(f)$ and $\frac{d^2u^*}{df^2} \equiv \frac{dw}{df}$

(x) Calculate the displacement function and soil-reaction function
$$w = \mathbf{N}\mathbf{p}_i$$
$$f = \mathbf{N}_f\mathbf{f}_i$$

(xi) Calculate the soil-reaction vector $\mathbf{F}_i^\star$ for each element i using the updated soil-reaction function from step (x) by equation (3.76)

(xii) Compute the non-linear compatibility vector $\mathbf{d}_i$ using the equations (3.77) and (3.78) for the updated soil-reaction function calculated in step (vii) for each element i

$(xiii)$ Calculate soil-reaction matrix $\mathbf{K}_{f,i}$ using $\frac{d^2u^*}{df^2}$ from step (xi) for each element i

(xiv) Calculate the new soil stiffness matrix $\mathbf{K}_{s,i}$ with the updated soil-reaction stiffness matrix $\mathbf{K}_{f,i}$ calculated in step $(xiii)$ for each element i

(xv) Compute the unbalanced force vector as:
$$\bar{\mathbf{g}}_i = \left(\mathbf{B}_m^T\mathbf{A}_m^{-1}\mathbf{A}_b - \mathbf{B}_b^T\right)\mathbf{p}_{u,i} + \left(\mathbf{B}_m^T\mathbf{A}_m^{-1}\mathbf{B}_b - \mathbf{K}_b'\right)\mathbf{p}_{v,i} - \mathbf{B}_m^T\mathbf{A}_m^{-1}\left(\mathbf{R}_{u,i} + \mathbf{e}_{u,i} - \mathbf{F}_{u,i}\right) + \mathbf{R}_{v,i} - \mathbf{F}_{v,i} + \mathbf{e}_{v,i}$$

(xvi) Perform the condensation of a system according to step (iv) thus obtaining updated condensed beam-soil stiffness matrix $\mathbf{K}_{sk,i}$ and unbalanced force vector $\delta\mathbf{q}_i$ for each element i

$(xvii)$ Assemble the condensed-out system matrix into global stiffness matrix and solve the system of equations:

$$\mathbf{K}_{sk,i}\Delta\mathbf{p}_v = \bar{\mathbf{g}}$$

$(xviii)$ Repeat the procedure from step (v) to step (xvi) until the norm of the displacement increment $\|\Delta\mathbf{p}_i\|$ or the norm of the unbalanced force $\|\mathbf{q}_i\|$ is smaller than prescribed tolerance

Chapter 4

Geotechnical test site characterization

Based on the presented analyses and testing performed by various authors, the testing field for research could be establish. Because no documented **LLP** tests in natural gravels were found, it was decided that the field tests would be performed in those type of soil. The piles will be embedded in cohesionless soil, made of alluvial deposits, mainly gravels with different content of sand. Because of the limiting funds it was decided that 10 piles in total would be constructed in mentioned soil. Axial distance form pile to pile is 3 times diameter of pile. The length of embedded pile is 5 m with 20 cm above ground level. The elevation of 20 cm above ground level is constructed to enable that the piles can be easily loaded. Loading of piles was achieved with hydraulic press. Since the length to diameter ratio is grater than 10, which means that the piles are flexible, and because it is the only device for measurement of displacement, incinometer probe is used for obtaining the displacement of the piles. The diameter of pile is taken as 0.25 with inner hole of 7cm for inlinometer casing. Pile is going to be made of concrete mixture. Detailed description of field, establishment of field testing and testing itself is given in Chapter 5 of this Thesis.

Location laterally loaded piles testing site, described in this chapter, was chosen because of its specific geological setting. Geological profile at the location consists of natural sandy gravels that were deposited in the past and this fact makes this kind of tests among the rare. As it mentioned before, **LLP** were

FIGURE 4.1: Location of test field

mostly tested in clays and sand, and there are just a few information about **LLP** testing and behaviour in natural sandy gravels.

4.1 Geographical position

The position of the test field is situated in the north-east outskirts of the town Rijeka, Grobnik, Croatia. Wider display of location is shown on the Figure 4.1.

4.2 Geological and geotechnical characteristics of test field location

The Grobnik Field is a vast karstic depression situated between the Riječina River Valley and mountains of Gorski Kotar. Shape of the field is irregular with maximum length about 4 km in west-east direction, and north-south direction. Altitude of Grobnik Field is lowering from north-east where it is about 325 m a.s.l. to 250 m a.s.l. on the south-west part. The Hum hill divides the Grobnik Field into its west and east parts.

Hills around the Grobnik Field are formed in the carbonate rocks of Cretaceous age. Those are limestone, dolomitic limestone and carbonate breccias. Palaeogene limestone and siliciclastic rock-marls and flysch are visible on the surface of south-west edge of the Grobnik Field [68, 69]. Geological map and legend are presented in Figure 4.2.

Fluvioglacial sediments cover the bottom of the Grobnik Fieldand caused that this depression has a characteristics of a karstic field. On the eastern part of the field, in the area of Kikovica and Dubine, the gravel cobble material prevails. Going toward the west, in the area of Dražice and Podhum, surface deposits are made of sands and gravels. Along the south and south-east edge of the Grobnik Field, fine sand and clayly sand start to prevail. The depth of those fluvioglacial sediment layers is approximately 25 m [70, 71].

Carbonate rocks around the field are fissured and karstified and they have a good water permeability characteristics. This is the area without permanent surface run-off and water circulation is present into deep karstic underground [72], but because of rising the underground water level, transgression of the Grobnik Field is periodic. Torrent flows can happen after heavy rain periods.
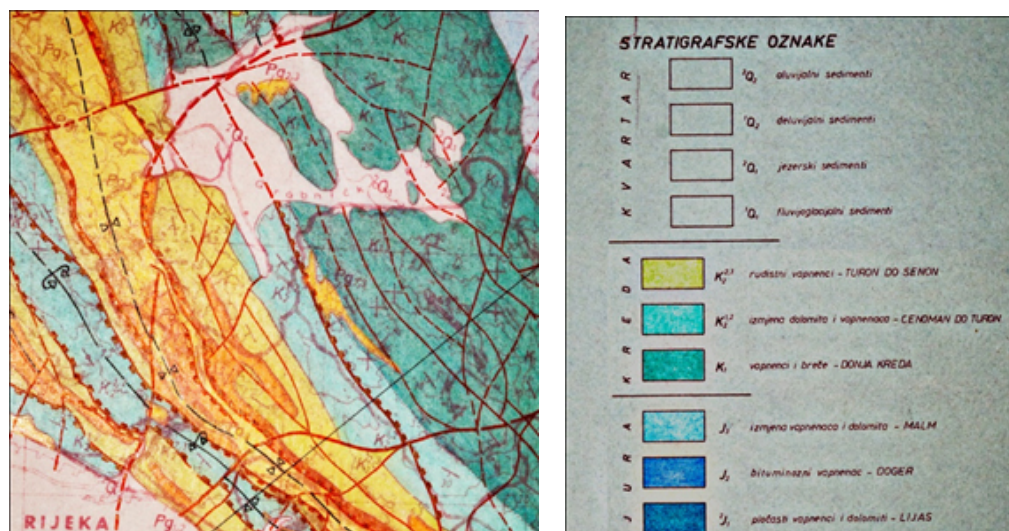

FIGURE 4.2: Geological map of field testing with legend, [73]

FIGURE 4.3: Material on a location

In general, geological profile can be divided into two parts: (a) superficial deposits, which consist of fluvial deposits and (b) bedrock, which is made of limestone. Fluvial deposits are well graded gravels with grain size up to 100 mm, with some elements of 250 mm in diameter. The depth of this layer of gravel material is from 10 m to 50 m at some locations. Upper part (20 cm below ground level) is made of clay, mostly organic deposits, which will be removed before testing. On Figure 4.3, the cut in natural gravel deposits are presented at a location near the testing field.

4.3   Ground water level

Since the superficial deposit is made mostly of granular soil, it has very high coefficient of permeability meaning that pore pressures cannot arise to the values which have influence to any kind of construction. After heavy rain, water can shortly remain at the surface, but usually runs away within some minutes.

4.4   Granulometric composition

From test site location, sandy gravel material was taken for sieve analysis. Procedures of sieving were based on Eurocode standards for such analysis [74].
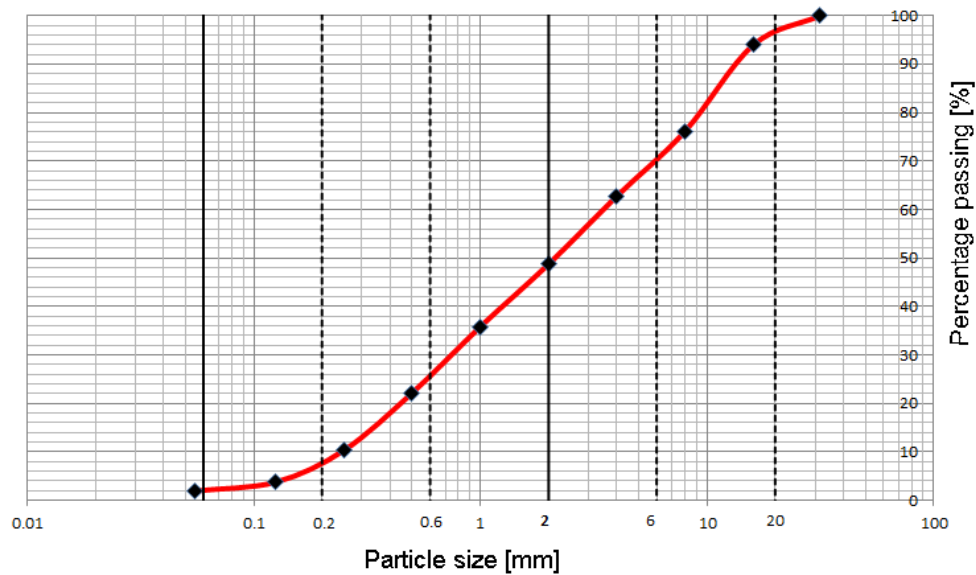
FIGURE 4.4: Granulometric composition diagram of gravel material from test location

On Figure 4.4 the result of sieve analysis is presented.

With the sieve analysis performed, uniformity coefficient and gradation coefficient could be obtained, given with equation (4.1) and (4.2), respectively. Based on that equations and sieve curve, coefficient of uniformity of gravel sample is 10 and coefficient of gradation is 0.9. In the most of the textbooks [75, 76, 77, 78] a well graded soil is the soil that has the coefficient of uniformity larger than 4 (if we talk about gravels) and 6 (if we talk about sands). Based on that fact, the analysed gravel is well graded. But, the limits of coefficient of gradation for soil to be well graded, is between 1 and 3. Bearing in mind the obtained results, analysed gravel is somewhere on a lower boundary which gives us the insight of the present amount of sand. Taking a look at the Figure 4.4, it can be concluded that the soil consists of nearly 50% of sand and 50% of gravel. That makes it a bit hard to distinguish what material will be dominant for pile behaviour. There are some evidence that the sand will be dominant in the mixture of sand and gravel if the specimen has more than 50% of sand [79].

$$C_u = \frac{D_{60}}{D_{10}} = 10 \qquad (4.1)$$

$$C_c = \frac{D_{30}^2}{D_{60} \cdot D_{10}} = 0.9 \qquad (4.2)$$
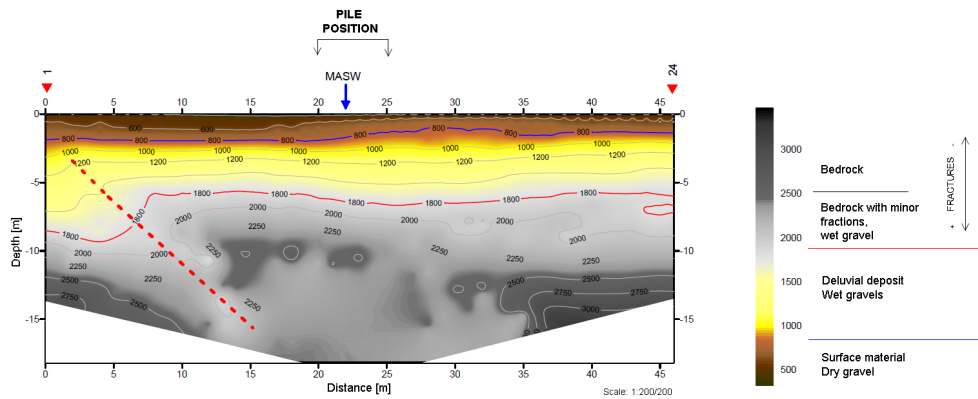
FIGURE 4.5: Seismic profile obtained by shallow seismic refraction survey
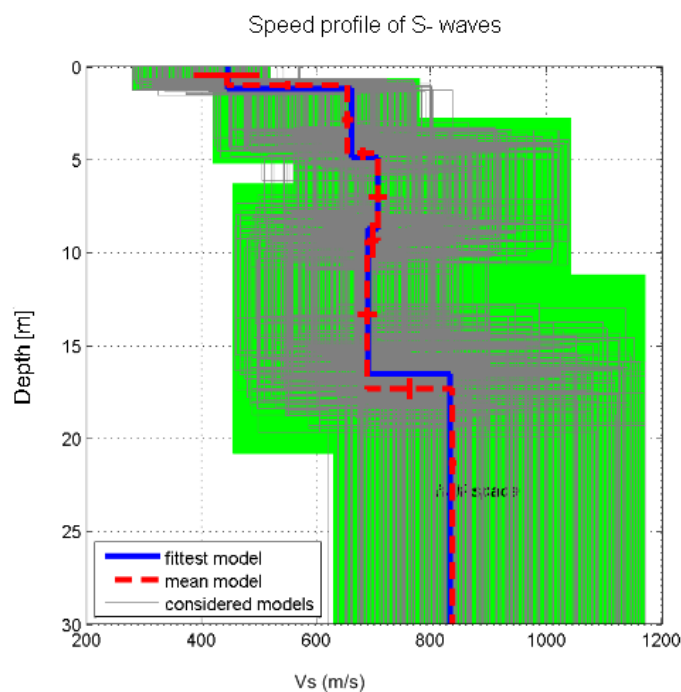
FIGURE 4.6: Plot of shear wave velocity with depth obtained from **MASW**

4.5 Geophysical survey on site

Basic geophysical survey on a site consists of shallow seismic refraction and multichannel analysis of surface waves (**MASW**). Techniques for mentioned geophysical testing surveys are described in Appendix C and D respectively. On Figure 4.5 the seismic profile obtained by shallow seismic refraction survey is presented, while on figure 4.6, shear wave velocity profile is plotted.
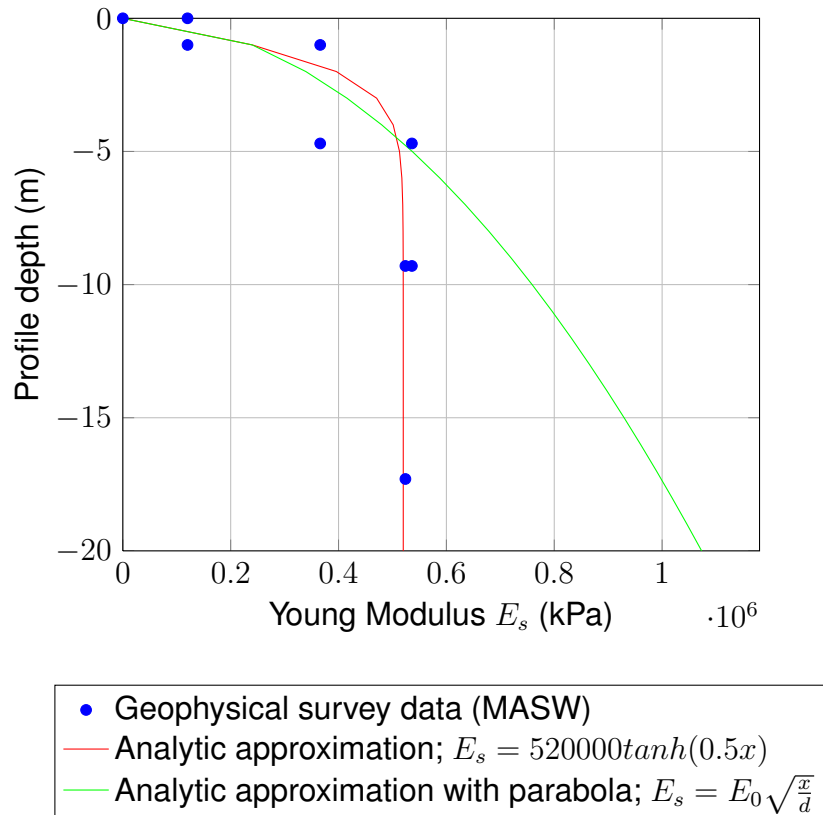
FIGURE 4.7: Distribution of static Young modulus through depth

Based on shear wave velocities, dynamic deformation parameters of naturally sandy gravels were calculated, and summarised in Table 4.1.

TABLE 4.1: Deformation parameters obtained by geophysical testing

Depth [m]	v_s [m/s]	ρ [g/cm^3]	G_{din} [MPa]	E_{din} [MPa]	E_{stat} [MPa]
0.0 - 1.0	444.0	1.7	335.13	600	120
1.0 - 4.7	655.0	1.9	815.15	1830	366
4.7 - 9.3	707.0	1.9	949.71	2680	536.4
9.3 - 17.3	689.0	1.9	901.97	2620	524
17.3 -	837	2.2	1541.25	4430	886

Static Young's modulus of soil was determinated as $E_{dyn}/5$ - $E_{dyn}/10$, based on some previous studies [80]. It depends on type of structure in soil [81] and the construction embedded in soil, and thus the existing deformation. Using that assumption, the change of static Young's modulus with depth can be calculated and it is presented in Figure 4.7. Functions approximate the changes of Young's soil modulus with depth are also plotted on that figure.

FIGURE 4.8: Large direct shear box at CEI

4.6 Laboratory testing of natural sandy gravel soil

Laboratory testing of material are carried out using a large direct shear box (Figure 4.8) at the Civil Engineering Institute of Croatia (CEI) in Zagreb. Top layout dimensions of the shear box are 0.35 m by 0.35 m with the hight of sample of 0.35 m. Vertical pressure was achieved with air pillow; maximum allowed vertical pressure is 400 kPa. Horizontal pressure was applied with electric motor; maximum horizontal pressure at the box is 400kPa. The test was conducted as a horizontal displacement control test with an increment of 1mm per 1 minute.

Four tests were conducted using four different vertical stresses: 50 kPa, 100 kPa, 150 kPa and 200 kPa. Shear stress vs. displacement curves are presented on Figure 4.9. On Figure 4.10, normal stresses vs. peak shear stress and normal stresses vs. residual shear stress are presented along with appropriate trendline representing the failure line and residual line.

Using results of four performed test basic soil behaviour parameters, cohesion and friction angle, can be calculated. Because of the type of material (mixture of sand and gravel) cohesion is equal to zero, and the friction angle is represented with the slope of failure line. The coefficient of slope of the failure line is $\tan \phi = 1.0304$ which is equivalent to the friction angle of $\phi \approx 46°$. The slope of residual line is $\tan \phi_r = 0.95$ giving the approxiamte angle of $\phi_r = 43°$ According to some authors like Bolton [82], Houlsby [83] and Wood [39, 84], angle of dilatancy
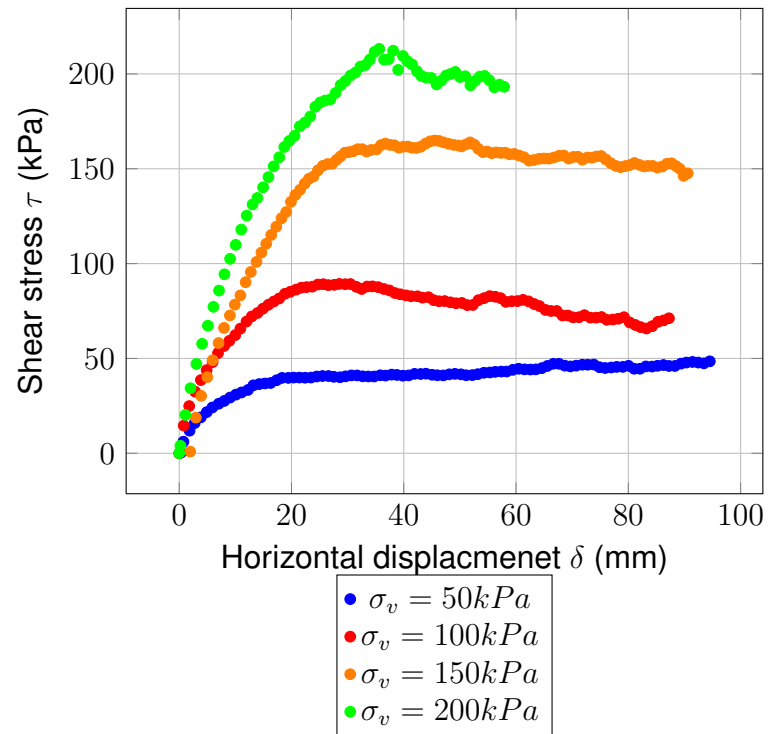
FIGURE 4.9: Shear stress vs. horizontal displacement for shear tests in large shear box

FIGURE 4.10: Peak and residual shear stresses vs. normal stresses with failure and residual lines

ψ can be calculated if peak and residual angle of friction is known using the following equation:

$$\phi = \phi_{cv} + 0.8 \cdot \psi \tag{4.3}$$

Using the obtained peak and residual angle obtained from shear tests and plugging them into the equation (4.3), the approximate angle of dilatancy is obtained as $\psi = 3.75°$.

Chapter 5

Experimental programme

5.1 Introduction

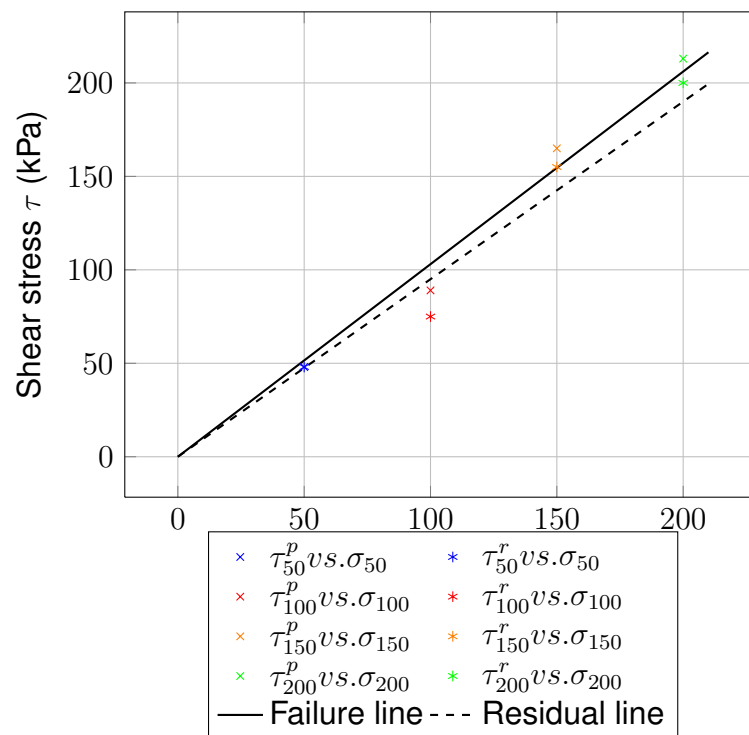In the following chapter the in-situ testing programme of **LLP** is presented and devised. The chapter consists of six sections without introduction part, (i) field test preferences, (ii) installation of inclinometer casings, (iii) installation of piles, (iv) installation of counterweight concrete block, (v) steel loading frame and (vi) testing procedure. Test field dimensions and constructions on the field will be presented. To determine the pile deflection, inclinometer probe will be used, by placing it to inclinometer casings installed in testing piles. The installation and position of inclinometer casings are presented in Section 5.4. The construction of piles, their cross-section, characteristics and dimensions are presented in Section 5.3. Piles are loaded laterally using the hydraulic press with capacity of 500kN. Load on pile is transferred via loading frame, described in Section 5.6, by counter-reaction using concrete block presented in Section 5.5. In the last section, the Section 5.7, the test procedure is presented.

5.2 Field test preferences

Test field consists of twelve in-situ bored and constructed concrete piles of which nine have inclinometer tube installed in the axis; seven inclinometer casings installed in soil profile away from piles to measure displacements of soil
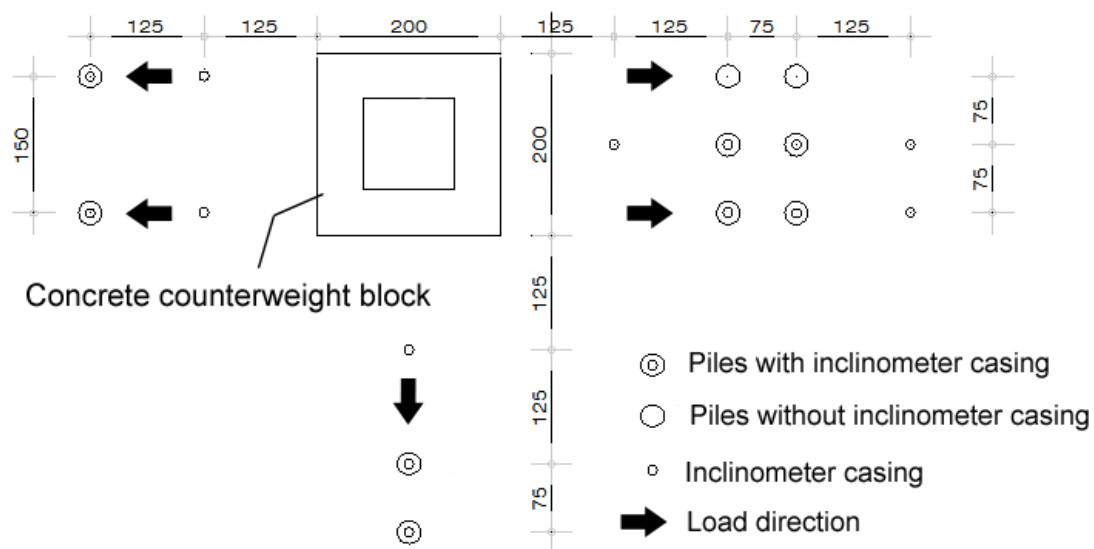
FIGURE 5.1: Test field schematic sketch
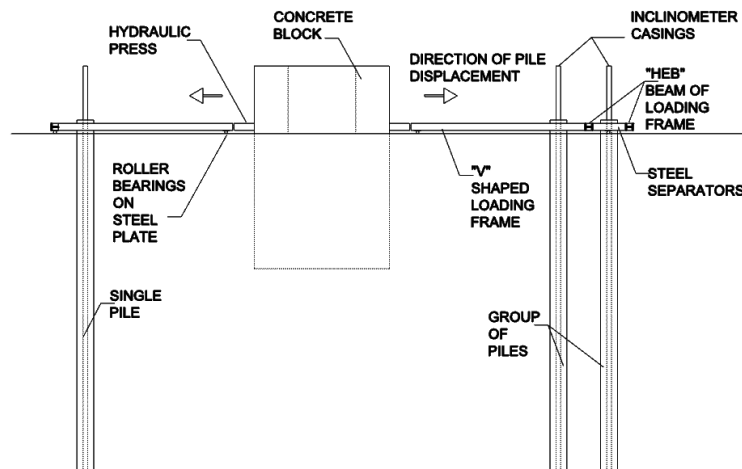
FIGURE 5.2: Cross-section of test field

around the piles and concrete block which is used as a counterweight force for loading the piles by means of loading frame. Sketch of test field is given on Figure 5.1, while test field cross-section is presented in Figure 5.2 . The axial distance between piles is chosen as three times the diameter of the pile, which was concluded to be the critical distance between the piles as it is mentioned in introduction of Chapter 4.

5.3   Installation of piles

As it is mentioned in the introduction of this chapter, within this section the pile installation will be presented. Section is divided into three subsections: (i) selection of pile length, (ii) the pile cross-section and (iii) pile instrumentation.

5.3.1   Selection of pile length

Basic idea for the selection of pile length pile testing regarding its length was to ensure a slender or flexible piles. Pile is flexible if the ratio of length to diameter of pile is larger than 10 [85]. Because of construction cost, the length of a pile is chosen to be 5m and its' diameter 25 cm, which gives slender ratio $L/D = 20$. Another way to check if the pile is flexible is to control its flexural rigidity in comparison to soil stiffness, given by Patra et al. [20]:

$$K_{RS} = \frac{E \cdot I}{E_s \cdot L^4} \tag{5.1}$$

$$1.8 \cdot (K_{RS})^{0.12} \leq 1 \tag{5.2}$$

If the left part of equation (5.2) is smaller then 1 then the piles behave as a flexible or slender pile. Taking into account the average Young's modulus of elasticity for concrete as $3.15 \cdot 10^7$ kPa, Young's modulus of soil as 120 MPa, the diameter of pile 25 cm with the inclinometer hole of 7 cm, left part of equation (5.2) is 0.59.

5.3.2   The pile cross-section

Piles have circular cross-section, 25 cm in diameter with a hole of 7 cm in which aluminium inclinometer casing will be installed. Pile reinforcing cage consists of 8 bars of $\phi16$ mm in diameter connected with spiral reinforcement Figure 5.3. Pile reinforcement is calculated and installed to ensure the pile stiffness. All above mentioned has been calculated based on maximum bending moment
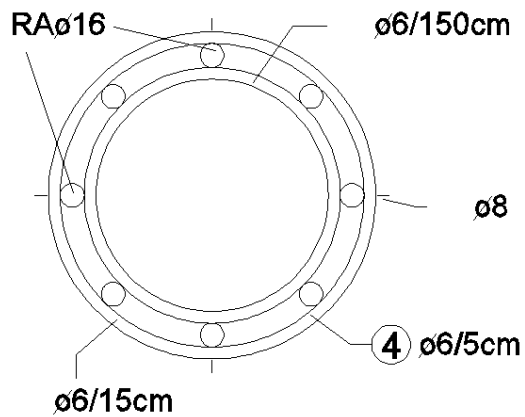
FIGURE 5.3: Pile reinforcement cross-section

FIGURE 5.4: Pile reinforcement

performed in some of previous analysis [73]. The reinforcing cage is shown on Figure 5.4.

5.3.3 Pile instrumentation

Regarding available measurement equipment, the measured deflection of a pile by inserting an inclinometer probe inside the inclinometer casing installed through the pile axis, as it shown on Figure 5.5, was accepted. The idea is to measure the deflection of a pile and by knowing its deflection to calculate

FIGURE 5.5: Pile installation

other useful data and define diagrams such as bending curves, and, the most important, diagrams of soil resistance along the piles.

Pile inclinometer casings are made of aluminium and delivered also in 3 m length elements. Inclinometer casings were connected the same way as standard plastic inclinometer casings with the connection parts made from aluminium.

5.4 Installation of inclinometer casings

Plastic inclinometer casings, made of acrylonitrile butadiene styrene, herein **ABS**, are installed in the test field in order to determine displacements in soil around the pile. Casings are embedded in soil 5.3m, 30 cm below the bottom of the pile. Six meter casing consists of two 3 m long parts connected using **ABS** connection, as shown in Figure 5.6. The installation of inclinometer casings in the field is shown in Figure 5.7.

Holes 10 cm in diameter and 5.3 m depth were bored with drilling rig, in which **ABS** inclinometer casings were placed an then grouted with the mixture of cement and water, Figure 5.8.

FIGURE 5.6: Six meter inclinometer ABS casings connected with ABS connection in the middle

FIGURE 5.7: Inclinometer casings arranged in test field

FIGURE 5.8: Drilling the inclinometer holes

5.5 Counterweight concrete block

The role of the concrete block is to ensure sufficient counterweight to enable lateral loading of piles. That was achieved using block mass and passive earth pressure. Figure 5.9 shows the forces acting on a concrete block. The acting force H that is induced with hydraulic press is balanced with block self-weight (W), passive pressure (P_p), soil resistance on block basis (F_b) and flanks (F_f). The dimensions of block are 2.0 by 2.0 meters in top view. Block is embedded in soil 2.0 m and it arises from the ground 1.0 m. From the 2.0 m – 0.5 m below ground line, block was made out of solid concrete while upper 1.5 m was made as a box 2 by 2 m with 0.5 m thick walls. Block reinforcement is shown in F 5.10, while completed block is shown in Figure 5.11. The hollow part of the block was filled with the excavated material.

5.6 Loading frame

Loading frame for load applying during the field testing consists of several elements which can be divided in structural and connection element. The schematic view of the loading frame is shown in Figure 5.12.
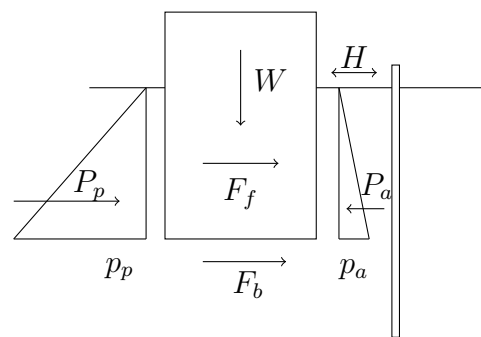
FIGURE 5.9: Schematic presentation of forces acting on concrete block

FIGURE 5.10: Counterweight block reinforcement
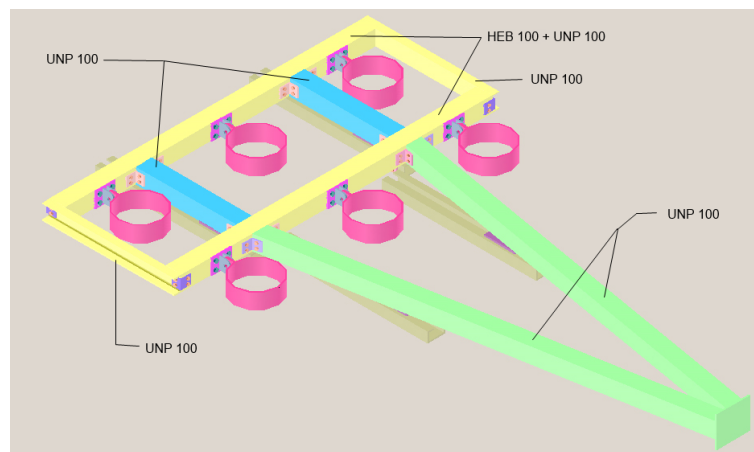
FIGURE 5.11: Completed counterweight block

FIGURE 5.12: Schematic view of loading frame

Loading frame consists of two horizontal beam made of HEB 100 steel elements, strengthen with the standard UNP 100 steel elements. The idea was to make the beam as rigid as it possible in the direction perpendicular to the direction of load applying and pile displacing. The distance between those two main beams is achieved by placing two box elements made of UNP 100 steel elements. The purpose of this elements is not only to make the distance between beams but as well to transfer load from "V" shaped load frame. The "V" shaped load frame is also made of double UNP 100 steel elements, and strengthen along its length with steel plates to avoid buckling of an element.

Special joint connections were made, to ensure connection between piles and
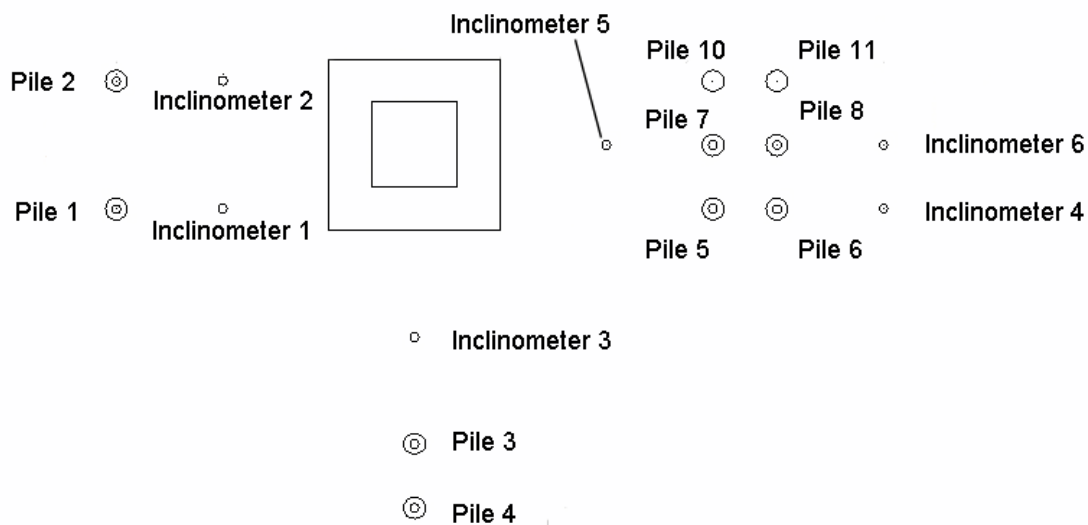
FIGURE 5.13: Labels of piles and inclinometer casing on the test field

the frame using pinned connections. Piles are connected to the loading frame with steel rings, 250 mm in the inner diameter, wall thickness 10 mm and length of 100 mm.

Most of the connection elements were planned and constructed as flexible connection to enable simple handling. Analyses and calculation for loading frame elements are presented in Appendix B.

5.7 Testing procedures

LLP field testing consists of five separate tests: (i) laterally loaded single pile test with monotonic displacement, (ii) laterally loaded single pile test with cyclic displacement (pile is loaded monotonically to some displacement and then unload until the force on the hydraulic press are equal to zero), (iii) laterally loaded group of *2 by 1* piles test with monotonic displacement, (iv) laterally loaded group of *2 by 3* piles test with monotonic displacement. The position of constructed piles and inclinometer casings is shown in Figure 5.13, where each pile with inclinometer casing has its label.

Piles are displaced by applying of a load from the hydraulic press to the "V" shaped loading frame and then further to steel beams whose function is to pull
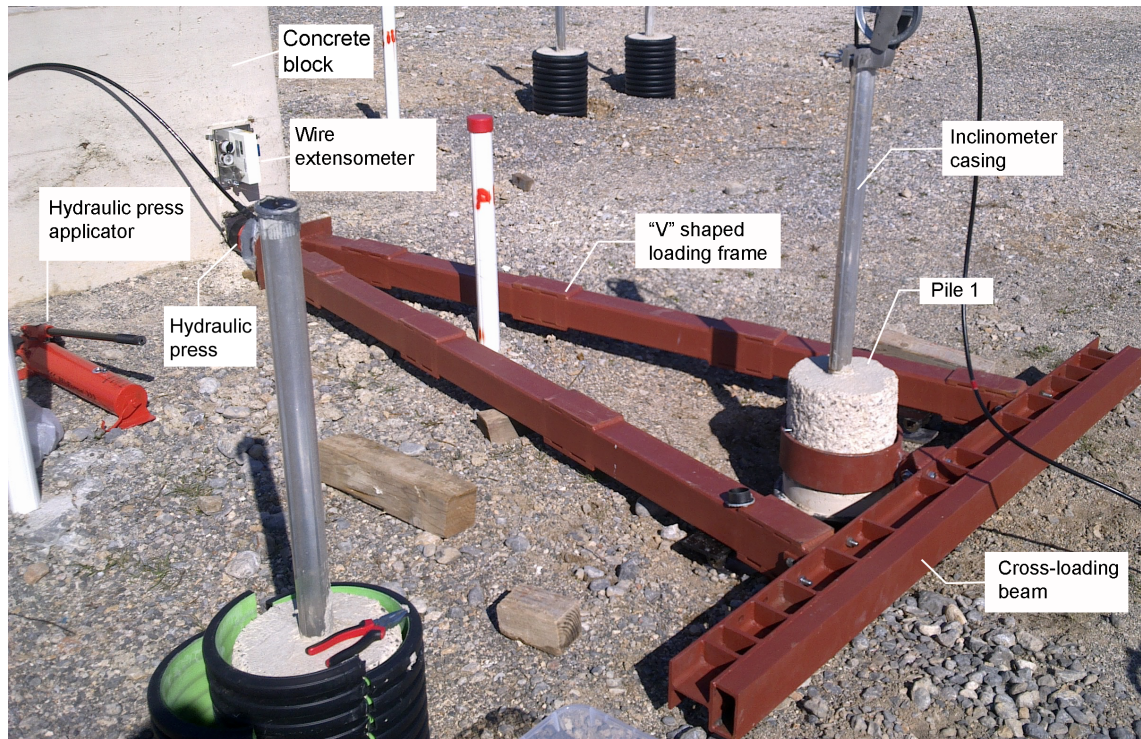
FIGURE 5.14: Prepared equipment for lateral load testing

the piles away from the concrete block as it marked with arrows on Figure 5.1. Installation of testing equipment on the field, with frame, hydraulic press and hydraulic applicator are presented on Figure 5.14 and 5.15, respectively.

The pressure in hydraulic press is formed by pumping in the fluid from hydraulic applicator, causing displacement of the loading frame and thus move the pile. Wire extensometer installed on counterweight block is connected to the pile head making it possible to ensure the measurement of pile head displacement. Loading of single piles and group of piles is performed with pile head displacement increment of 2 mm. The difference was only in test (ii), where the single pile is tested with cyclic displacements.
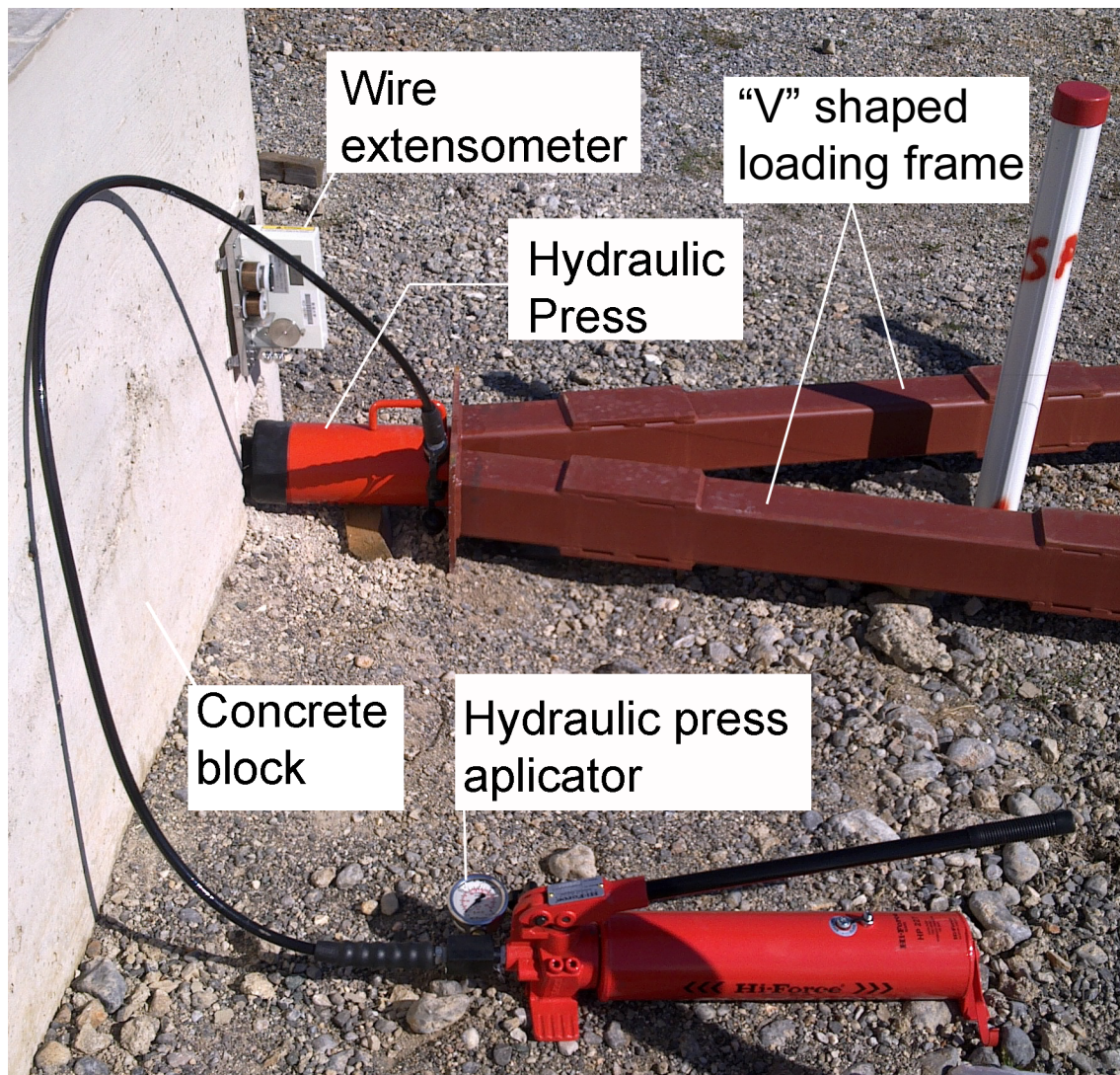
FIGURE 5.15: Position of hydraulic press and applicator during the pile testing

Chapter 6

Field test results

Results from the **LLP** field testing are presented and discussed in this section. Head displacement of piles are measured with the wire extensometer during testing, while its deflection is measured with inclinometer probe which is placed in pile installed aluminium casing as it described in Chapter 5.

Deflection of soil-pile system can be expressed using Rayleigh-Ritz method that satisfies 3.1 which in turns gives function of pile deflection by Fourier series as:

$$y(z) = \sum_{i=1}^{n} \mathbf{B}_i \left(1 \cos \overline{N} \pi z \right) \tag{6.1}$$

where $\mathbf{B}$ are soil-pile system coefficients, $\overline{N} = \frac{2i-1}{2L}$ and z is the depth.

Coefficients $\mathbf{B}$ can be obtained using the procedure defined in Appendix A, with equations (A.16) and (A.17). Differentiating the equation (6.1) with respect to the depth z, function of rotation $\theta(z)$ (equation (6.2)), bending moment $M(z)$,(equation (6.3)), shear force $V(z)$, (equation (6.4)), and soil reaction $p(z)$, (equation (6.5)), can be obtained.

$$\theta(z) = \frac{dy(z)}{dz} \tag{6.2}$$

$$M(z) = EI\frac{d^2y(z)}{dz^2} \tag{6.3}$$

$$V(z) = \frac{dM}{dz} \tag{6.4}$$

$$p(z) = \frac{dV}{dz} \tag{6.5}$$

Since Fourier series function can cause ill-posed condition after differentiation, the Cesáro sum technique can be used to overcome that issue [86].

The Cesáro summation technique is a mathematical method that is assigning a sum to an infinite series. If a series of data converges to $\sum A$, then it is also sumable using the Cesáro sum technique, and has the Cesáro $\sum A$. The biggest advantage of this technique is that a series that does not converge may still be well defined using Cesáro sum-technique [87].

Using the defined Cesáro sum's from equations (A.7) to (A.11) and applying them to the equations (6.2), (6.3), (6.4) and (6.5), where partial sum is defined as $a_n = \mathbf{B}_n \left(1 - \cos\overline{N}\pi z\right)$, the equations can be expressed with the Cesáro sum coefficients (C, k) as defined in Appendix A with equations (A.22), (A.23), (A.24), (A.25) and (A.26) for displacements, rotations, bending moments, shear forces and soil reactions, respectively.

6.1 Monotonically loaded single pile

Single pile was laterally loaded with a monotonic increment of pile head displacement. Defined displacement was 2 mm for each loading step. There was no unloading and reloading procedure. The pile was loaded until the force was brought to the ultimate load force for the soil-pile system. Load displacement curve for this test is plotted in the Figure 6.1.
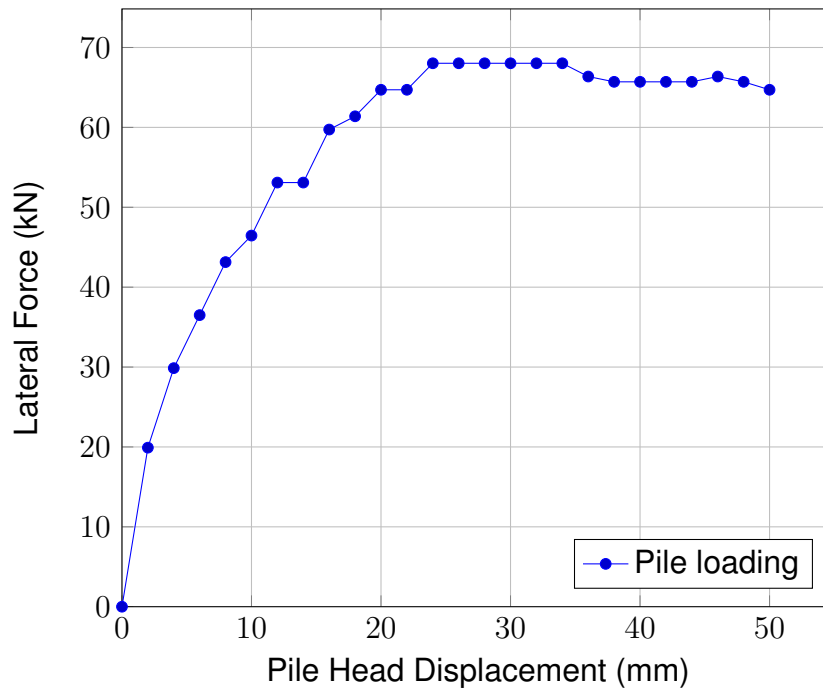
FIGURE 6.1: Pile head displacement vs lateral force for monotonically loaded single pile with monotonic loaded

6.1.1 Displacements and deflection

Displacements of a laterally loaded single pile with monotonic load are presented on Figure 6.2. Figure 6.2 a) presents pile deflection for a small pile head displacements, while Figure 6.2 b) shows deflection of a single laterally loaded pile for large pile head displacements.

If the Cesáro sum is applied as it described in Appendix A, for $(C, 1)$ (equation (A.22)), approximation of measured data for monotonically loaded single pile can be defined. These approximations are presented in Figure 6.3.

6.1.2 Bending curves

Bending curves are calculated from pile deflection using the Cesáro sum technique. The approximation of bending moment is based on the equation (A.24), see Appendix A. Figure 6.4 presents bending curves for monotonically loaded single pile.
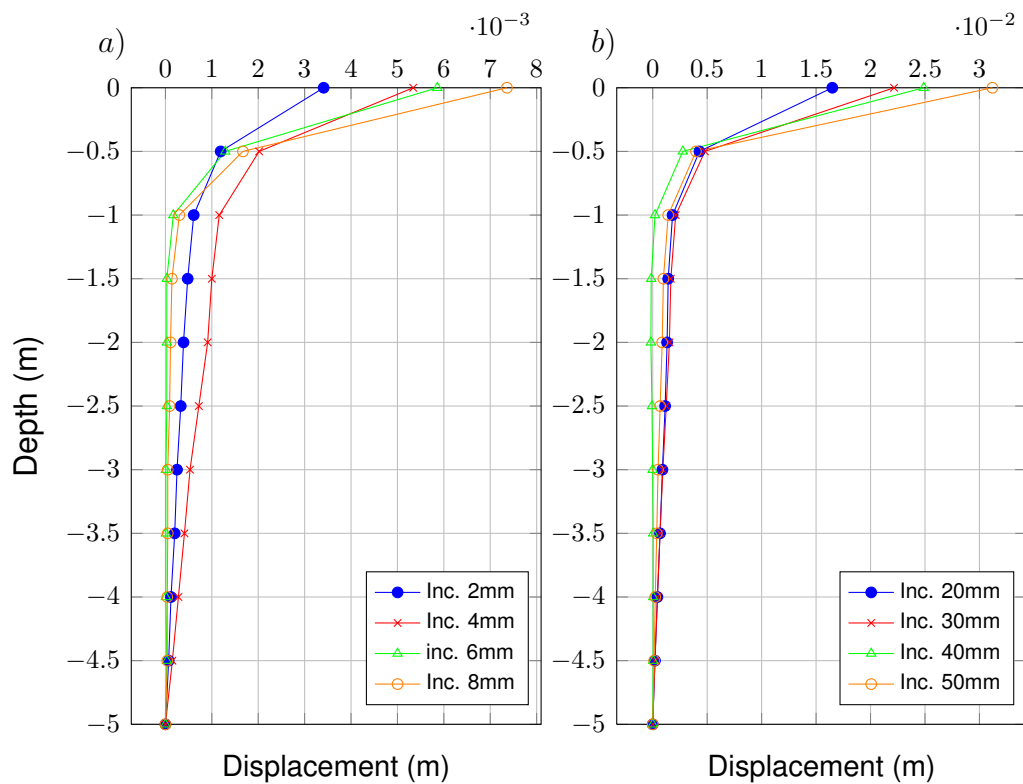
FIGURE 6.2: Deflection of a monotonically loaded single pile: a) Small head
displacements and b) Large head displacements

6.1.3 Soil resistance

To determine approximate soil resistance of a monotonically loaded single pile,
the Cesáro sum based on the equation (A.26) is used. Using equation (A.26)
p-y curves for monotonically loaded single pile are calculated and plotted on
Figure 6.5. Plotted curves are defined for depths of 0.5m, 1m and 1.5m.

FIGURE 6.3: Approximation of deflections of a monotonically loaded single pile using Cesáro sum technique: a) Small head displacements and b) Large head displacements
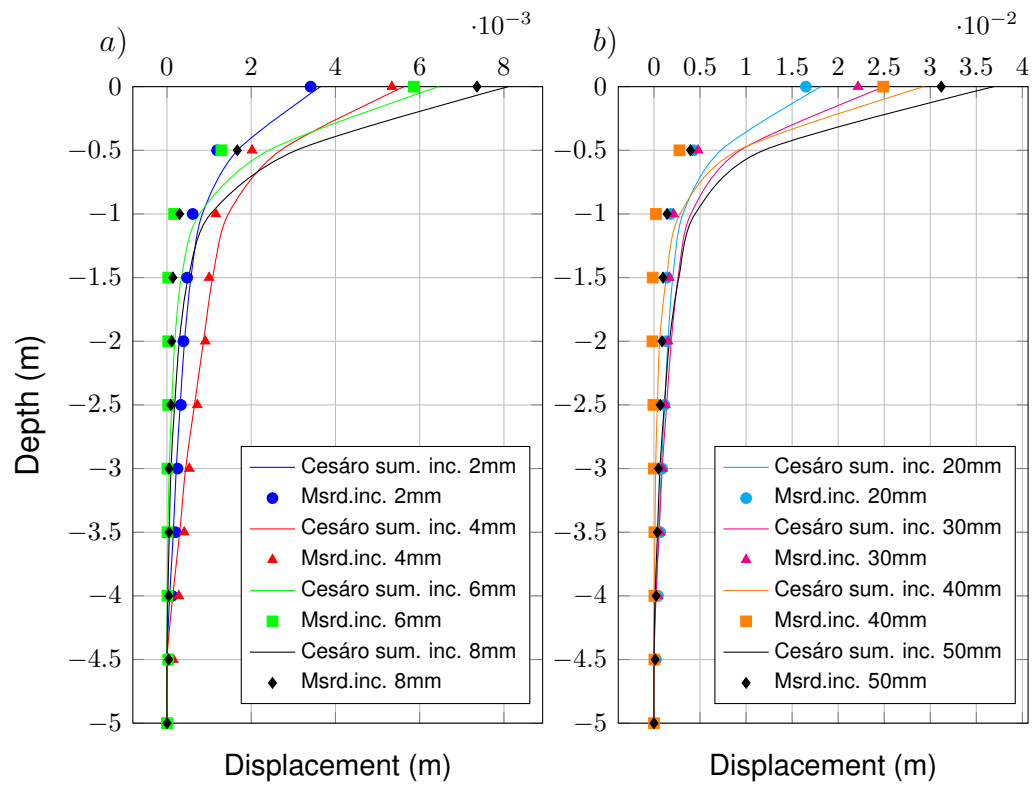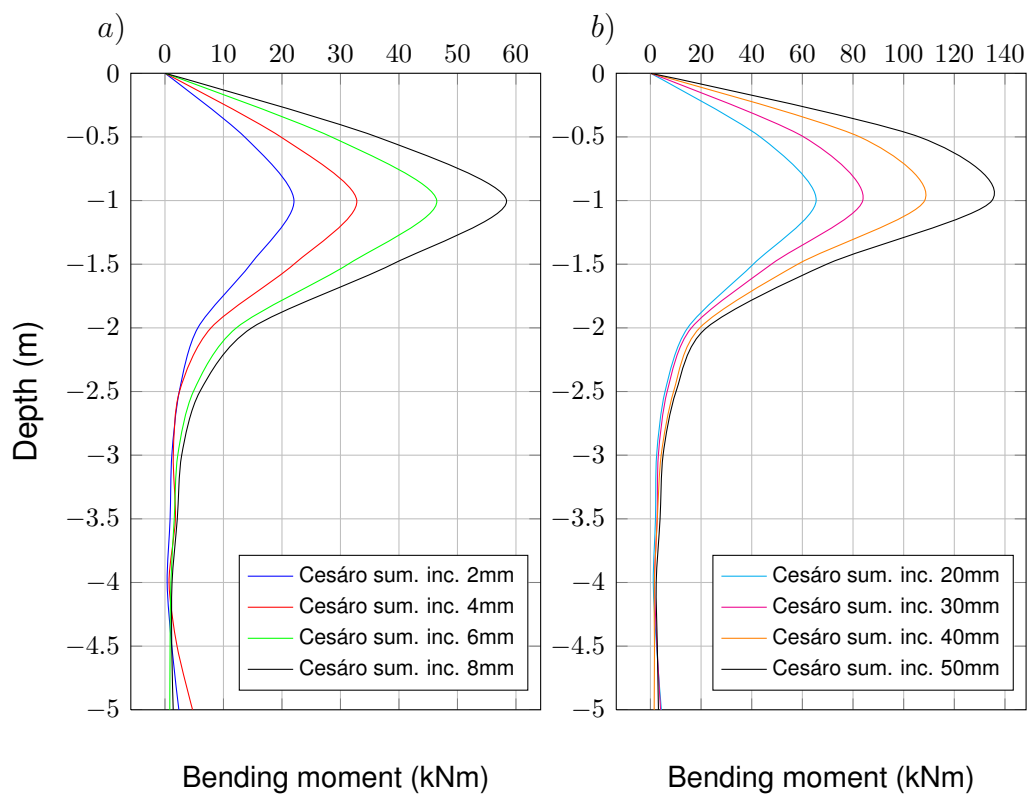
FIGURE 6.4: Approximation of bending curves of a monotonically loaded single pile using Cesáro sum technique: a) Small head displacements and b) Large head displacements
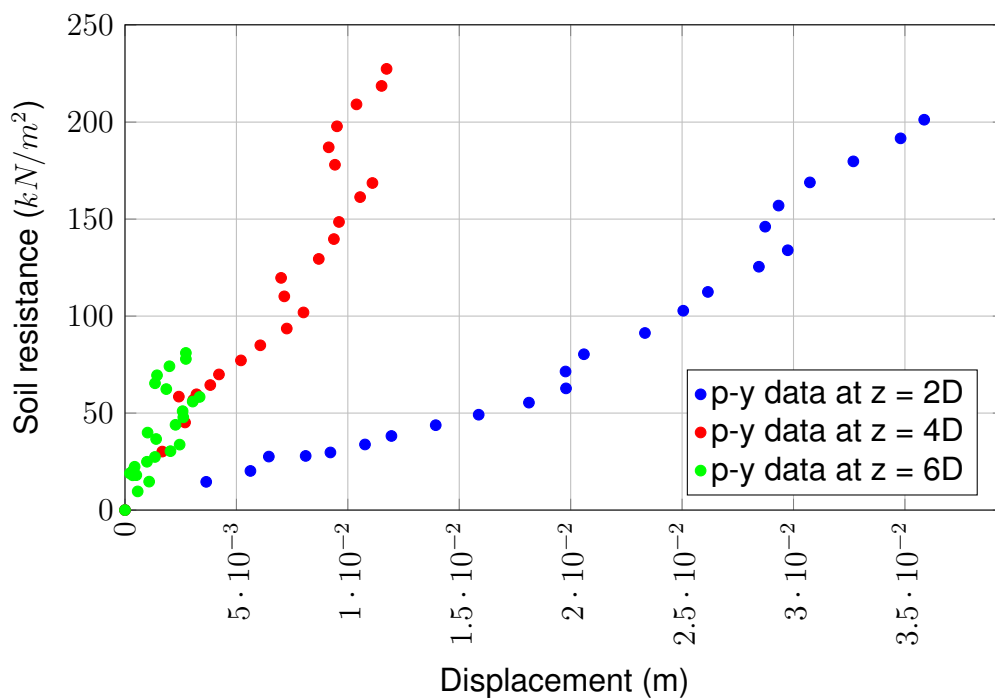

FIGURE 6.5: Data points of *p-y* curves of a monotonically loaded single pile

6.2 Cyclicly loaded single pile

Test is conducted on a single pile laterally loaded with a monotonic loading. Force increment was 2mm until pile head displacement of 24mm after which force was reduced to zero, gradually. Pile head displacements during the reduction of the force wasn't measured. The deformation of a pile after unloading was 5.2mm which gives a valuable information about plastification of soil-structure system.

Pile was then loaded again until the ultimate load of system. The load deformation curve is shown on Figure 6.6. It is worth mentioning, that after unloading of as pile, the left over deformation was 15.2mm.
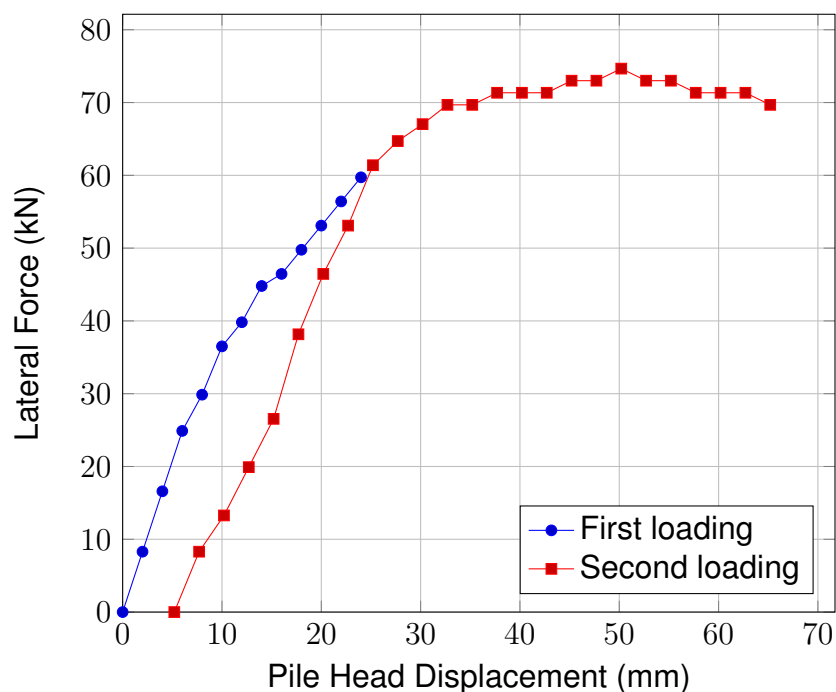
FIGURE 6.6: Pile head displacement vs lateral force for single pile cyclicly loaded (2 cycles)

6.2.1 Displacements and deflection

Using the inclinometer probe, as it mentioned in Chapter 5, deflections of a loaded pile were measured. On Figure 6.7, the deflection of a single pile under cyclic loading is presented, derived from inclinometer probe. Applying the Cesáro sum technique as it defined in Appendix A, for $(C, 1)$ (equation (A.22)),

approximation of measured data can be defined, and they are presented on Figure 6.8.
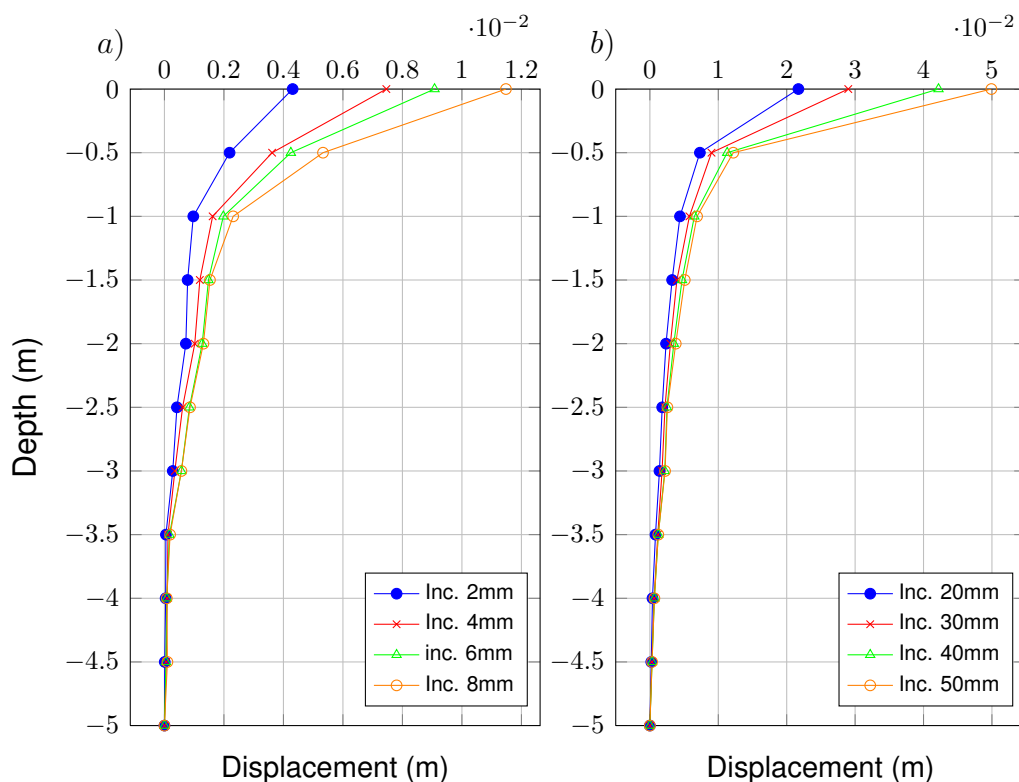
FIGURE 6.7: Deflection of a cyclicly loaded single pile: a) Small head displacements and b) Large head displacements

6.2.2   Bending curves

Bending curves are determinated using the Cesáro sum technique based on the equation (A.24). On Figure 6.9, bending curves are presented for cyclicly loaded single pile.

6.2.3   Soil resistance

Using the Cesáro sum technique based on the equation (A.26), *p-y* curves for cyclicly loaded single pile are plotted and presented on Figure 6.10. Plotted curves are for pile depths of 0.5 m, 1 m and 1.5 m.

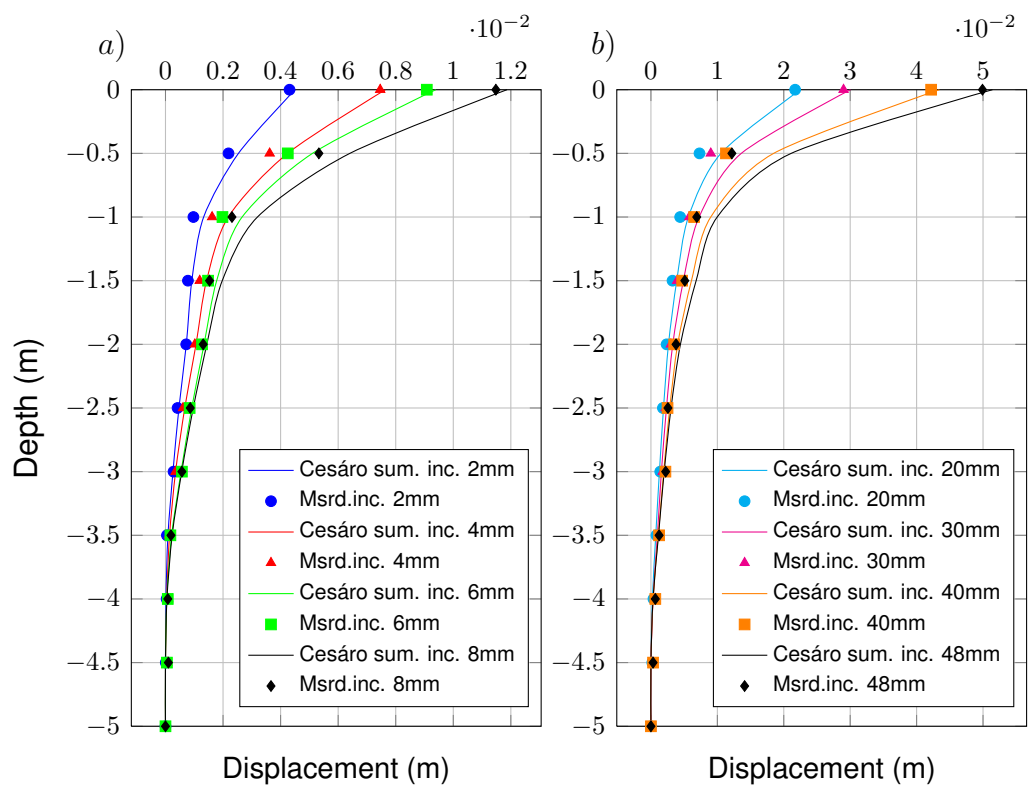FIGURE 6.8: Approximation of deflection of a single pile using Cesáro sum technique: a) Small head displacements and b) Large head displacements
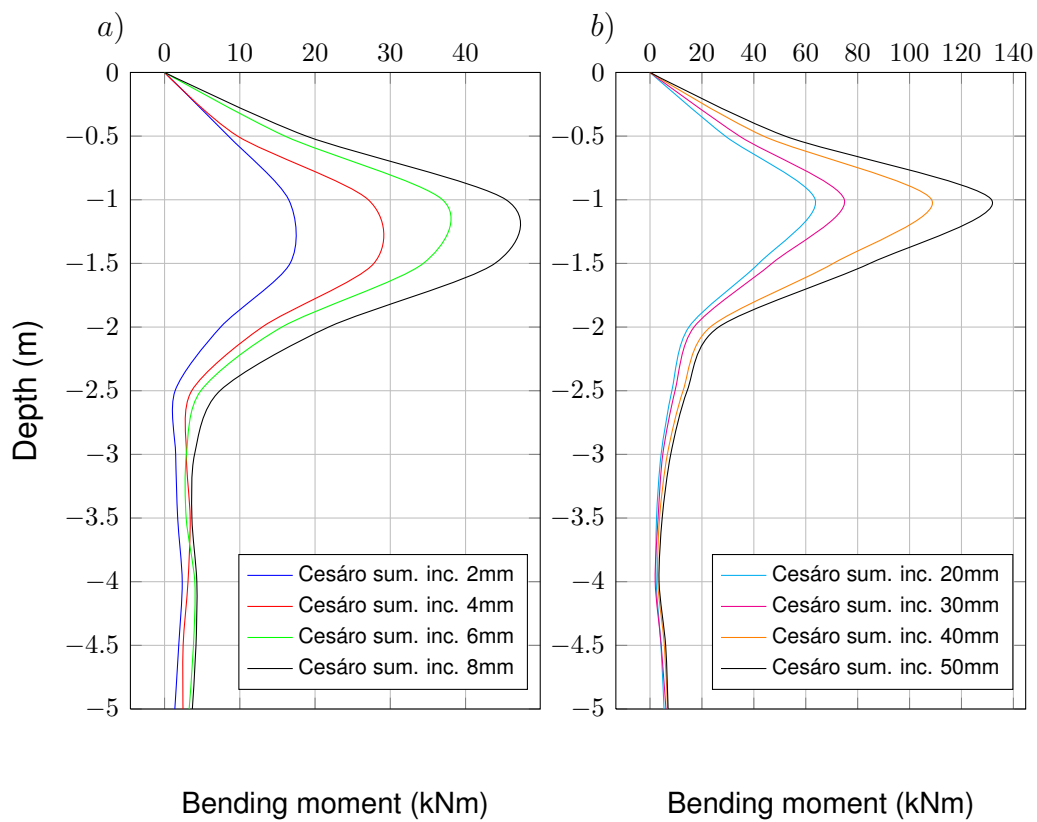
FIGURE 6.9: Approximation of bending curves of a single pile using Cesáro sum technique: a) Small head displacements and b) Large head displacements
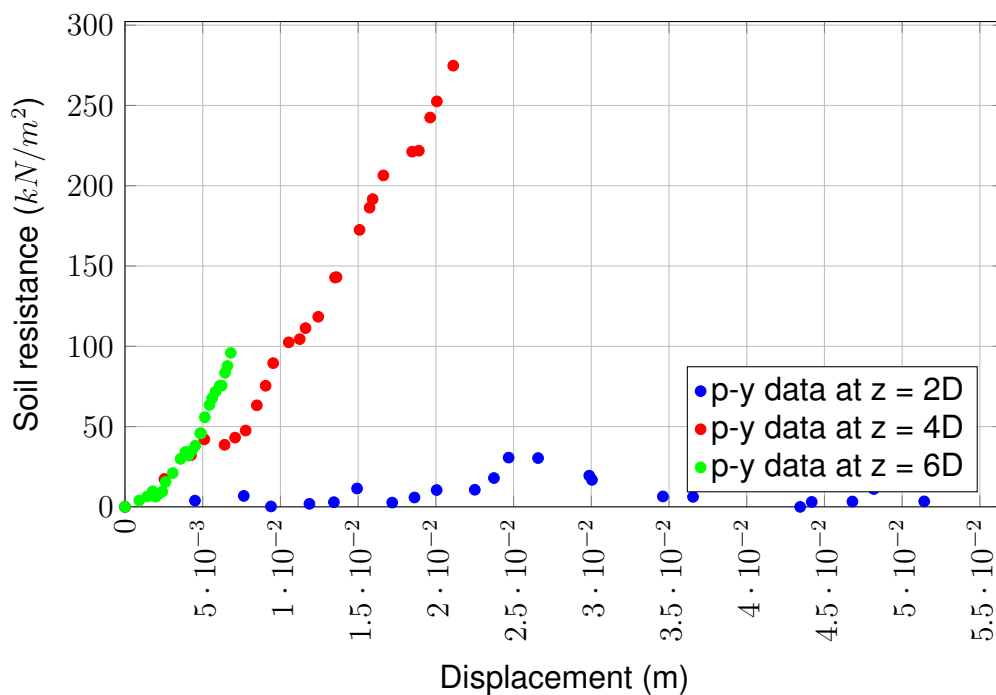
FIGURE 6.10: Data points of *p-y* curves of a pile with Cesáro sum

6.3 Monotonically loaded two piles in line

A group of two piles in line are tested using monotonic loading. Piles were connected with special joint connections, which enable possibility of pile head rotation. Displacement increment was 2 mm. Displacement was incremented until force on a press stood still, which corresponded to a lateral displacement of 50 mm. The ultimate load was divided by the number of piles. Lateral displacements versus average loads per pile are plotted on Figure 6.11. Group of piles was then unloaded until force was equal to zero. Displacement of a group of piles after unloading was 23 mm.

FIGURE 6.11: Pile head displacement vs lateral force for two piles in line

6.3.1 Displacements and deflection

As it stated before, pile deflection was measured using inclinometer probe. On Figure 6.12, deflection of Pile 3 (Figure 6.12 a)) and Pile 4 (Figure 6.12 b)) are plotted. If Cesáro sum technique (Appendix A, equation equation (A.22)) is applied to a measured data, then the displacement approximation can be derived. Approximation of displacements of Pile 3 are plotted on Figure 6.13 a) while displacements of Pile 4 are plotted on Figure 6.13 b)
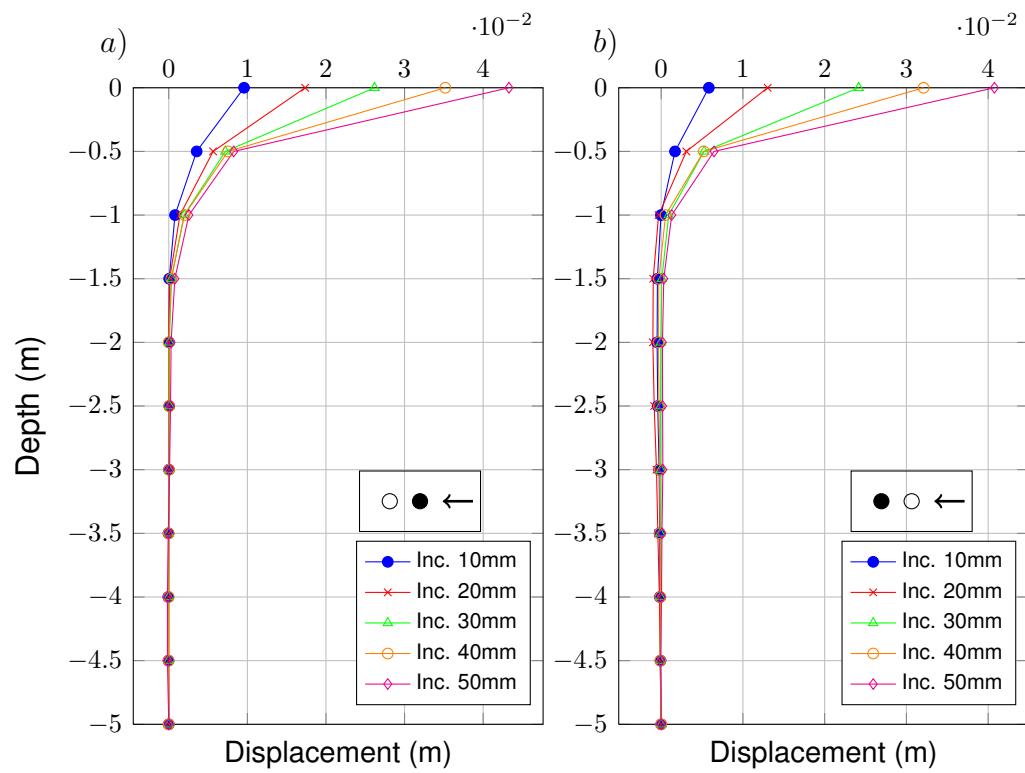
FIGURE 6.12: Deflection of a monotonically loaded *2 by 1* pile group: a) Deflection of Pile 3 and b) Deflection of Pile 4
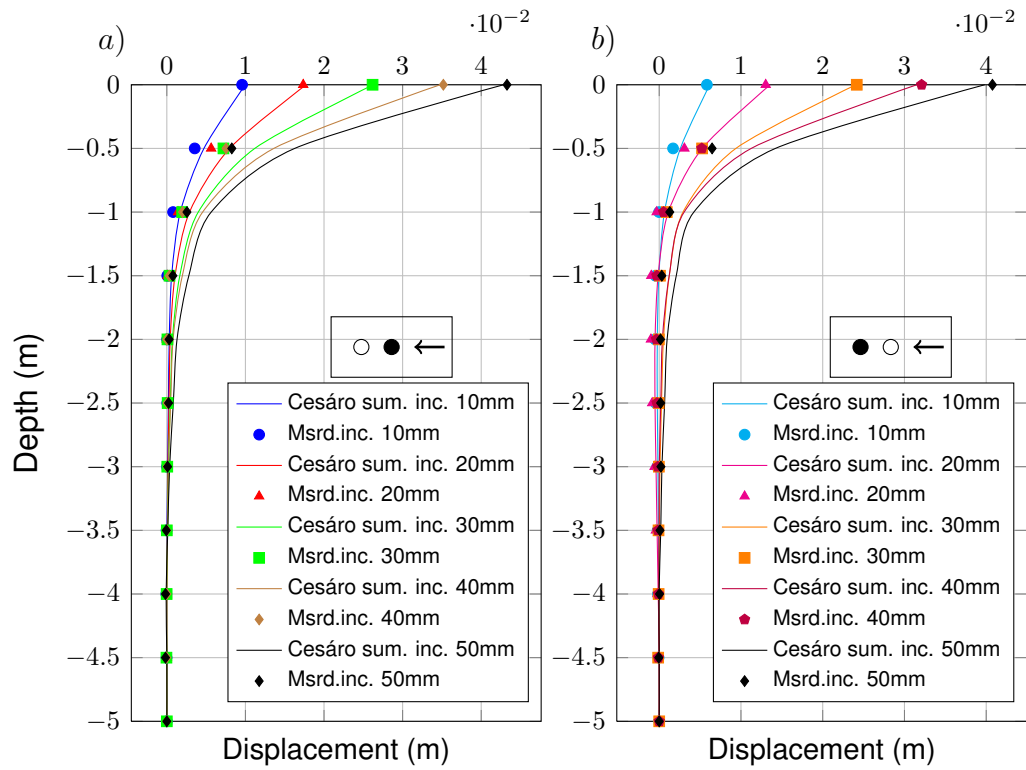
FIGURE 6.13: Approximation of deflections of a Pile 3 with Cesáro sum: a) Deflection of the Pile 3 and b) Deflection of the Pile 4

6.3.2 Bending curves

Bending curves are defined, as before, using the Cesáro sum based on the equation (A.24). Figure 6.14 a) shows bending curves of a Pile 3, while on Figure 6.14 b) are presented bending curves for Pile 4.
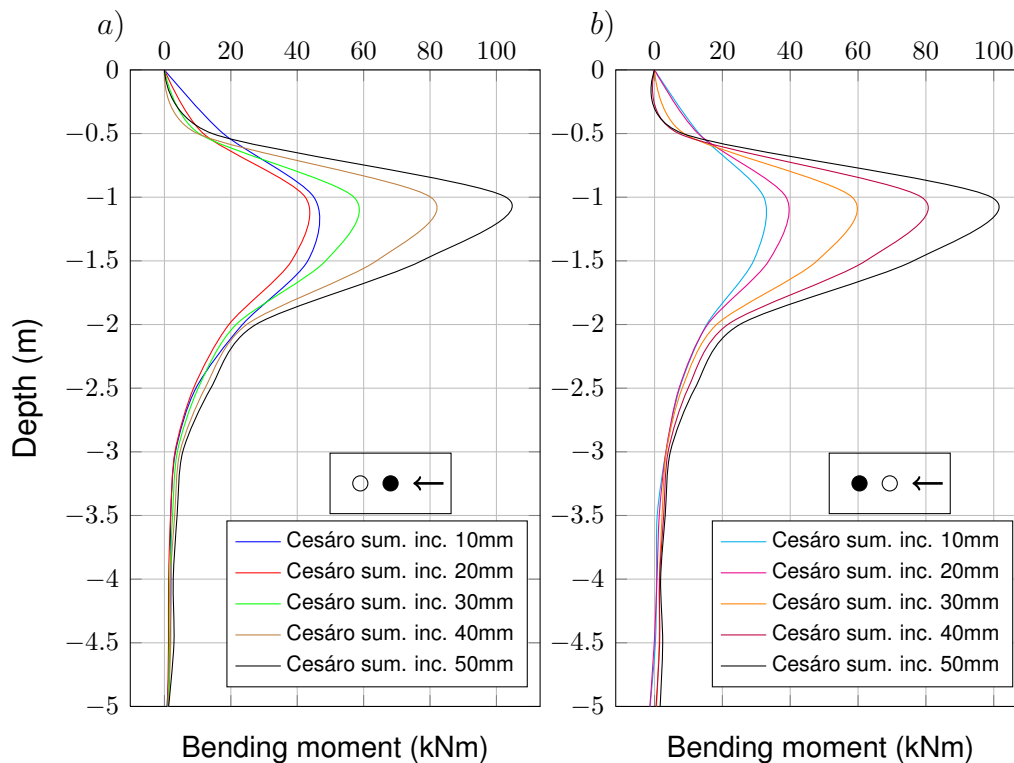
FIGURE 6.14: Approximation of bending curves: a) Bending curves of the Pile 3 and b) Bending curves of the Pile 4

6.3.3 Soil resistance

For determination of soil resistance, the equation (A.26) of Cesáro sum technique is used. The *p-y* curves for Piles 3 and 4 are plotted on Figures 6.15 and 6.16, respectively.
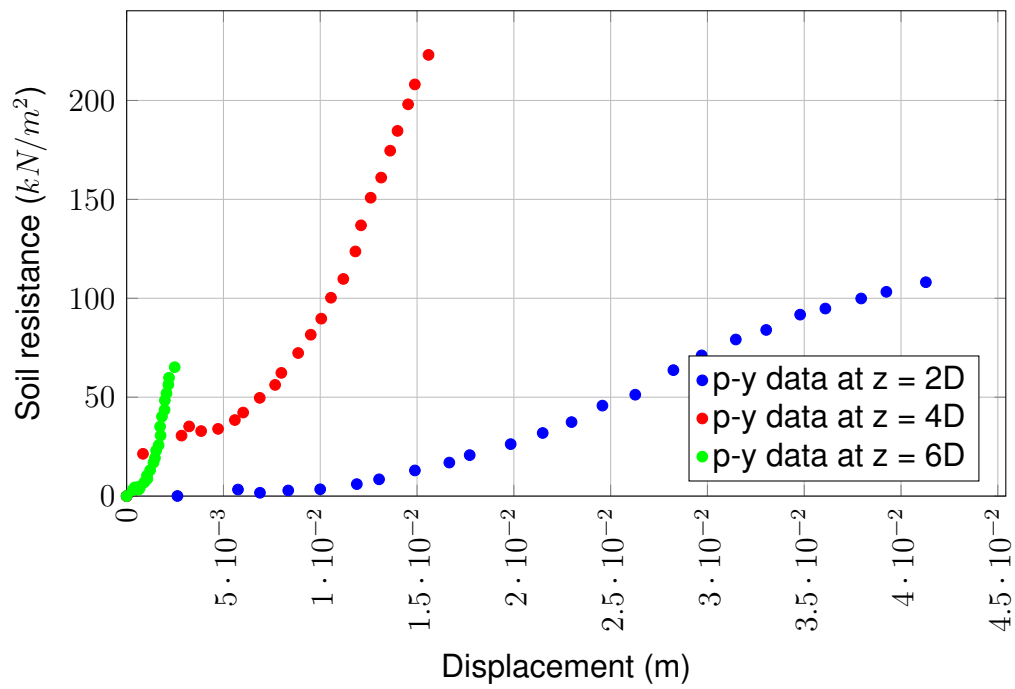
FIGURE 6.15: Data points of *p-y* curves of a Pile 3
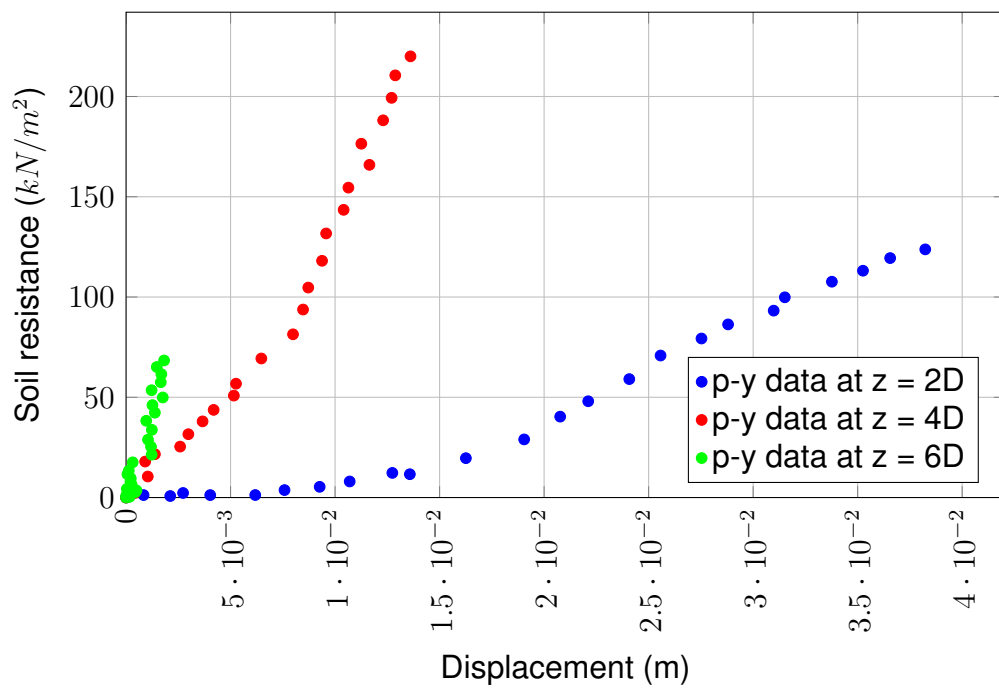
FIGURE 6.16: Data points of *p-y* curves of a Pile 4

6.4 Monotonically loaded group of 2 *by* 3 piles

Group of six piles (2 rows and 3 columns in load direction; Figure 5.1) are tested with applying monotonic load. Piles were connected to loading frame with special type of joint connections allowing the pile heads to rotate freely. Displacement increments of loading were small, and varied from 0.5 - 1.0 mm per step. Testing was discontinued due to overload of steel structure. Probably this is the main reason why there is a non-linear shape of load displacement curve presented on Figure 6.17. In the following subsection (Figure 6.18) it can be observed that the piles have not experienced significant displacements that would produce breaking of piles.
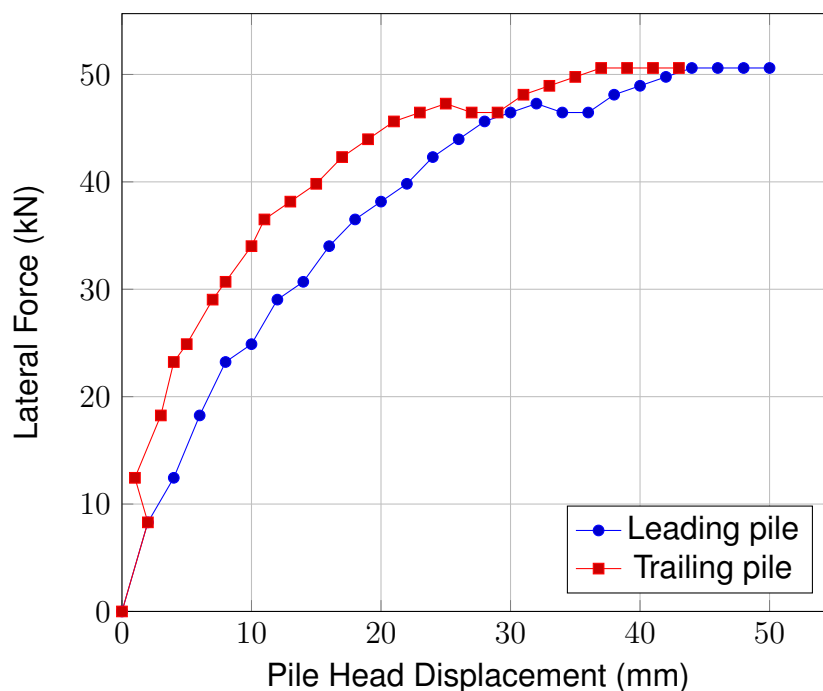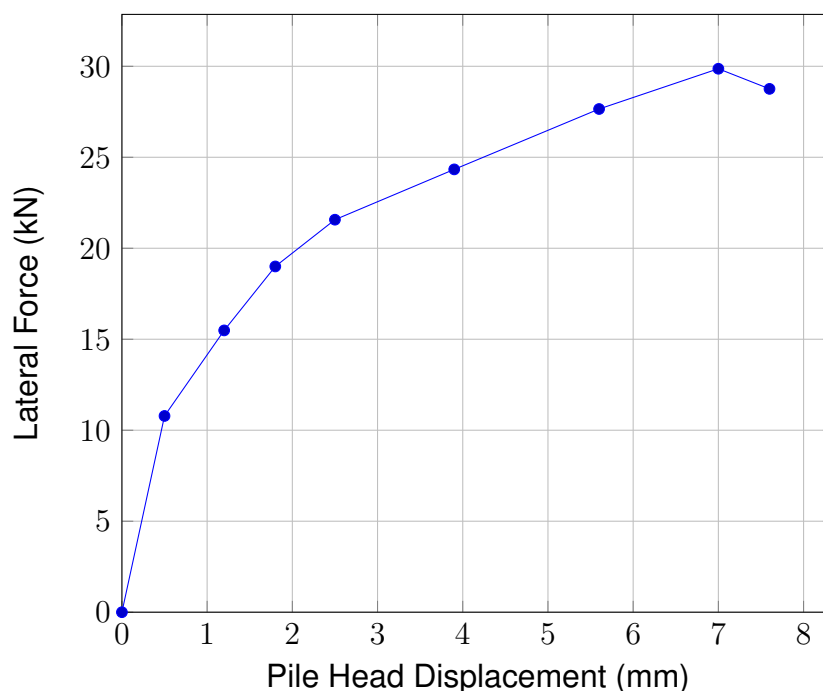
FIGURE 6.17: Pile head displacement vs lateral force for the group of 6 piles

6.4.1 Displacements and deflection

As it is stated before, piles deflections were measured using the inclinometer probe. In Figure 6.18, deflections of a Pile 5 (6.18 a)), Pile 6 (6.18 b)), Pile 7 (6.18 c)) and Pile 8 (6.18 d)) are presented. If Cesáro sum technique (Appendix A, equation equation (A.22))is applied to measured data, then the displacement

approximation can be plotted. Approximation of displacements of Piles 5, 6, 7 and 8 are presented on Figures 6.19 a), 6.19 b), 6.19 c) and 6.19 d) respectively.

6.4.2 Bending curves

Bending curves are defined, as before, using the Cesáro sum technique based on the equation (A.24). Bending curves of Piles 5, 6, 7 and 8 are presented on Figures 6.20 a), 6.20 b), 6.20 c) and 6.20 d) respectively.

6.4.3 Soil resistance

For determination of soil resistance, equation A.26 of Cesáro sum technique is used. Using the equation, the *p-y* curves for Pile 5, 6, 7 and 8 are plotted in Figures 6.21, 6.22, 6.23 and 6.24, respectively.
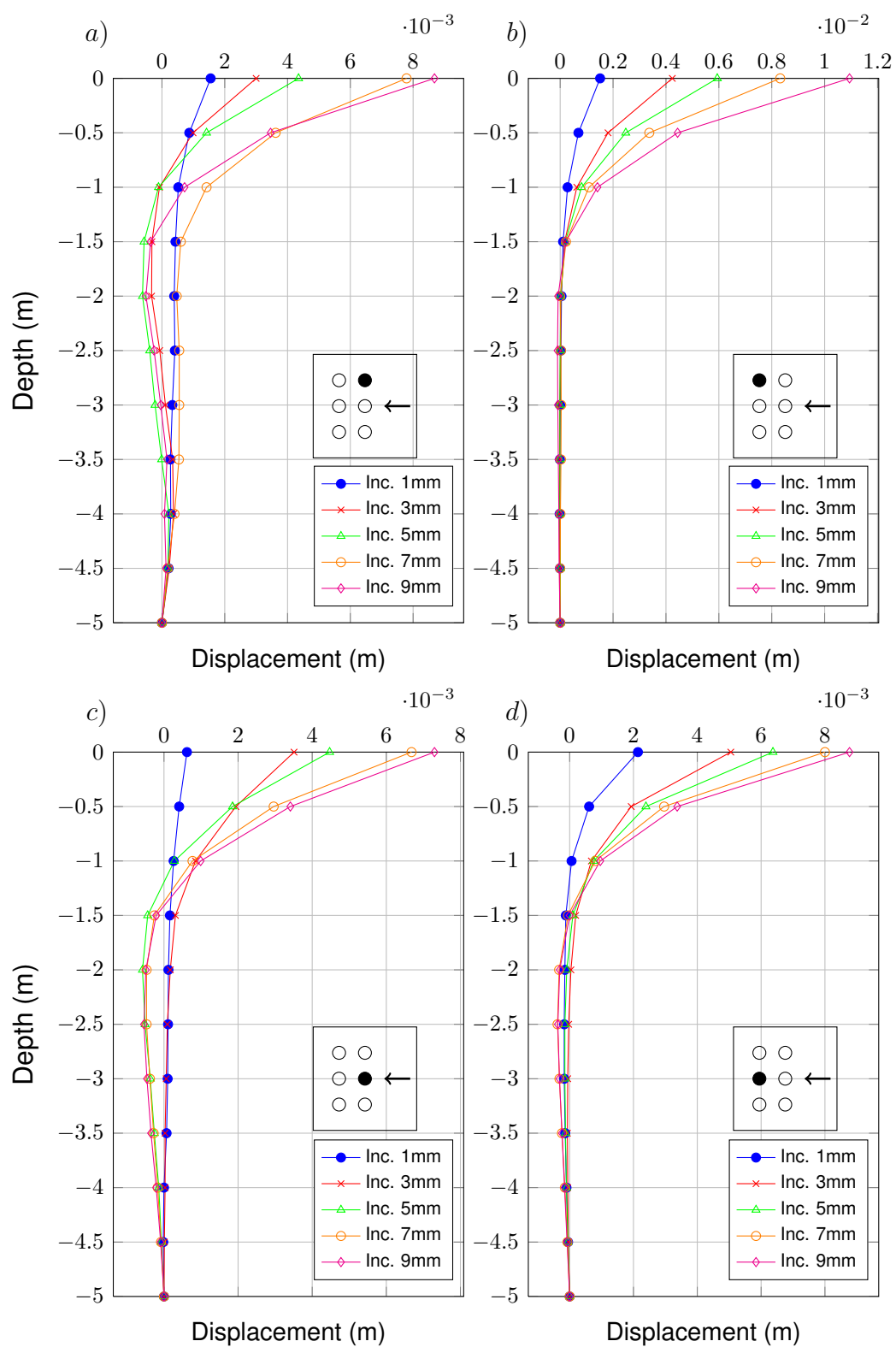
FIGURE 6.18: Deflection of a monotonically loaded *2 by 3* pile group: a) Deflection of the Pile 5, b) Deflection of the Pile 6, c) Deflection of the Pile 7 and d) Deflection of the Pile 8
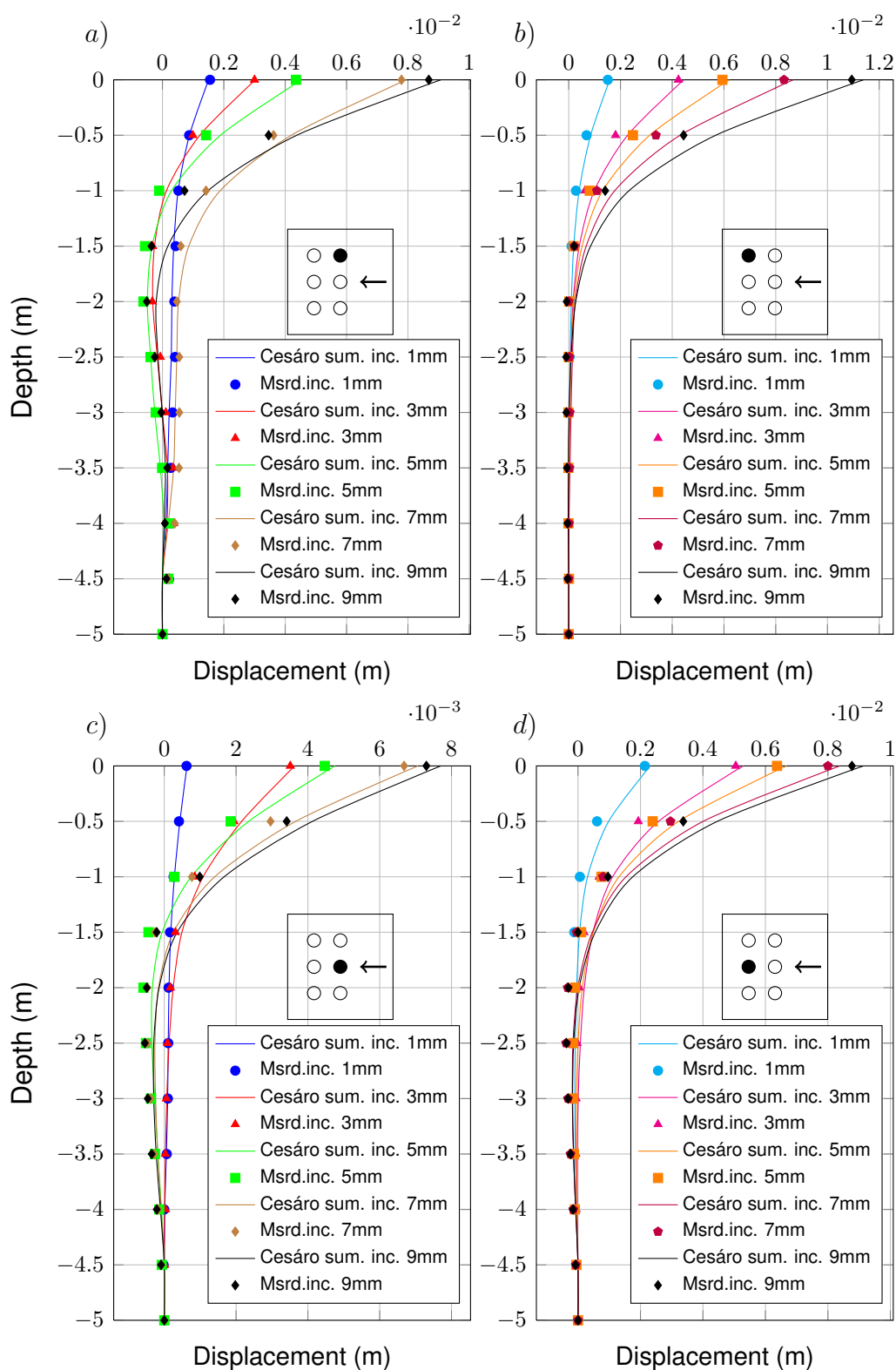
FIGURE 6.19: Approximation of deflections: a) Deflection of the Pile 5, b) Deflection of the Pile 6, c) Deflection of the Pile 7 and d) Deflection of the Pile 8
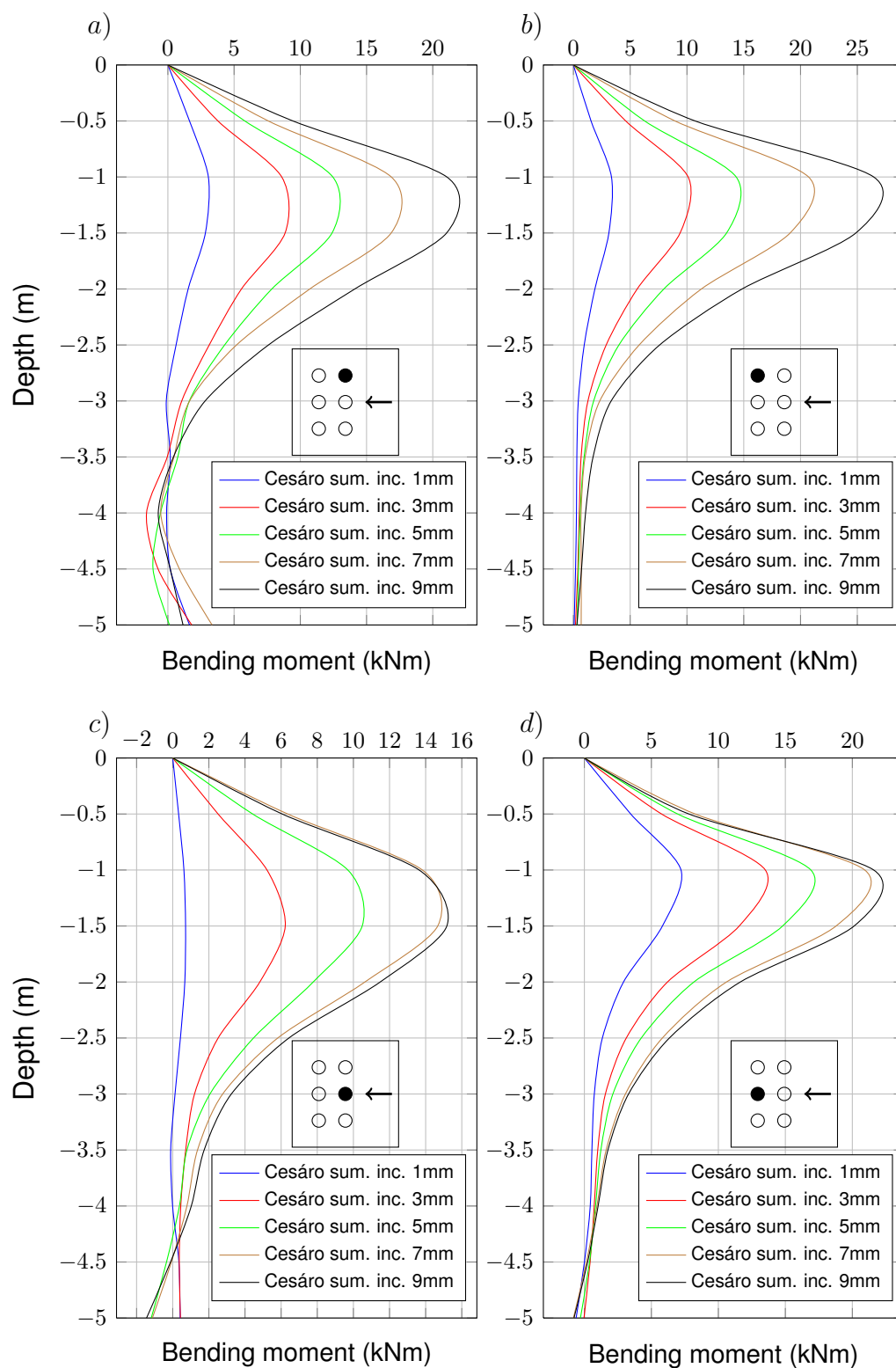
FIGURE 6.20: Approximation of bending curves: a) Bending curve of the Pile 5, b) Bending curve of the Pile 6, c) Bending curve of the Pile 7 and d) Bending curve of the Pile 8
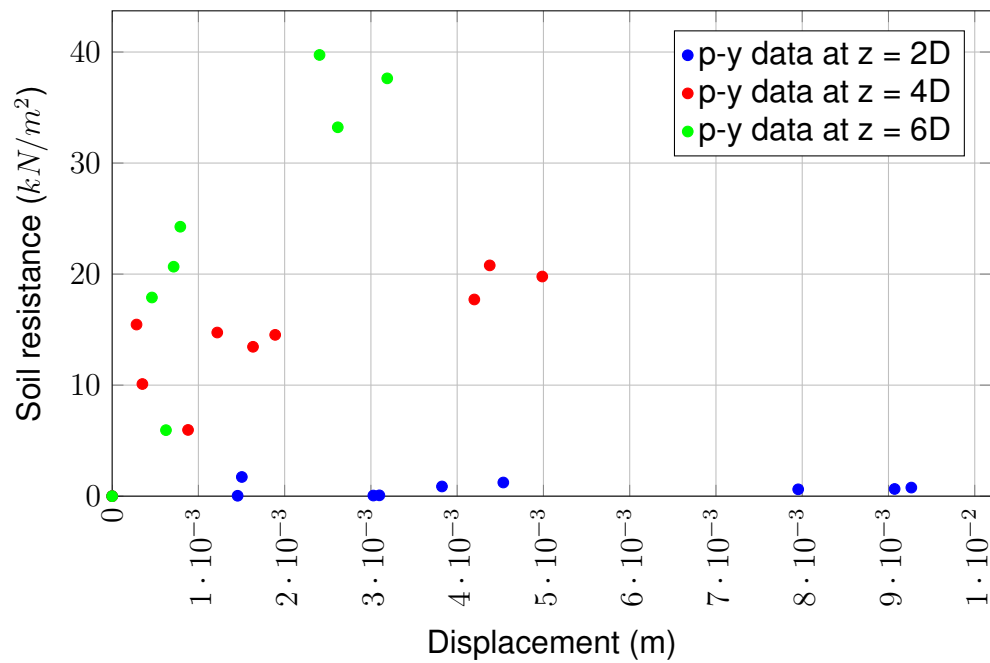
FIGURE 6.21: Data points of *p-y* curves of Pile 5
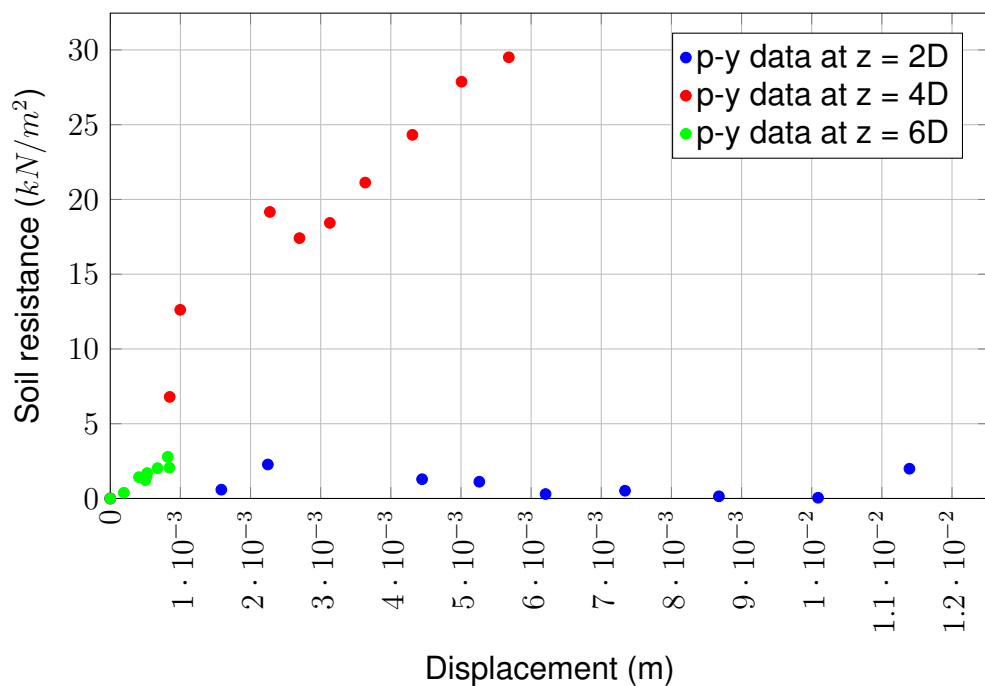
FIGURE 6.22: Data points of *p-y* curves of Pile 6
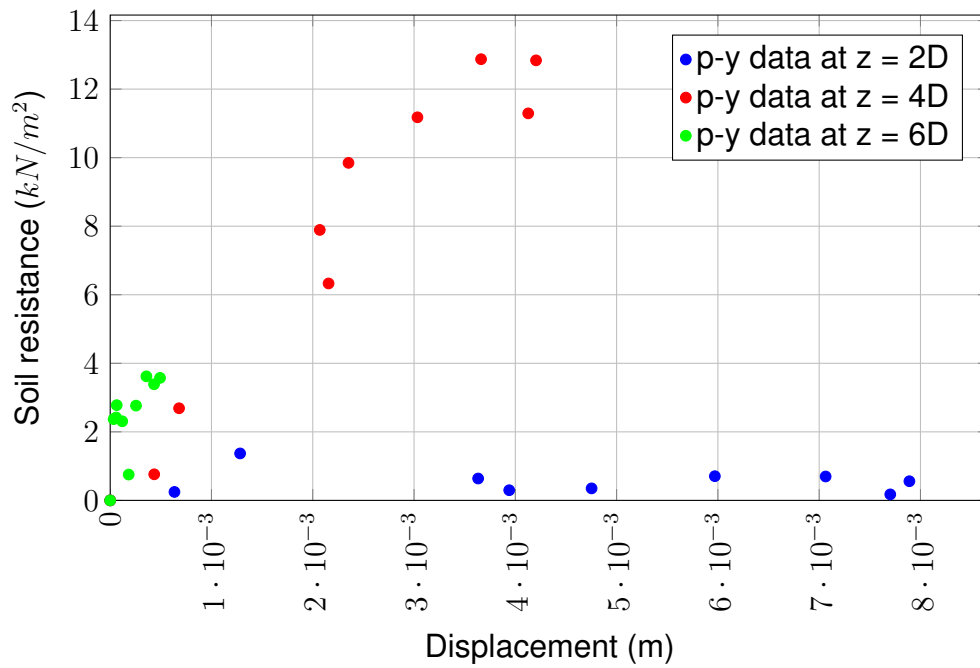
FIGURE 6.23: Data points of *p-y* curves of Pile 7
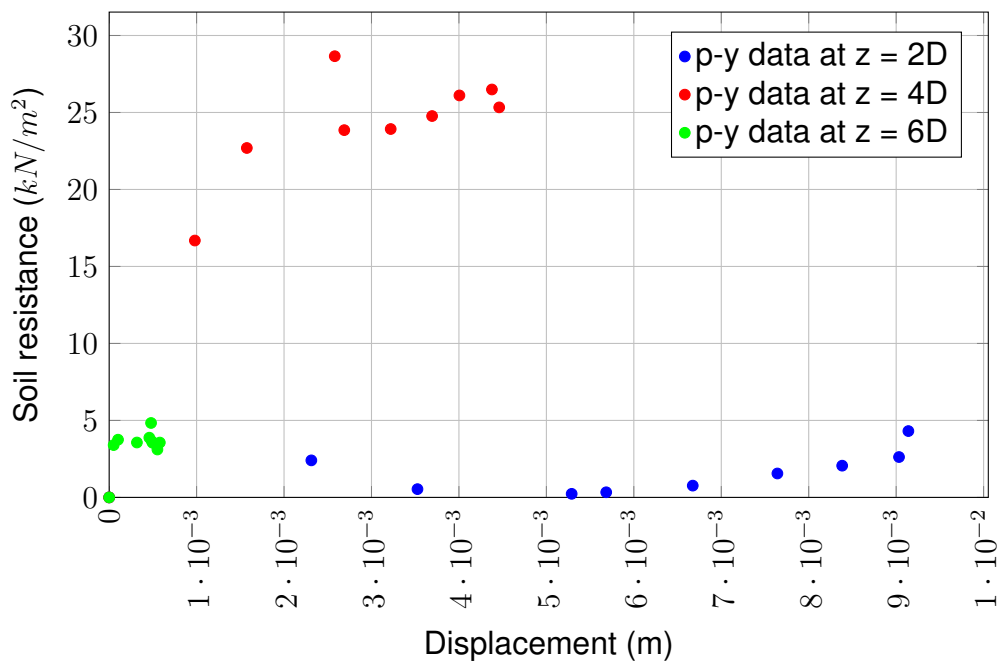
FIGURE 6.24: Data points of *p-y* curves of Pile 8

6.5   Presentation of measured results

6.5.1   Behaviour of group of piles in comparison to single pile behaviour

Within this section, the presentation of performed test results will be presented. Firstly, the ultimate force read out on the hydraulic press during the pile testing will be compared to the analytical expression of ultimate force proposed by Patra et al. [20], (2.2). In Table 6.1, the soil parameters for calculating ultimate force are given. Patra et al. [20] also gave an expression for ultimate force for the two piles in line. Ultimate force for this combination of piles loading is defined in equation (6.6).

$$Q_{Lg} = \gamma \cdot L^2 \left(K_s \cdot S + 0.36d \cdot K_p \right) \tag{6.6}$$

TABLE 6.1: Soil parameters for calculating the ultimate force based on Patra's equation [20]

			Force $[kN]$	
Unit weight $[kN/m^3]$	Friction angle $[\circ]$	E_soil $[MPa]$	Single pile	Group of two piles in one row
19	40	120	69.38	108.12

Comparing the calculated and measured results, it was concluded that expressions given by Patra et al. [20] show very good approximation of ultimate lateral force per pile with lateral forces obtained from measured results. Relations soil resistance vs. displacement for Pile 2, Pile 3 and Pile 4, plotted on Figures 6.5, 6.15 and 6.16 respectively are approximated assuming the hyperbolic type of function, given with equation (6.7), that the best fits measured results. Using the non-linear regression technique [88] and the *Mathematica* software as a tool to perform non-linear regression [89], coefficients of hyperbolic functions are determined and defined in Table 6.2.

$$f(w) = \frac{\kappa \cdot w}{\rho + \zeta \cdot w} \qquad (6.7)$$

The same procedure is used for approximation of soil resistance for Pile 5, Pile 6, Pile 7 and Pile 8 and soil resistance data is presented on Figures 6.21, 6.22,6.23 and 6.24, respectively. Values of coefficients of hyperbolic equation (6.7) are presented in Table 6.2.

On Figure 6.25 the soil resistance curves are presented. The curve referenced as a Pile 2 represents a single pile test results. Pile 3 is the pile closest to the concrete block (trailing pile), and Pile 4 is the outer (leading pile) pile of 2 by 1 group of pile. Piles are labelled on Figure 5.13. From the Figure 6.25, it can be easily depicted how the "shadowing" effect influences on the behaviour of piles in group in comparison to the single pile test results. On Figure 6.28, so called "p-multiplier" factors are presented. The "p-multiplier" factor represents the relation of ultimate soil resistance of a pile inside the group of piles referred to the ultimate soil resistance of a single pile. Using the "p-multiplier", the shape of *p-y* curves for other pile depths can be recalculated if the trend of multiplier factor is known.

TABLE 6.2: Coefficients of hyperbolic function given with equation (6.7)

Pile ID	Coefficients								
	0.5			1			1.5		
	κ	ρ	ζ	κ	ρ	ζ	κ	ρ	ζ
Pile 1	14.6	0.01509	0.53175	18.3	0.00239	0.0098	8.7	0.00068	0.00821
Pile 2	3	0.000303	0.01	3	0.0000971	0.005	3	0.0001	0.002
Pile 3	13	0.00398	0.04	39	0.009	0.08	5.2	0.00031	0.01
Pile 4	15.6	0.00373	0.03969	3	0.00013	0.00662	5	0.00013	0.00662
Pile 5	3	0.022073	0.01	3	0.0004205	0.00667	3	0.000292	0.00333
Pile 6	3	0.022873	0.01	2.5	0.0003662	0.005	2.3	0.000238	0.002
Pile 7	1	0.027987	0.02	3	0.0006588	0.00667	3	0.000361	0.00333
Pile 8	3	0.008374	0.01	3.2	0.0003119	0.005	2.8	0.000204	0.002

FIGURE 6.25: Presentation of p-y curves for single pile and group of two piles
in line for 2D, 4D and 6D depths
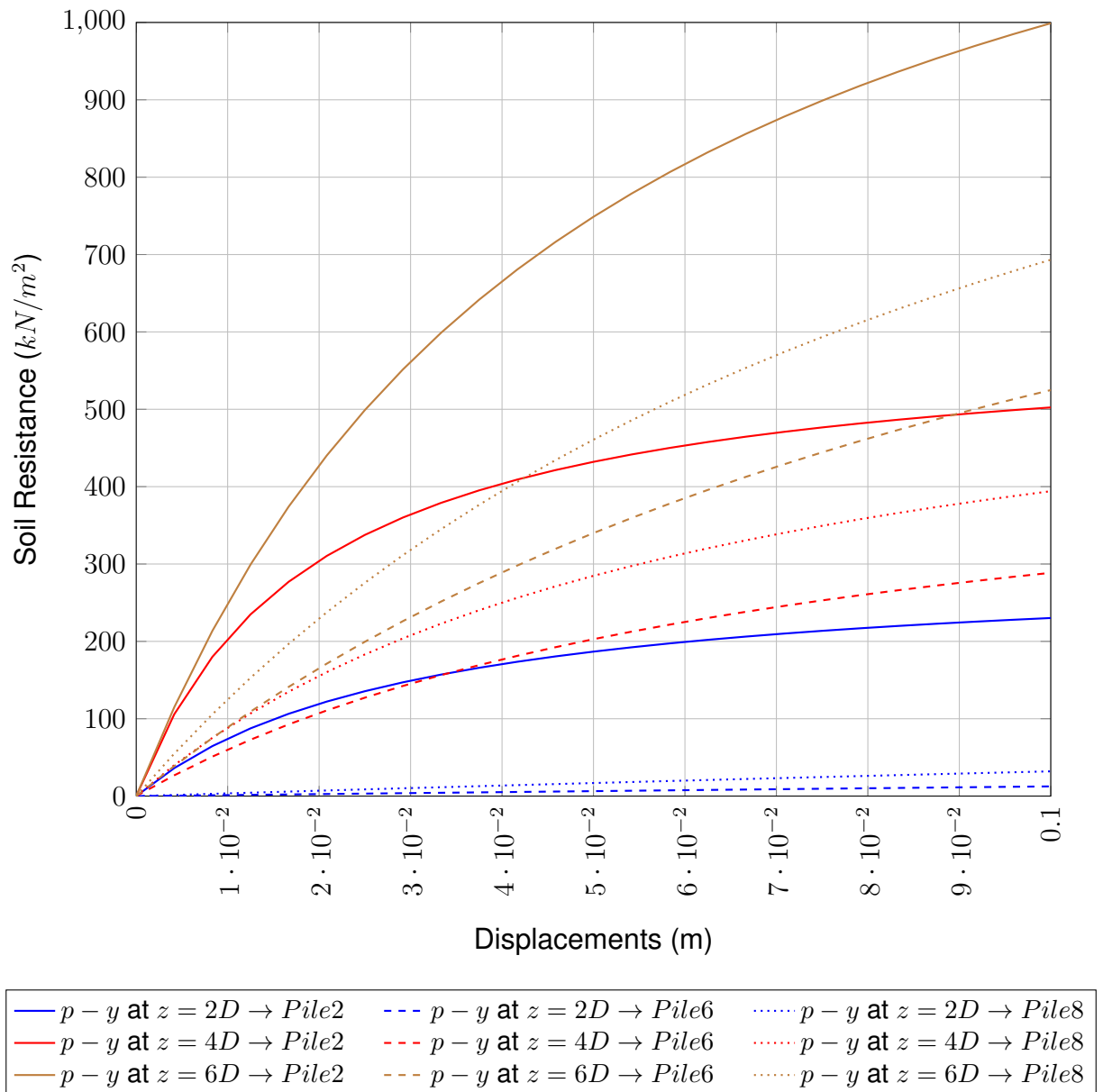
FIGURE 6.26: Presentation of *p-y* curves for single pile and group of six piles for leading row piles for 2D, 4D and 6D depths
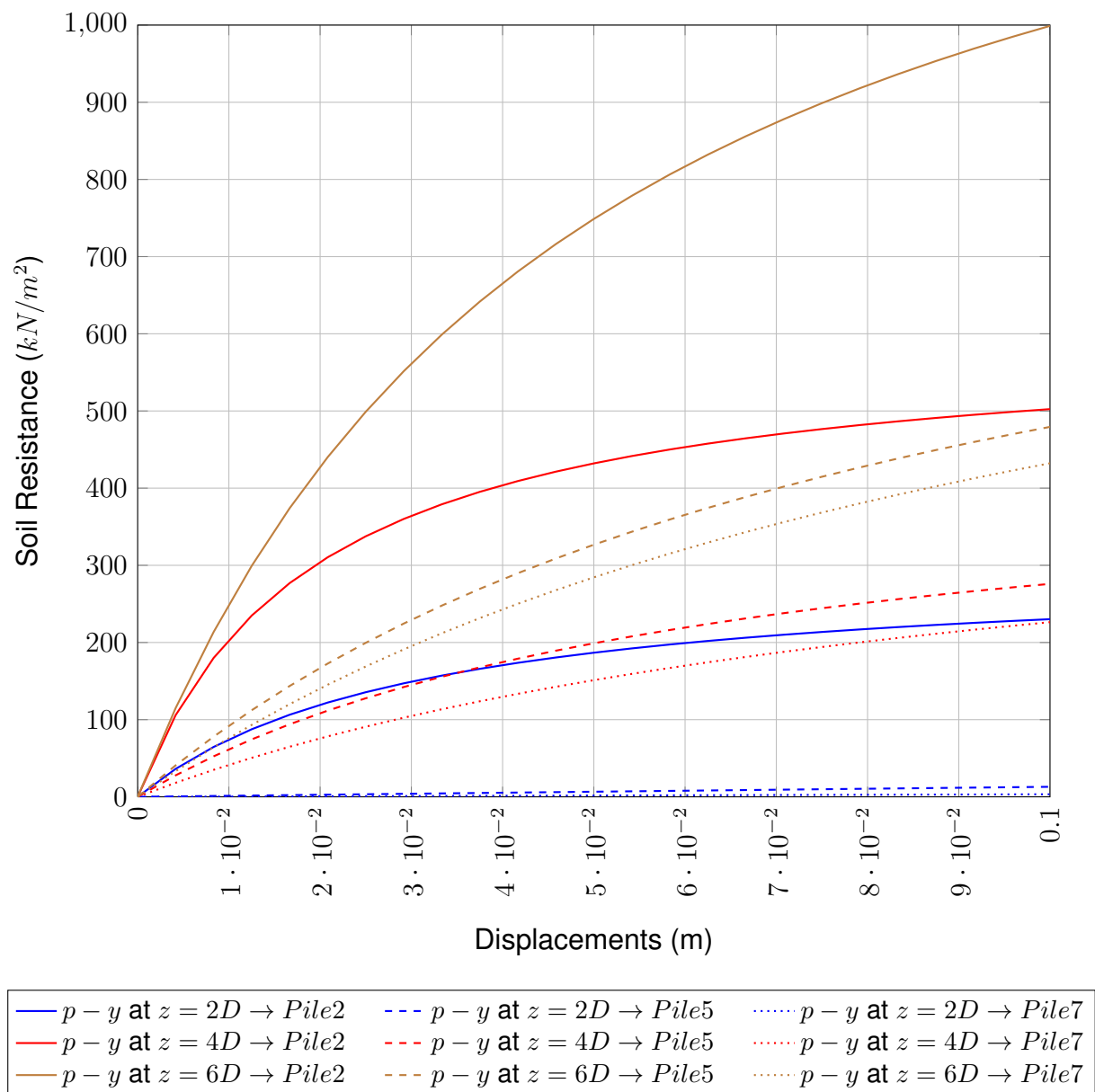
FIGURE 6.27: Presentation of *p-y* curves for single pile and group of six piles for trailing row piles for 2D, 4D and 6D depths
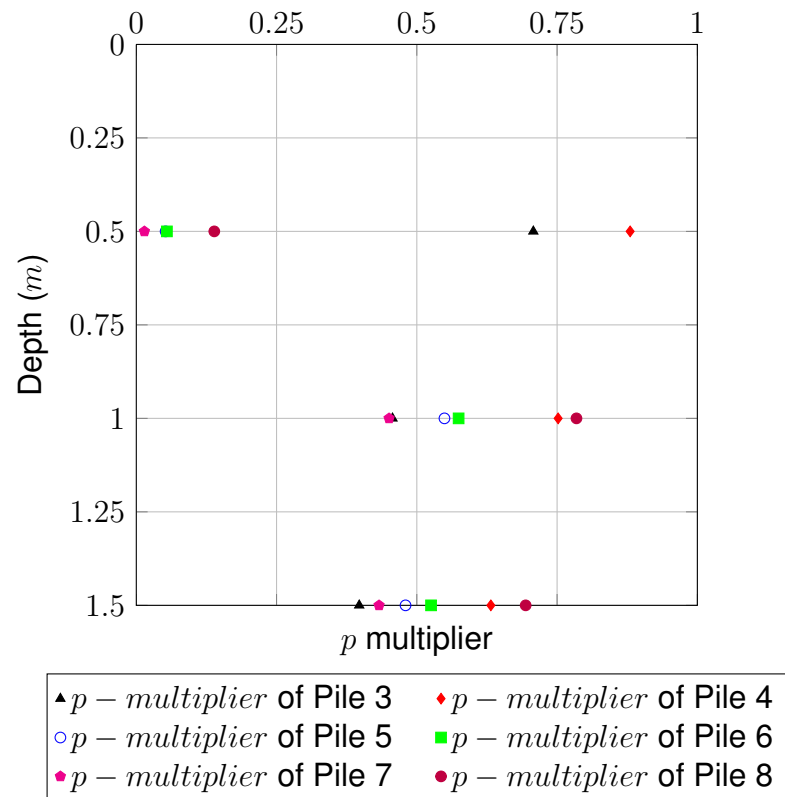
FIGURE 6.28: The "p-multipliers" for Piles 3, 4, 5, 6, 7 and 8 referred to the Pile 2

Chapter 7

Back analysis of LLP behaviour using FEM

According to Cividini et al. [90], there are two different ways to conduct back analyses: the inverse approach and the direct approach. For the inverse approach, the formulation is the reverse of that in ordinary stress analyses, even though the governing equations are identical. According to this approach, the number of measured values should be greater than the number of unknown parameters. The direct approach to back analysis is based on an iterative procedure of correcting the trial values of unknown parameters by minimizing the error function. Gioda and Maier [91] pointed out that an advantage of direct approach methods is that they may be applied to non-linear back analysis problems without having to rely on a complex mathematical background. Cividini et al. [90] stated that standard algorithms of mathematical programming might be adopted for numerical solutions. Iterative solutions require quite time-consuming computations.

Performed **LLP** testing results are analysed using **LLP** modelling. Two types of numerical analyses are performed: (i) analysis of laterally loaded pile using the four-field interpolation element discussed in Chapter 3, Subsection 3.3.3 and (ii) analysis of laterally loaded piles using three-dimensional finite element software for geotechnical analysis, RS3. In the first type of analysis, pile is modelled as a shear-rigid Timoshenko beam with two nodes (the third node is condensed out during the finite element formulation) resting on a Winkler's soil model. Two
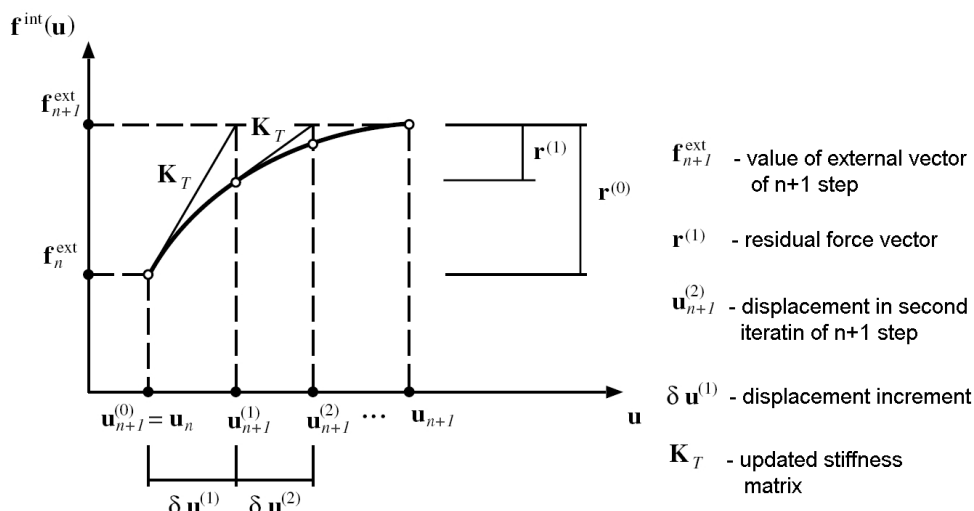
FIGURE 7.1: Sketch of absolute energy convergence process [64]

examples are presented: (i) example in which both pile and soil have linear constitutive behaviour and (ii) example in which pile has linear constitutive behaviour while soil has non-linear (hyperelastic) behavior. In the second type of analysis, pile is modelled using solid finite elements (2-dimensional elements). Elastic (Young's) modulus for solid element is calculated from the relation of stiffness of constructed pile and modelled pile [92]. The idea is to calculate the axial ($E_m A_r$) and flexural stiffness ($E_m I_m$) of a model from the real axial ($E_r A_r$) and flexural stiffness ($E_r I_r$), by equalizing them, as it proposed by Arta [92]. Soil is also modelled as a solid material. Three-dimensional finite element analysis was performed using the Rocscience's RS3 (Rock and Soil 3-dimensional modelling) computer software [93]. Piles and soil are modelled using four node tetrahedron finite elements. Automatic mesh generator was used to generate nodes and elements. Number of nodes and elements are depending on modelled problem for a single pile; and for a group of *2-by-1* piles and group of *2-by-3* piles.

Number of iterations were limited to 1000 while load steps were calculated automatically, depending on chosen absolute energy type of convergence. The absolute energy convergence process is presented on Figure 7.1, while the general behaviour is given by equation (7.1).

$$\left| \frac{\Delta U_i^T \left(P_n - F_i \right)}{\Delta U_0^T \left(P_n - F_0 \right)} \right| < e_{tol} \tag{7.1}$$

7.1 Numerical analysis using four-field finite element

The results presented here are based on the analysis of laterally loaded piles on shear-rigid Timoshenko beam resting on Winkler's soil model defined by equation (3.42). Pile is modelled using ten elements, each 0.5 m long and eleven nodes. Modulus of subgrade reaction is calculated using the function presented in section 4.5. Different values of the modulus of subgrade reaction are used for depths of 0 to 1 m and for 1 to 5 m. Forces used in calculations are taken from **LLP** field test performed on a single pile. Three load increments are compared, although the measured data indicate that the soil and the pile are behaving nonlinearly even for small lateral increments. Results of performed analysis are presented the Figure 7.2.

Presented four-field interpolation of a beam-soil element is compared to the field test results of laterally loaded pile in sandy gravels. Using the Cesáro sum technique [57, 86, 87], the *p-y* curves are developed for various pile depth. The values of *p-y* data are in good correlation to hyperbolic curve type. In that manner, the hyperbolic type of constitutive behaviour of Winkler's soil model such as one given by equation (6.7) is chosen to describe the soil behaviour in numerical model. For the purpose of pile modelling, the pile is divided in 10 finite elements, each element having the length of 0.5m . Different hyperbolic function coefficient is assigned to an element according to the element position in modelled pile. The chosen hyperbolic function coefficients are presented in Table 7.1. On the Figure 7.3, the deflection of laterally loaded pile for lateral force of $30kN$, $46kN$, $53kN$ and $61kN$ are plotted with the approximation of the same deflection obtained from analysis using the four-field mixed finite elements.

TABLE 7.1: Hyperbolic function parameters for non-linear Winkler's soil model

Depth $[m]$	κ	ρ	ζ
0 - 0.5	3	0.000303	0.01
0.5 - 1	3	0.0000971	0.005
1.0 - 1.5	3	0.0001	0.002
1.5 - 2.0	3	0.00001	0.001
2.0 - 5.0	3	0.00001	0.0005
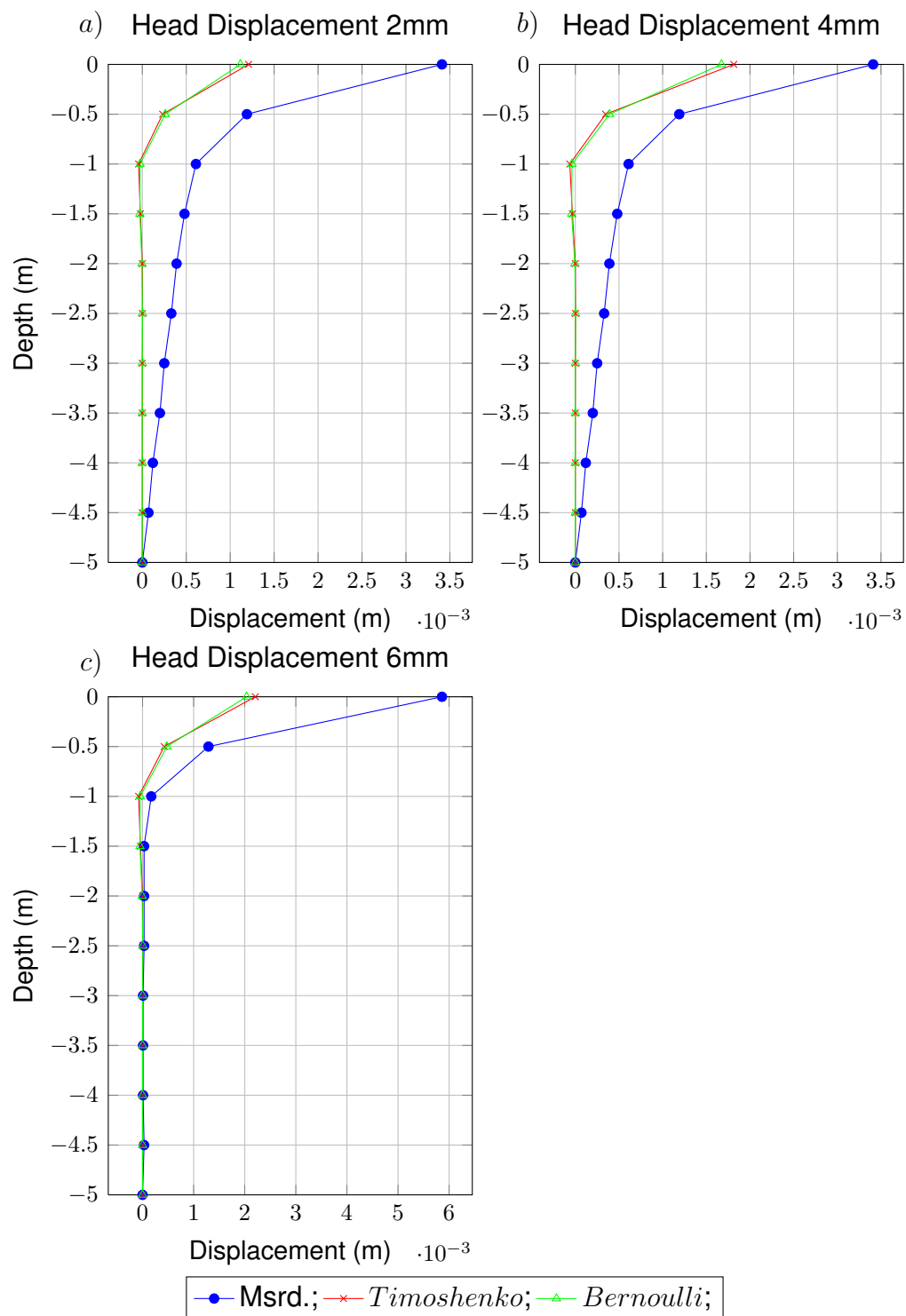
FIGURE 7.2: Measured and computed Pile 2 displacements for lateral forces: *a*) 20kN, *b*) 30kN and *c*) 36.5kN
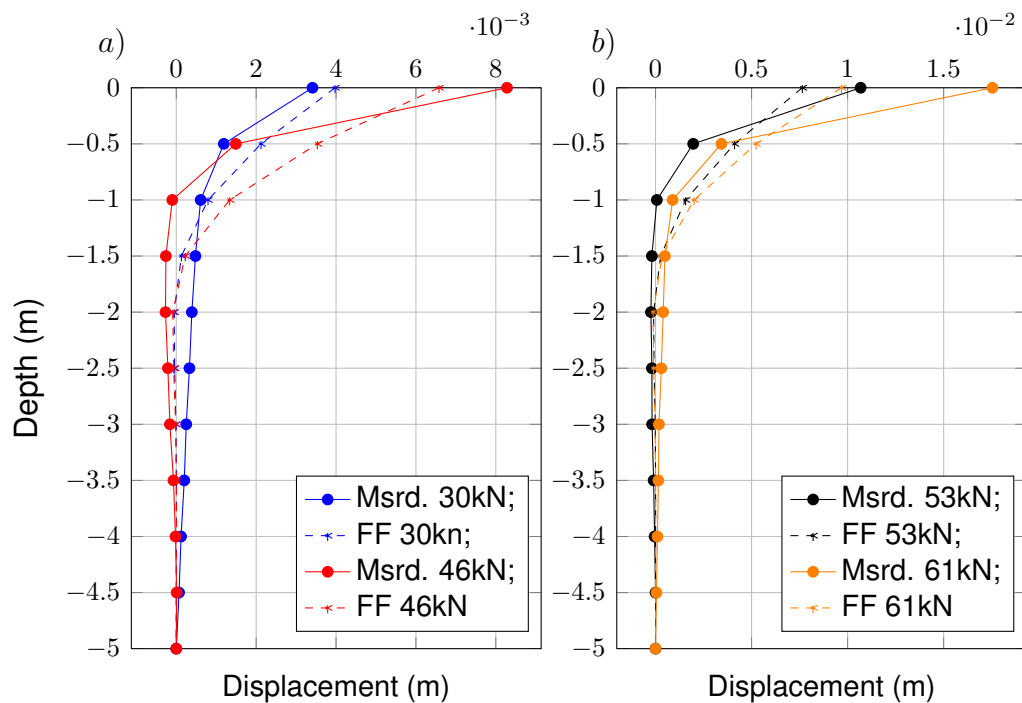
FIGURE 7.3: Measured and computed pile displacements of: $a)$ lower value lateral forces and $b)$ higher value lateral forces

7.2 Numerical analysis using RS3 software

As it is mentioned in introduction of this Chapter, the three dimensional analyses of laterally loaded piles are performed using Rocscience RS3 [93], finite element software for geotechnical analysis. For each analysed model, the finite element mesh was generated automatically.

7.2.1 Monotonically loaded single pile

Three-dimensional model of a laterally loaded single pile is presented on Figure 7.4. Automatic mesh generator was used to generate 2552 nodes and 9229 elements on a domain dimensions a = 10 m, b = 10 m and z = 20 m. Figure 7.5 presents the model with generated mesh. As it is mentioned before, the pile was modelled using solid elements and loaded by applying the prescribed displacement. Increments of loading displacements were the same as at the field test: 2 mm of head displacement per step, as it defined in Section 5.7. Two different soil flow law were done: adopted associated and non-associated flow law. Pile was modelled using non-associated flow law. The results of the

numerical analysis conducted for laterally loaded single pile are presented on Figures 7.6 and 7.7.
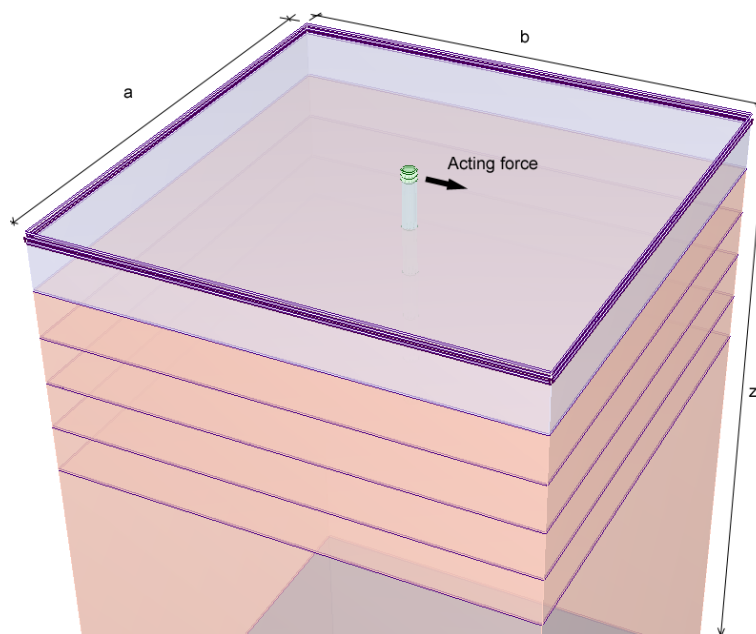
FIGURE 7.4: Geometry of a 3D model of single pile
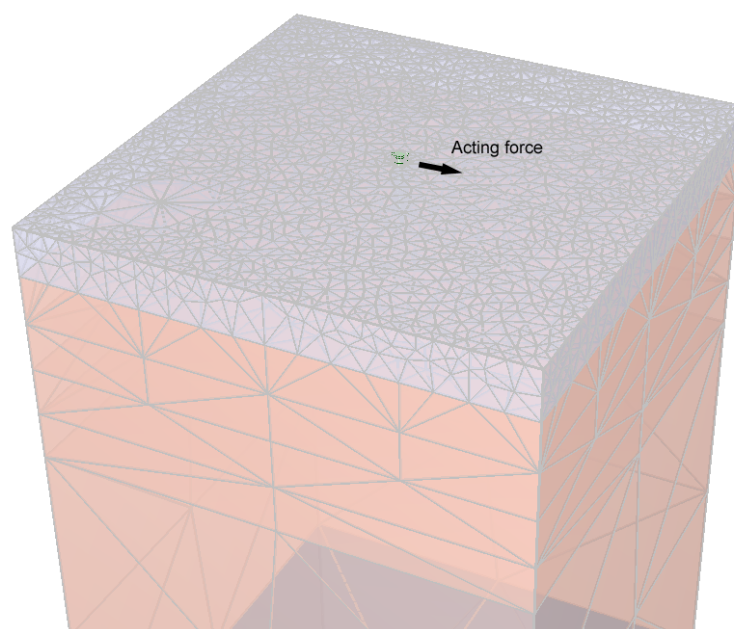
FIGURE 7.5: Generated FE mesh of a 3D model of single pile with 2552 nodes and 9229 elements

From the comparison of the computed and measured results, it is concluded that the dilatancy does not have so much influence as it considered before the

FIGURE 7.6: Presentation of measured and computed pile displacements for
pile head displacement of 2mm, 4mm, 6mm and 8mm for Pile 2

FIGURE 7.7: Measured and computed pile displacements for pile head displacement of 20mm, 30mm, 40mm and 50mm for Pile 2

modelling. Main reason for that could be the fact that the stresses in soil produced by the pile movements are too small to trigger the dilative behaviour of present sand-gravel mixture of soil.

7.2.2 Monotonically loaded two piles in line

The same procedure of modelling was used, as it is discussed in previous Sub-section 7.2.1, for two pile in line. Three-dimensional model is presented on Figure 7.8. Automatic mesh generator was used to generate model with 2935 nodes and 11161 elements. Dimensions of the domain are the same like in previous analysis: a = 10 m, b = 10 m and z = 20 m. Generated mesh for two piles in line model is presented on Figure 7.9. Piles were loaded by applying the prescribed displacement in the same way as they were loaded during the field testing. The results of the numerical analysis of a two piles in line presented on Figures 7.10 and 7.11 for Pile 3, and Figures 7.12 and 7.13 for Pile 4.
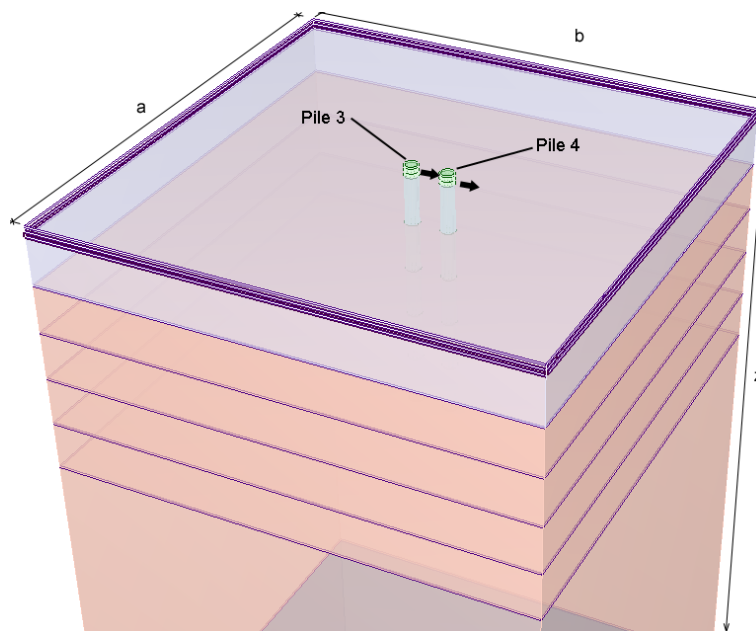
FIGURE 7.8: Geometry of a 3D model for group of *2 by 1* piles

From the comparison of the computed and measured results, it is concluded that the dilatancy does not have so much influence either in this example as it considered before the modelling. Main reason for that could be in the fact that the stresses in soil produced by the piles movement are also too small to trigger the dilative behaviour of present sand-gravel mixture of soil.
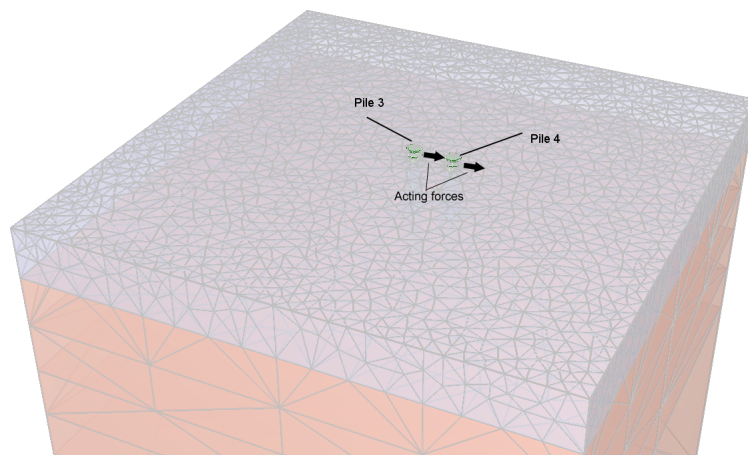
FIGURE 7.9: Generated FE mesh of a 3D model for group of *2 by 1* piles with 2935 nodes and 11161 elements
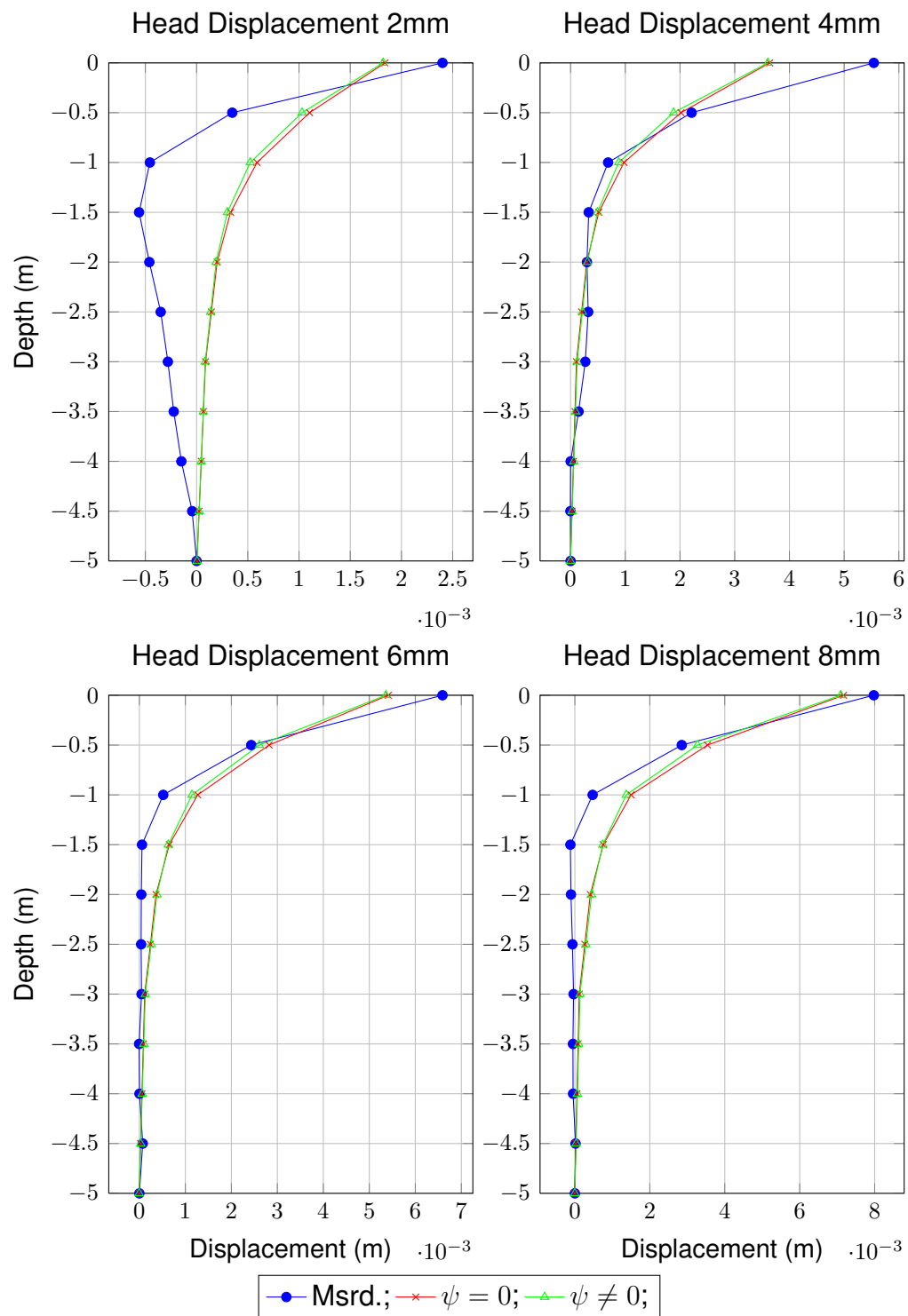
FIGURE 7.10: Measured and computed pile displacements for pile head displacement of 2mm, 4mm, 6mm and 8mm for Pile 3
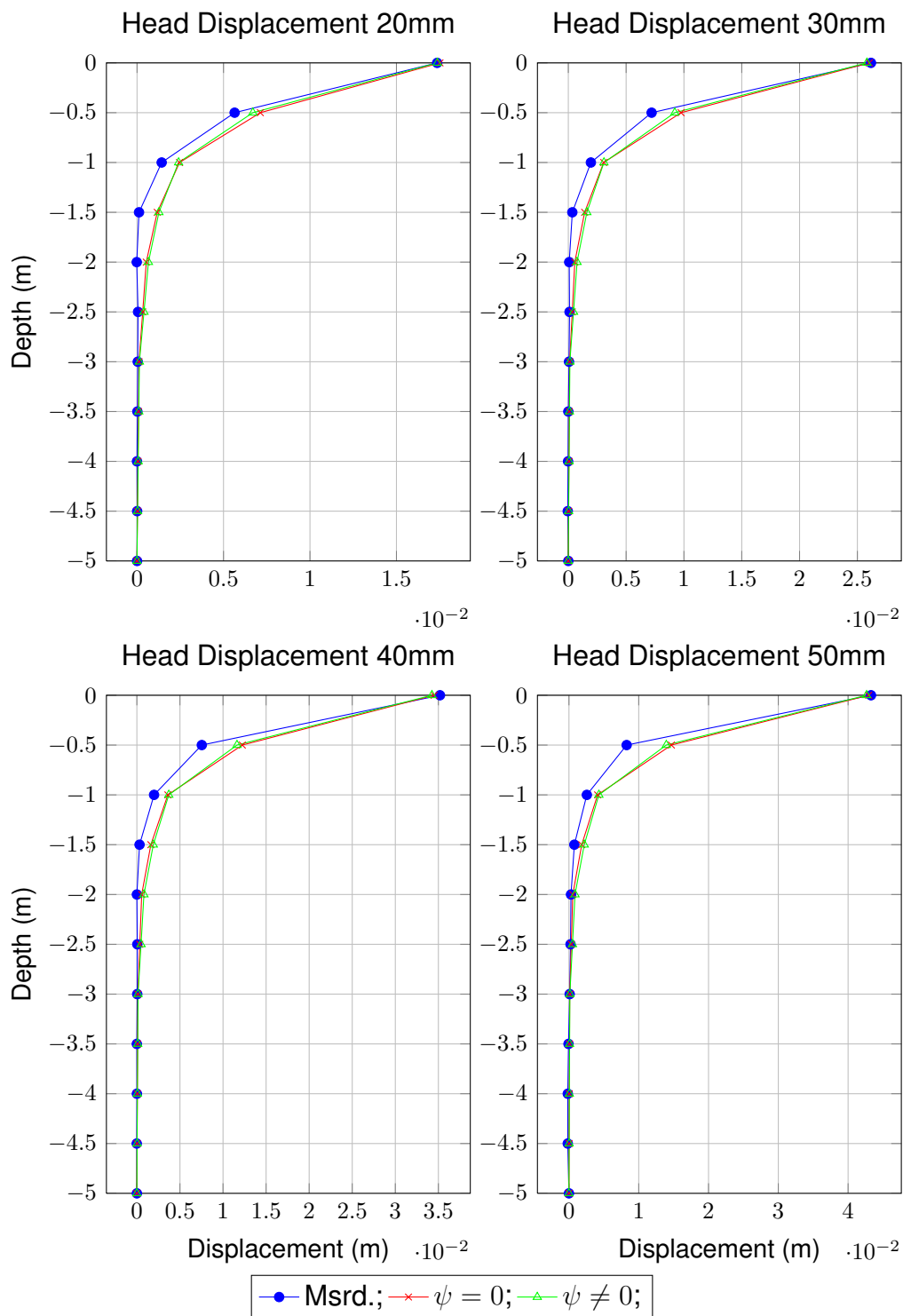
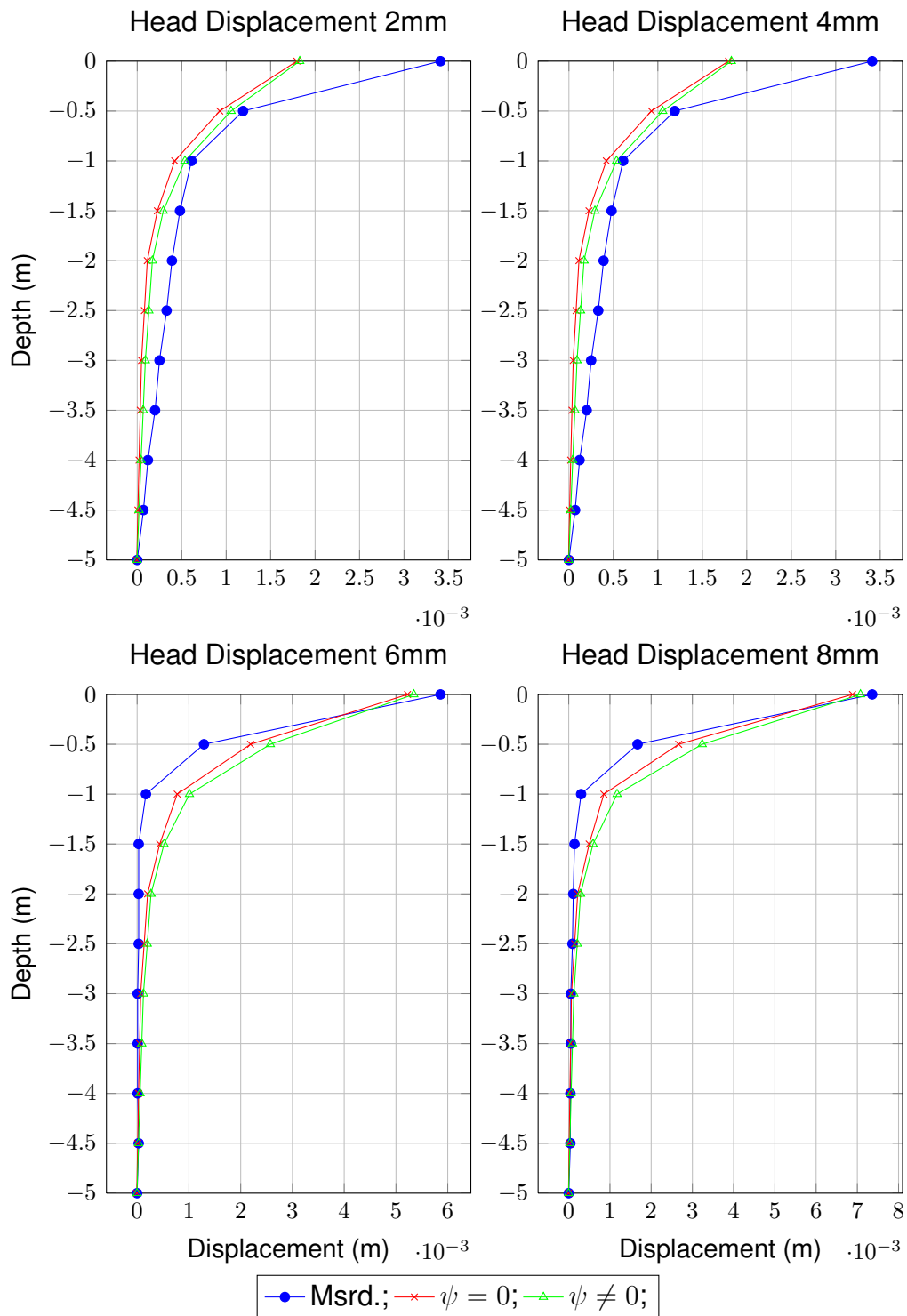FIGURE 7.11: Measured and computed pile displacements for pile head displacement of 20mm, 30mm, 40mm and 50mm for Pile 3
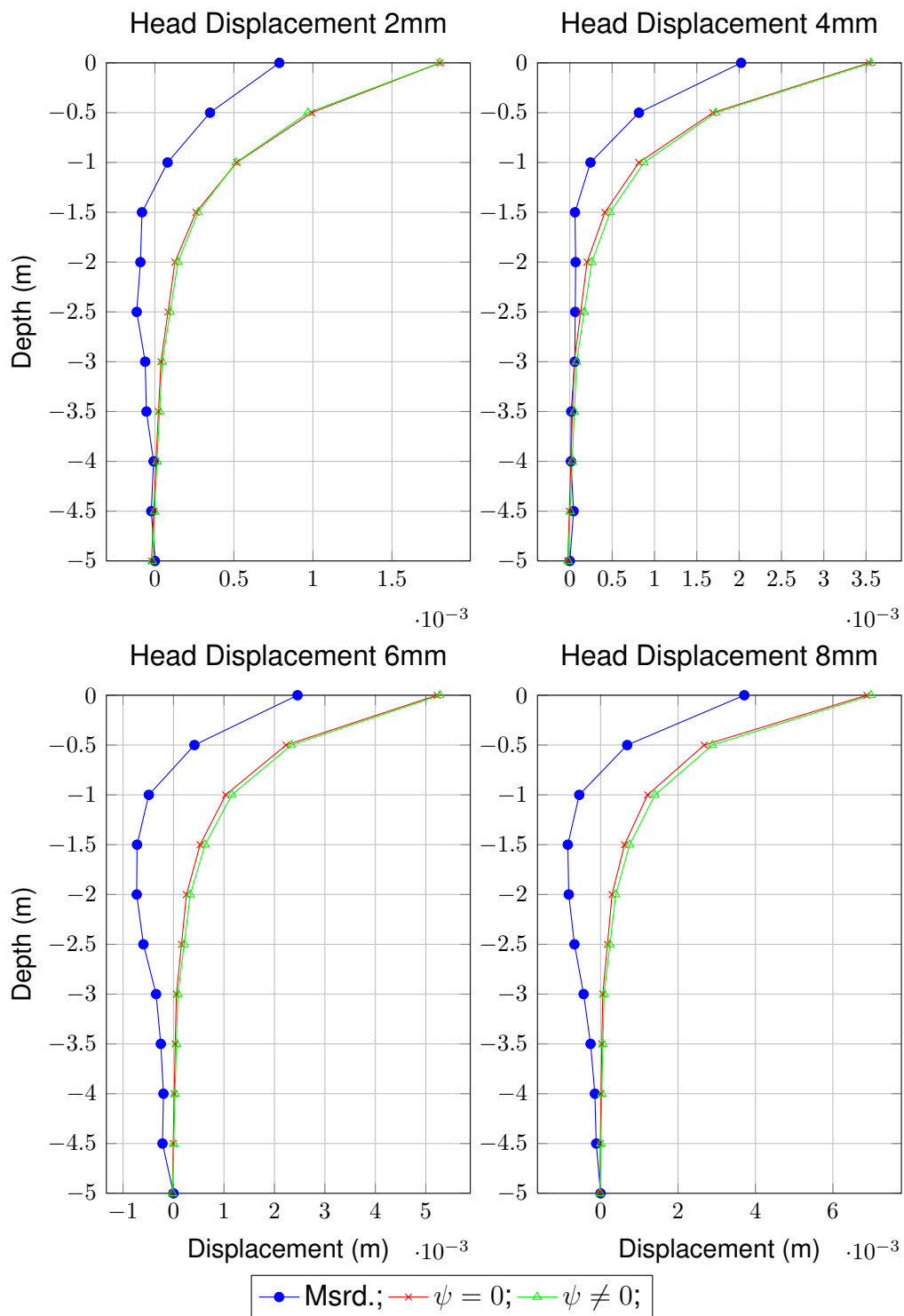
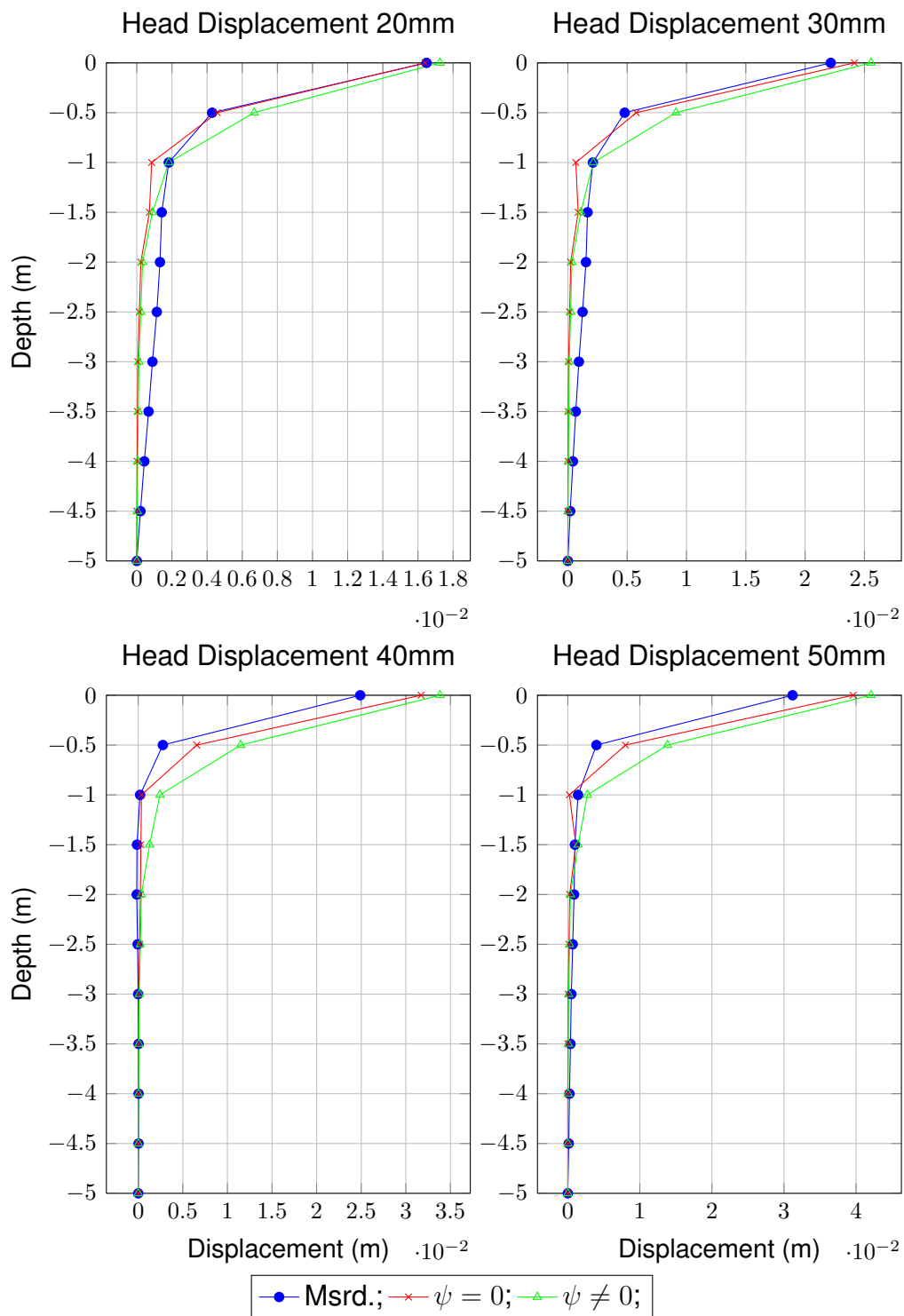FIGURE 7.12: Measured and computed pile displacements for pile head displacement of 2mm, 4mm, 6mm and 8mm for Pile 4
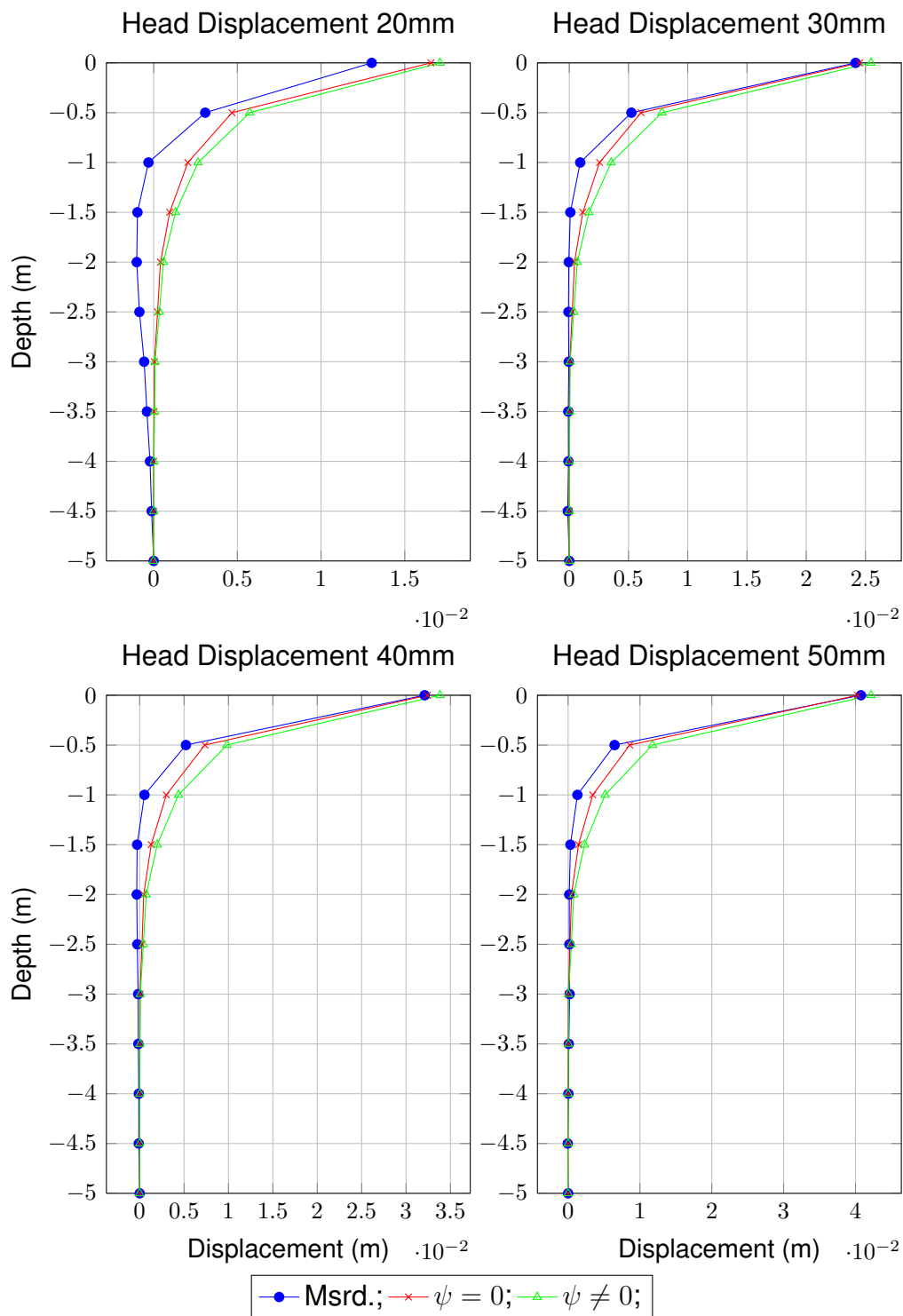
FIGURE 7.13: Measured and computed pile displacements for pile head displacement of 20mm, 30mm, 40mm and 50mm for Pile 4

7.2.3 **Monotonically loaded group of 2 *by* 3 piles**

Three dimensional model of group of *2 by 3* piles is presented in Figure 7.14. Same modelling procedure was used as it is discussed in previous sections. Automatic mesh generator, generated 5349 nodes and 23209 elements. Dimension of domain is the same as it is in previous examples: domain dimensions are: a = 10 m, b = 10 m and z = 20 m. Finite element mesh is presented with Figure 7.15. Piles were loaded with prescribed displacement, as they were loaded during the field test. Two kind of soil flow laws were used here as well: the one with associated and the non-associated flow laws. Pile was modelled using non-associated flow law. The results of numerical analyses are presented on Figures 7.16, 7.17, 7.18 and 7.19 for Piles 5, 6, 7 and 8, respectively.
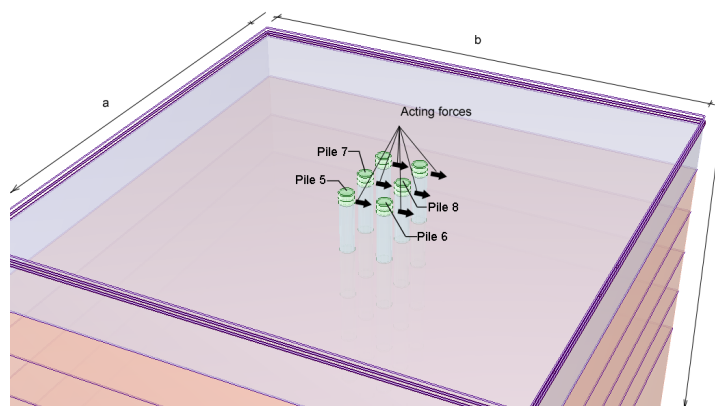
FIGURE 7.14: Geometry of a 3D model for group of *2 by 3* piles
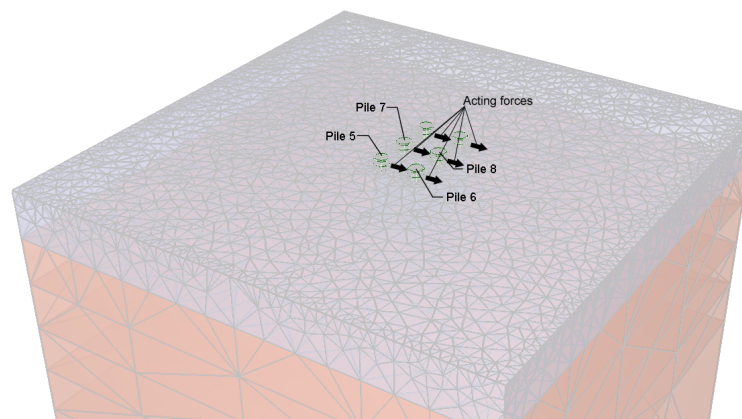
FIGURE 7.15: Generated FE mesh of a 3D model for group of *2 by 3* piles with 5349 nodes and 23209 elements
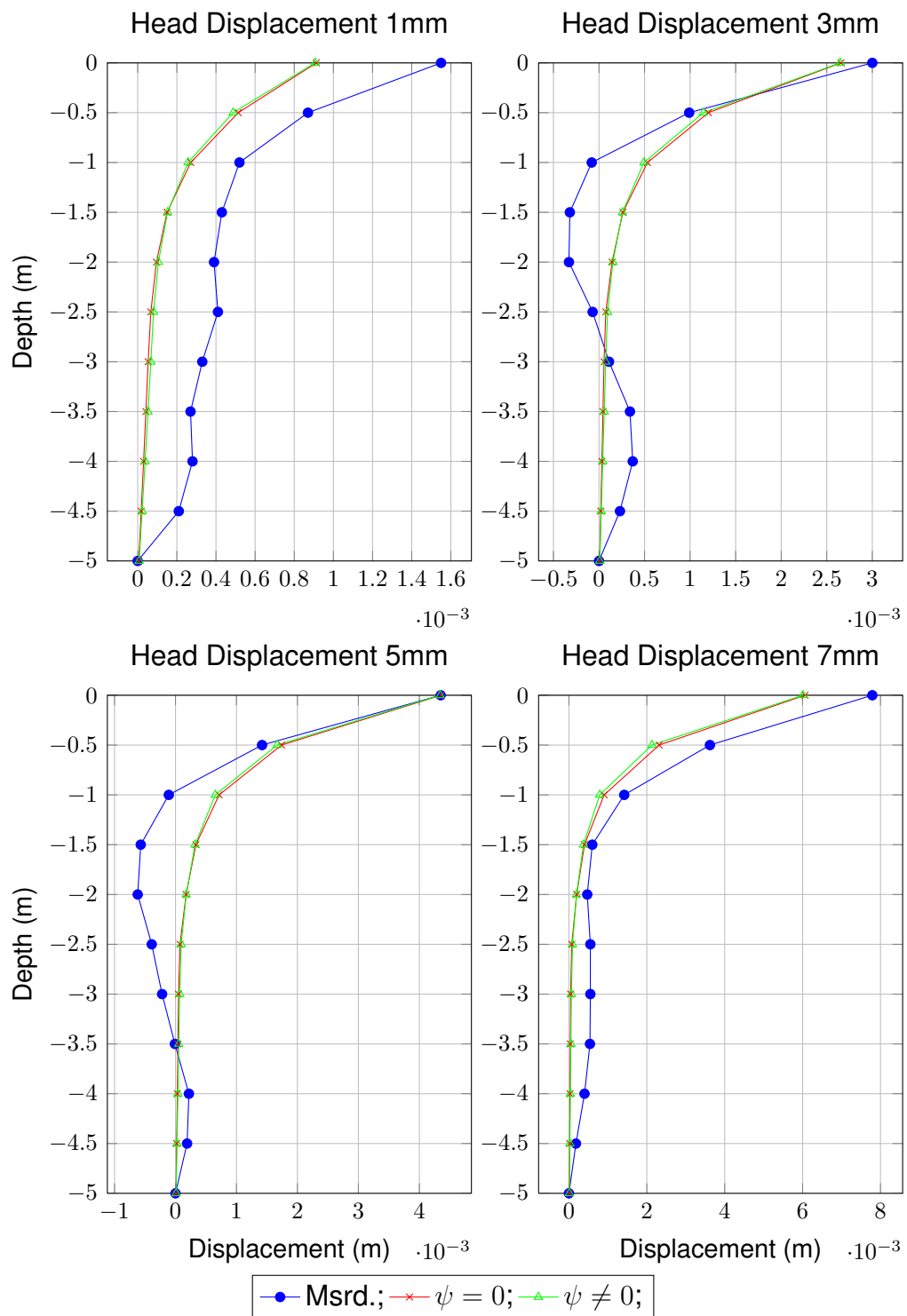
FIGURE 7.16: Measured and computed pile displacements for pile head displacement of 1mm, 3mm, 5mm and 7mm for Pile 5
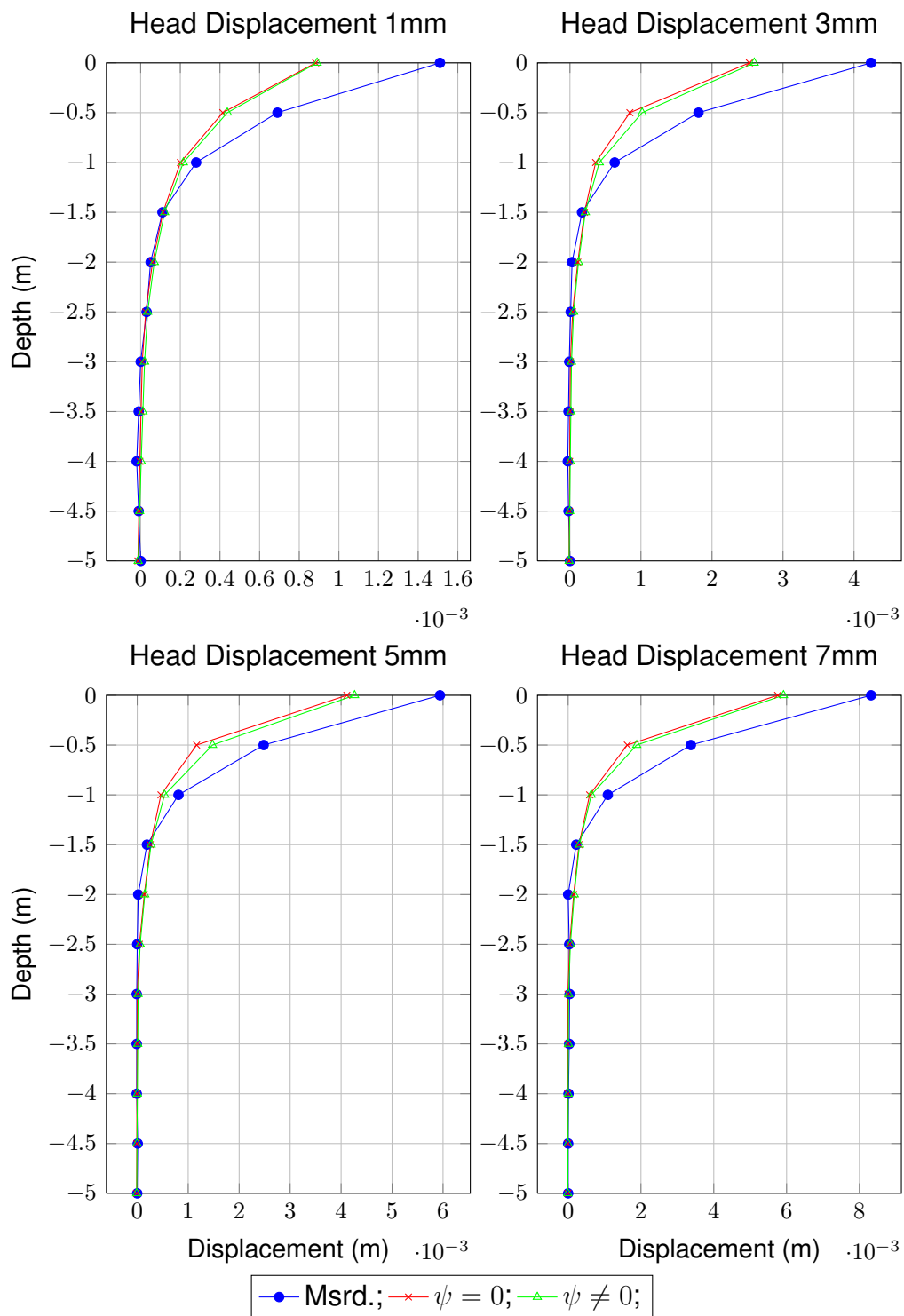
FIGURE 7.17: Measured and computed pile displacements for pile head displacement of 1mm, 3mm, 5mm and 7mm for Pile 6
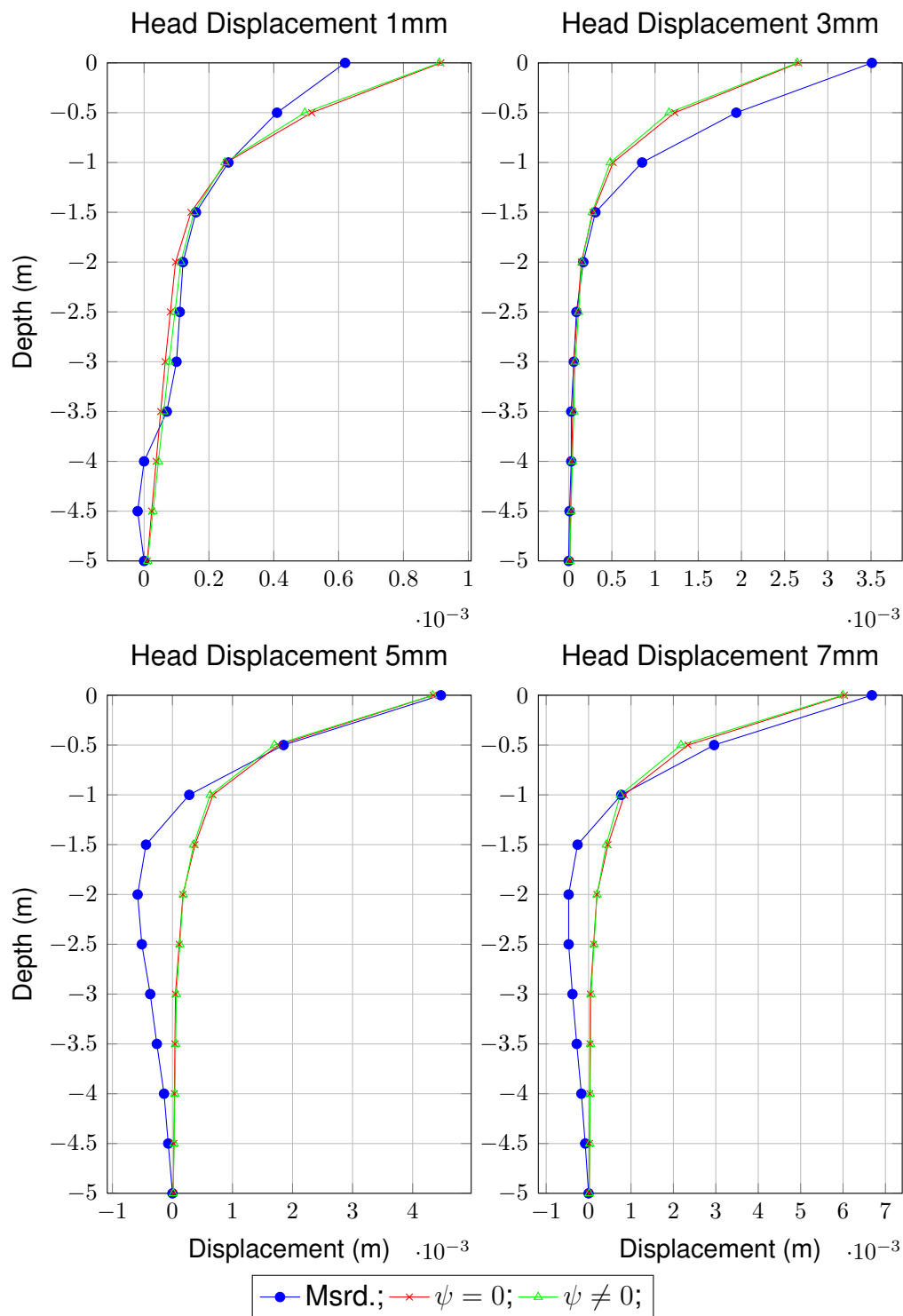
FIGURE 7.18: Measured and computed pile displacements for pile head displacement of 1mm, 3mm, 5mm and 7mm for Pile 7
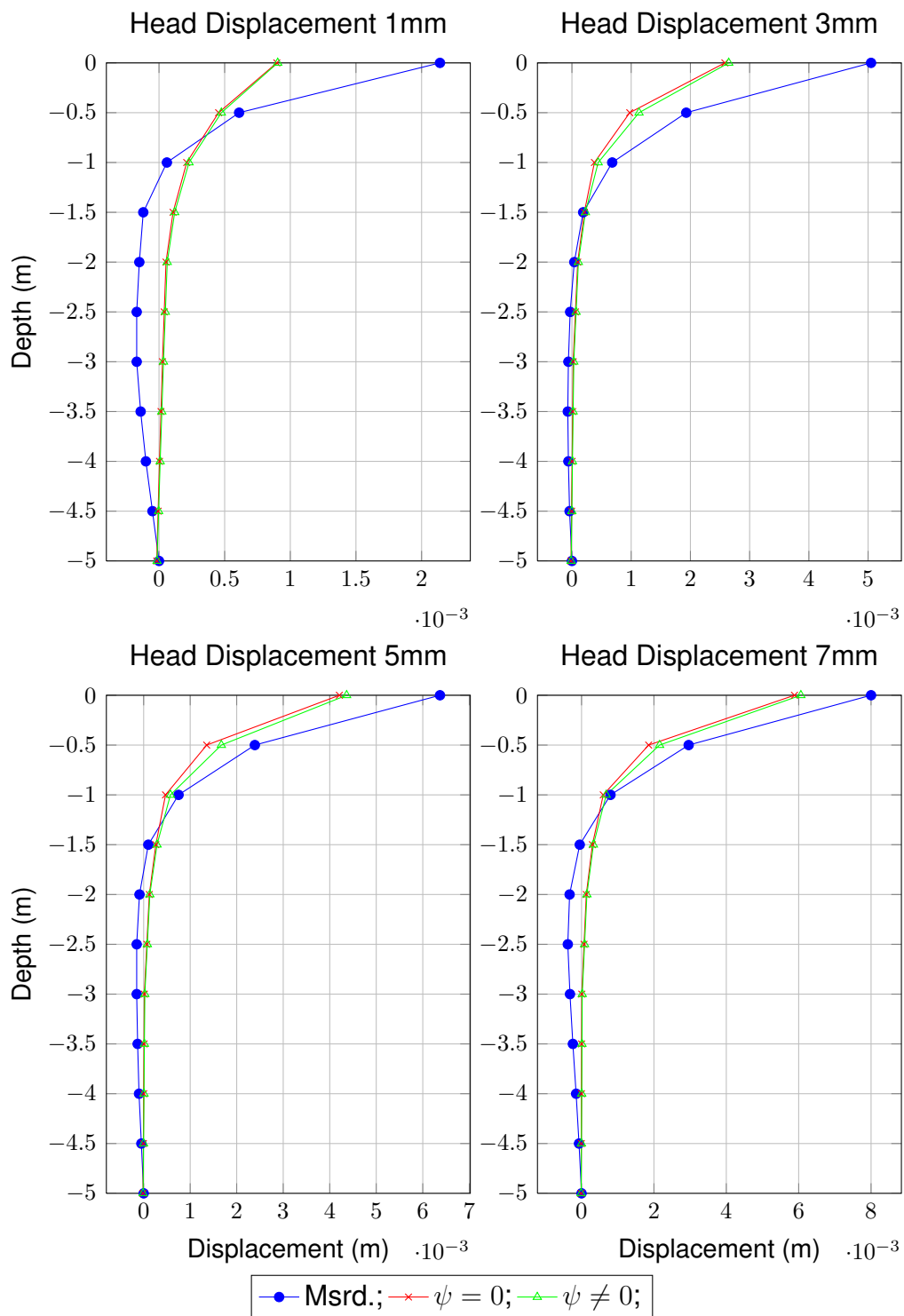
FIGURE 7.19: Measured and computed pile displacements for pile head displacement of 1mm, 3mm, 5mm and 7mm for Pile 8

From the comparison of the modelled and measured results of group of *2 by 3* piles, it is concluded that the dilatancy also does not have so much influence.The stresses in soil produced by the piles movement are also too small to trigger the dilative behaviour of present sand-gravel mixture of soil.

Though the displacements of piles in tests are small they are still large enough to produce the displacement of inclinometer casings installed outside of piles as presented on Figure 5.13. Displacements of inclinometer casings in front of leading piles were in order of 3 mm, while the inclinometer casings behind trailing piles have displacements of maximum 2 mm. Since the piles had defined direction of loading displacements, displacements along the side of group of piles have not been measured. Thus, the full 3D effect of group of piles behaviour cannot be fully displayed but it does have to exist due to measured displacements behind and in front of the group of piles.

Chapter 8

Conclusions

8.1 Summary

In geotechnical engineering, piles are one of the possibilities to be used for deep foundation when soil layer with low bearing capacity and high deformability needs to be "bridged". Although their main issue is to withstand vertical forces and capacity, piles very often have to be calculated for lateral capacity where the dominant loading is horizontal. One type of horizontal excitation is earthquake, while another can be water wave. Piles can also be used for landslide stabilization where the weight of a sliding mass acts as a horizontal load. There are many studies regarding laterally loaded piles in cohesionless or cohesive soils, usually described simply as sand and clay, as the two most representative types of cohesionless and cohesive soil.

Behavior of **LLP** in non-cohesive gravely soil material was analysed only in few studies with absence of physical field testing results, and this was the main motivation for this research. There are only some studies which are dealing with **LLP** in gravel fill, between pile connection plate and surrounding soil, while the piles itself were embedded in sand or clay. These studies are not considered in this Thesis. In-field tested **LLP** were completely embedded in natural sandy gravels with pinned head connection (with no bending moment in pile head). Piles were made of reinforced concrete with aluminium inclinometer casing installed through the axis of a pile. Length of piles is 5m and piles diameter is

0.25m, giving them slenderness ratio of 20 which makes them slender, or flexible, or so called long piles. The length of pile is governing the mechanism of ultimate lateral force. Piles were reinforced with longitudinal and spiral reinforcement. Axial distance between piles in a group are three diameters and it was chosen based on results from [8, 10, 11, 29, 30, 31, 32, 33, 35, ect.]. Totally of ten piles are tested in following combination:

- Single pile laterally loaded by applying the controlled displacement,

- Single pile laterally loaded by applying of the controlled displacement, unloaded and reloaded by applying the controlled displacement again,

- Group of *2 by 1* group of piles laterally loaded by applying the controlled displacement,

- Group of *2 by 3* group of piles laterally loaded by applying the controlled displacement.

Installed piles were loaded using a displacement control test by steel frame designed and constructed for this field testing. Displacement of piles via steel frame were applied by increasing of the lateral force using hydraulic press with 700bar capacity.

During the pile loading, the deflection of pile was measured using inclinometer probe by inserting inclinometer through the inclinometer casing. There was eight inclinometer casings installed in piles and six inclinometer casings were installed in surrounded soil.

From the results of previous studies it can be concluded that the cohesionless material behaviour is greatly affected by the density of the material. If the material is dense and then exposed to shearing, dilatancy can take place as a consequence of volume change, due to soil particle rearrangement. It has been proven that dilatancy has an influence on laterally loaded pile behaviour but, unfortunately, this was proven only numerically. Presented research had an idea to identify dilatancy in gravels behaviour caused by lateral load of piles.

After **LLP** field testing, the dilatancy behaviour of sandy gravels was analysed in order to obtain bending moment and soil resistance diagrams based on testing results, using the Cesáro summation technique. When the soil resistance and

displacements are known, the *p-y* curves for each laterally loaded pile can be calculated and then is possible to compare the results obtained for the single pile and group of piles and identify influence of group of pile-soil interaction.

8.2 Results

From the obtained field tests results and their analysis, the following conclusions regarding behaviour of **LLP** in natural sandy gravel are made:

- The critical depth for the highest soil resistance in natural sandy gravels is at the depth from 2 to 3 pile diameters,

- The ultimate lateral force for the laterally loaded single pile and group of two piles in line are in good correlation with Patra's equations [20] for determinating ultimate lateral force applied on piles,

- The Cesáro technique provides very good approximation of deflections, bending curves and soil resistance curves for **LLP** if the slenderness ratio is larger than 10,

- Behaviour of **LLP** of natural sandy gravels, probably because high content of sand (50%) in soil material, is very similar to the behaviour of piles embedded in sand,

- The dilatancy behaviour in natural sandy gravels does not present very much influence on the soil–pile interaction as it stated in hypothesis. It is caused by high content of sand (50%) in soil material and relatively small values of displacements.

- **LLP** in natural sandy gravels with approximately equal proportion of sand and gravel are behaving like piles in sand but with higher ultimate soil resistance caused by larger friction angle of the material.

8.3 Further research

Based on the performed test results, and experience gained during the testing, some advices for further research are proposed:

- Various mixtures of sand and gravel should be chosen to test embedded laterally loaded piles. For example, 100% of sand and 0% of gravel, 70% of sand and 30% of gravel, 30% of sand and 70% of gravel, 0% of sand and 100% of gravel. It is expected that with rising of gravel content in the mixture, the dilatancy behaviour should be more expressed.

- Triaxial test of sand and gravel mixture should be performed on the basis of soil loading condition (lateral compression) to see dilatancy behaviour and influence related to the grain size composition and gravel content.

- Based on in-field testing and laboratory results the *p-y* curves for mentioned mixtures of gravel and sand would be developed. It is expected that the dilatancy behaviour should have significant impact on the shape of the *p-y* curves of **LLP**.

Appendices

Appendix A

The Cesáro Sum-Technique

The Cesáro summation, named after the Italian analyst Ernesto Cesáro (1859-1906), is a mathematical method that is assigning a sum to an infinite series. If a series of data converges to $\sum A$, then it is also sumable using the Cesáro sum technique, and has the Cesáro $\sum A$. The most important advantage of this technique is that a series that does not converge may still be well defined using Cesáro sum-technique [87].

The general Cesáro sum is defined as:

$$S_k = C(k, r) \left\{ \sum_{n=0}^{k} a_n \right\} \equiv \frac{C_{r-1}^{k+r-1} s_0 + C_{r-1}^{k+r-2} s_1 + ... + C_{r-1}^{r} s_{k-1} + C_{r-1}^{r-1} s_k}{C_r^{k+r}} \quad \text{(A.1)}$$

where $C_r^k = k! / (r! (k-r)!)$ and the partial sum $s_k = \sum_{n=0}^{k} a_n$.

For computational convenience, the s_k terms are changed to a_k and can be change to conventional Cesáro sum as it shown in equation A.2.

$$S_k = C(k, 1) \left\{ \sum_{n=0}^{k} a_n \right\} \equiv \frac{s_0 + s_1 + ... + s_{k-1} + s_k}{k+1} = \frac{1}{k+1} \sum_{n=0}^{k} (k-n+1) a_n \quad \text{(A.2)}$$

In the equation A.3 to A.6, the Cesáro sum is shown for r equals to 2, 3, 4 and 5.

$$S_k = C(k,2) \left\{ \sum_{n=0}^{k} a_n \right\} \equiv \frac{1}{(k+1)(k+2)} \sum_{n=0}^{k} (k-n+1)(k-n+2)a_n \qquad \text{(A.3)}$$

$$S_k = C(k,3) \left\{ \sum_{n=0}^{k} a_n \right\} \equiv \frac{\sum_{n=0}^{k} (k-n+1)(k-n+2)(k-n+3)a_n}{(k+1)(k+2)(k+3)} \qquad \text{(A.4)}$$

$$S_k = C(k,4) \left\{ \sum_{n=0}^{k} a_n \right\} \equiv \frac{\sum_{n=0}^{k} (k-n+1)(k-n+2)(k-n+3)(k-n+4)a_n}{(k+1)(k+2)(k+3)(k+4)}$$
$$\text{(A.5)}$$

$$S_k = C(k,5) \left\{ \sum_{n=0}^{k} a_n \right\} \equiv \frac{\sum_{n=0}^{k} (k-n+1)(k-n+2)(k-n+3)(k-n+4)(k-n+5)a_n}{(k+1)(k+2)(k+3)(k+4)(k+5)}$$
$$\text{(A.6)}$$

From the engineering purposes it is easier to start with the $n = 1$ as a starting point of the sum, and a_0 term can be left out from the sum resulting the Cesáro sum reduction. Reduced expressions are presented with equations A.7 to A.11.

$$S_k = C(k,1) \left\{ \sum_{n=1}^{k} a_n \right\} \equiv \frac{1}{k} \sum_{n=1}^{k} (k-n+1)a_n \qquad \text{(A.7)}$$

$$S_k = C(k,2) \left\{ \sum_{n=1}^{k} a_n \right\} \equiv \frac{1}{k(k+1)} \sum_{n=1}^{k} (k-n+1)(k-n+2)a_n \qquad \text{(A.8)}$$

$$S_k = C(k,3) \left\{ \sum_{n=1}^{k} a_n \right\} \equiv \frac{\sum_{n=1}^{k} (k-n+1)(k-n+2)(k-n+3)a_n}{k(k+1)(k+2)} \qquad \text{(A.9)}$$

$$S_k = C(k,4) \left\{ \sum_{n=1}^{k} a_n \right\} \equiv \frac{\sum_{n=1}^{k}(k-n+1)(k-n+2)(k-n+3)(k-n+4)a_n}{k(k+1)(k+2)(k+3)} \tag{A.10}$$

$$S_k = C(k,5) \left\{ \sum_{n=1}^{k} a_n \right\} \equiv \frac{\sum_{n=1}^{k}(k-n+1)(k-n+2)(k-n+3)(k-n+4)(k-n+5)a_n}{k(k+1)(k+2)(k+3)(k+4)} \tag{A.11}$$

Having defined Cesáro's sums, general form of the pile deflection expressed through the Fourier's series can be defined as (according to [86]):

$$y(z) = \sum_{i=1}^{n} \mathbf{B}_i \left[1 - \cos \overline{N} \pi z \right] \tag{A.12}$$

where $\mathbf{B}_i$ coefficients of the soil-pile system, z is the depth, $\overline{N} = \frac{2i-1}{2L}$ and L is the length of pile. Equation (A.12) can be rewritten in scalar product as:

$$\mathbf{y}_c = \mathbf{AB} \tag{A.13}$$

where $\mathbf{A}$ is the matrix of Fourier's coefficients presented with equation (A.14) and $\mathbf{B}$ is the vector of soil-pile coefficients.

$$A = \begin{bmatrix} \left[1 - \cos\overline{N}_n\pi z_1\right] & \cdots & \left[1 - \cos\overline{N}_2\pi z_1\right] & \left[1 - \cos\overline{N}_1\pi z_1\right] \\ \left[1 - \cos\overline{N}_n\pi z_2\right] & \cdots & \left[1 - \cos\overline{N}_2\pi z_2\right] & \left[1 - \cos\overline{N}_1\pi z_2\right] \\ \vdots & \cdots & \vdots & \vdots \\ \left[1 - \cos\overline{N}_n\pi z_n\right] & \cdots & \left[1 - \cos\overline{N}_2\pi z_n\right] & \left[1 - \cos\overline{N}_1\pi z_n\right] \end{bmatrix} \tag{A.14}$$

According to Lin et al. [86], least-square rule is applied to the equation (A.13) using the following procedure:

- Obtain square summation error, $\mathbf{S}$

$$\mathbf{S} = (\mathbf{AB} - \mathbf{y}_m)^T (\mathbf{AB} - \mathbf{Y}_m),$$

(A.15)

- Vector $\mathbf{B}$ is obtained by minimising the equation (A.15) according to $\mathbf{B}$

$$\frac{\partial \mathbf{S}}{\partial \mathbf{B}} = \underbrace{2\mathbf{A}^T\mathbf{A}}_{\Gamma} \cdot \mathbf{B} - \underbrace{2\mathbf{A}^T \cdot \mathbf{y}_m}_{\zeta} = 0$$

(A.16)

Solving the system of equation defined with equation (A.16), coefficients of soil-pile system of vector $\mathbf{B}$ can be calculated using the measured values of displacements $\mathbf{y}_m$ as:

$$\mathbf{B} = \Gamma^{-1}\zeta$$

(A.17)

If the deflection of pile is known, then the bending moment M, shear force V and soil reaction p can be easily calculated by differentiating the pile deflection with depth, as it presented using equations (A.18) to (A.21), according to [86]:

$$\theta(z) = \frac{dy(z)}{dz}$$

(A.18)

$$M(z) = EI\frac{d^2y(z)}{dz^2}$$

(A.19)

$$V(z) = \frac{dM}{dz}$$

(A.20)

$$p(z) = \frac{dV}{dz}$$

(A.21)

where $\theta(z)$ is the function of rotation along the pile, $M(z)$ is the function of bending moment along the pile, $V(z)$ is the function of shear force along the pile, $p(z)$ is the function of soil resistance along the pile and EI is the bending stiffness of a pile.

Since Fourier series function can cause ill-posed condition after differentiation [86], the Cesáro sum technique can be used to overcome that issue. Using the defined Cesáro sum's presented by equations (A.7) to (A.11) and applying them to the equations (A.18), (A.19), (A.20) and (A.21), where $a_n = \mathbf{B}_n \left(1 - \cos \overline{N}\pi z\right)$,

those equations can be expressed with the Cesáro sum coefficients as:

$$y(z) = \frac{1}{k} \sum_{n=1}^{k} (k - n + 1)\mathbf{B}_n \left(1 - \cos \overline{N}\pi z\right) \tag{A.22}$$

$$\theta(z) = \frac{1}{k(k+1)} \sum_{n=1}^{k} (k - n + 1)(k - n + 2) \cdot \mathbf{B}_n \overline{N}\pi \left(\sin \overline{N}\pi z\right) \tag{A.23}$$

$$M(z) = \frac{1}{k(k+1)(k+2)} \sum_{n=1}^{k} (k-n+1)(k-n+2)(k-n+3)EI \cdot \mathbf{B}_n \overline{N}^2 \pi^2 \left(\cos \overline{N}\pi z\right) \tag{A.24}$$

$$V(z) = \frac{1}{k(k+1)(k+2)(k+3)} \sum_{n=1}^{k} (k - n + 1)(k - n + 2)(k - n + 3)(k \tag{A.25}$$
$$- n + 4)EI \cdot \mathbf{B}_n \overline{N}^3 \pi^3 \left(- \sin \overline{N}\pi z\right)$$

$$p(z) = \frac{1}{k(k+1)(k+2)(k+3)(k+4)} \sum_{n=1}^{k} (k - n + 1)(k - n + 2)(k - n \tag{A.26}$$
$$+ 3)(k - n + 4)(k - n + 5)EI \cdot \mathbf{B}_n \overline{N}^4 \pi^4 \left(- \cos \overline{N}\pi z\right)$$

Appendix B

Loading Frame Joint Connections and Elements Calculation

Steel loading frame (Figure B.1) consists of multiple steel elements and the most important elements are referenced as Element 4 and Element 5. Those two elements should have to withstand the biggest force on the loading frame which is calculated to be 85 kN. The internal forces and cross-section dimensions of the elements were calculated based on Eurocode3 norm for steel constructions [94]. Steel characteristic has been taken as the same through the whole calculation, as well as for connection bolts. All necessary characteristics are summarised in table B.1. The following calculations have been performed, for each element in the loading frame:

- Calculation of a bolt on shear,

- Calculation of steel section against the pressure on the hole boundary,

- Calculation of a bolt on tension,

- Calculation of welds.

B.1 Calculation of the Element 4

Calculation of Element 4 consists of bolt control on shear resistance, bolt control on tension resistance and weld resistance. Isometric view of Element 4 is

TABLE B.1: Parameters needed for joint computations

Parameter	Value	Parameter	Value
Bolt grade	5.6	d	22mm
c_1	0.6	d_0	24mm
f_{ub}	500MPa	a	0.569
f_u	360MPa	β_w	0.8
$A_s^{(22)}$	$303mm^2$	t	8mm
$A_s^{(16)}$	$70.7mm^2$	α_w	3mm
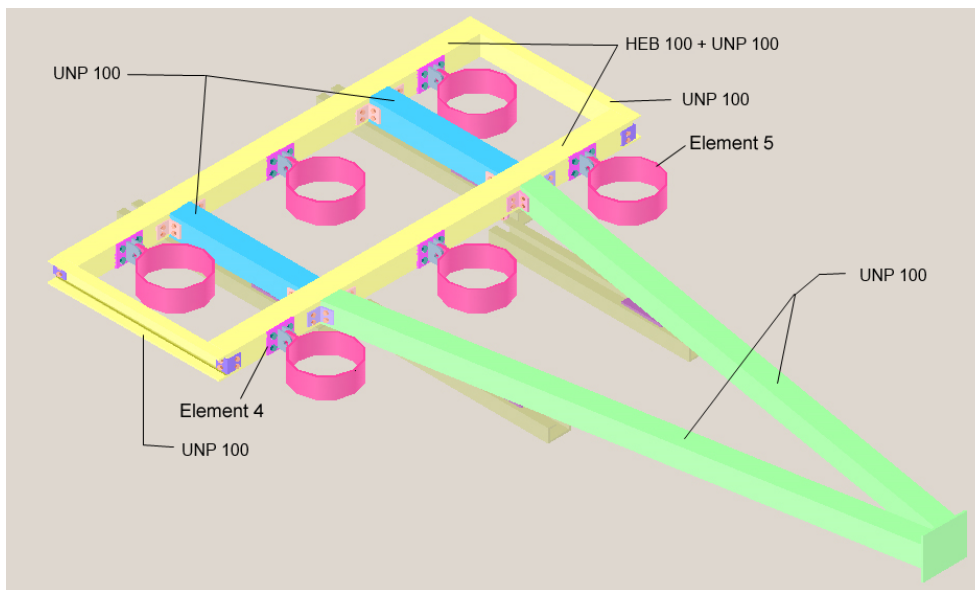
FIGURE B.1: Isometric view on steel loading frame

presented in Figure B.2(a) while the left side view is presented on Figure B.2(b). Maximum effective force that the connection has to withstand is $F_{Ed} = 85kN$.

B.1.1 Control of the pressure on the hole boundaries

- Characteristic resistance force on hole boundary

$$F_{b,Rk}^{(22)} = 2.5\alpha \cdot f_u \cdot d \cdot t = \tag{B.1}$$

$$= 2.5 \cdot 0.569 \cdot 360 \cdot 22 \cdot 14 \tag{B.2}$$

$$= 157.727kN \tag{B.3}$$

(a) Isometric view of Element 4   (b) Top and left-side view of Element 4
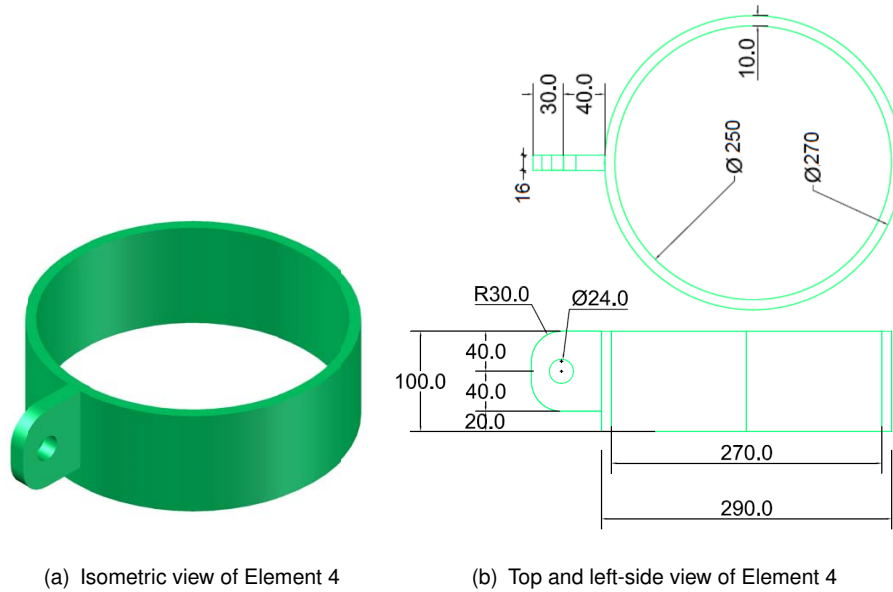
FIGURE B.2: View of Element 4

- Resistance force per one hole

$$F_{b,Rd}^{(22)} = \frac{F_{b,Rd}^{(22)}}{1.25} = 126.18 kN \tag{B.4}$$

- Sum resistance force per number of hole pressure

$$F_{b,Rd,uk}^{(22)} = 1 \cdot F_{b,Rd}^{(22)} = 126.18 kN \tag{B.5}$$

Sum resistance force of 22 mm diameter hole has grater resistance than the effect load ($F_{Ed} < F_{b,Rd,uk}^{(22)}$).

B.1.2   Control of the resistance of welded part

- Characteristic force of welded part

$$F_{w,Rk} = \frac{f_u}{\sqrt{3}\beta_w} \cdot \alpha_w \cdot L \tag{B.6}$$

$$= \frac{360}{\sqrt{3} \cdot 0.8} \cdot 3 \cdot 100 \tag{B.7}$$

$$= 77.94 kN \tag{B.8}$$

- Resistance force of a weld

$$F_{w,Rd} = \frac{F_{w,Rk}}{1.25} = 62.35 kN \tag{B.9}$$

- Sum resistance force per number of welded lines

$$F_{w,Rd,uk} = 2 \cdot F_{w,Rd} = 124.7 kN \tag{B.10}$$

Sum resistance force per number of welded lines is grater than the effect load $(F_{Ed} < F_{w,Rd,uk})$.

B.2 Control of the Element 5

Calculation for Element 5 consists of bolt control on shear resistance, bolt control on tension resistance and weld resistance as it follows. Isometric view on Element 5 is presented in Figure B.3(a) while left side view is presented on Figure B.3(b).

(a) Isometric view of Element 5   (b) Left-side view of Element 5
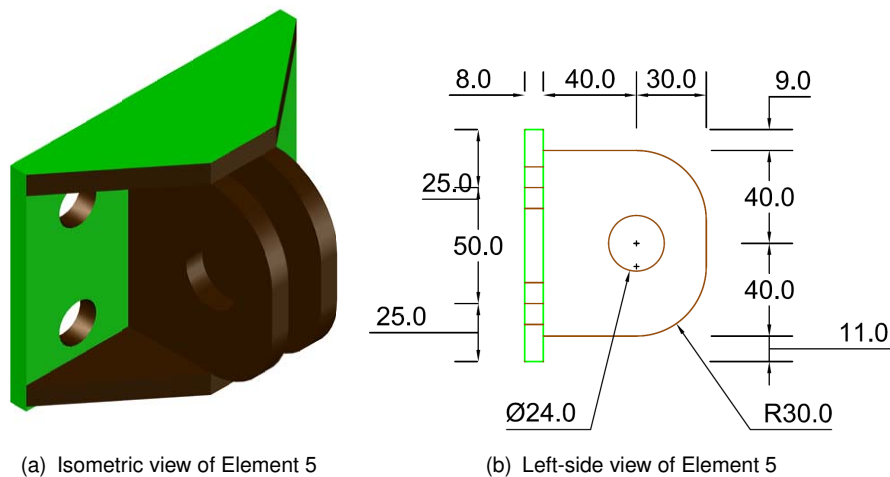
FIGURE B.3: View on Element 5

B.2.1 Resistance of a bolt on shear

- Characteristic resistance force of bolt on shear

$$
\begin{aligned}
F_{v,Rk}^{(22)} &= c_1 \cdot f_{ub} \cdot A_s^{(22)} \\
&= 0.6 \cdot 500 \cdot 303 \\
&= 90.9 kN
\end{aligned}
\tag{B.11}
$$

- Resistance force per one shear plane

$$
F_{v,Rd}^{(22)} = \frac{F_{v,Rk}^{(22)}}{1.25} = 72.72 kN
\tag{B.12}
$$

- Sum resistance force per number of shearing plane

$$
F_{v,Rd,uk}^{(22)} = 2 \cdot F_{v,Rd}^{(22)} = 145.44 kN
\tag{B.13}
$$

Sum resistance force per number of shearing plane is grater then the effect load $(F_{Ed} < F_{v,Rd,uk}^{(22)})$.

B.2.2 Control of the pressure on the hole boundaries

- Characteristic force

$$
F_{b,Rk}^{(22)} = 2.5\alpha \cdot f_u \cdot d \cdot t =
\tag{B.14}
$$

$$
= 2.5 \cdot 0.569 \cdot 360 \cdot 22 \cdot 8
\tag{B.15}
$$

$$
= 90.2 kN
\tag{B.16}
$$

- Resistance force per one hole pressure

$$
F_{b,Rd}^{(22)} = \frac{F_{b,Rd}^{(22)}}{1.25} = 72.16 kN
\tag{B.17}
$$

- Sum resistance force pre number of hole pressure

$$
F_{b,Rd,uk}^{(22)} = 2 \cdot F_{b,Rd}^{(22)} = 144.32 kN
\tag{B.18}
$$

Sum resistance force per number of hole pressure is grater then the effect load $(F_{Ed} < F_{b,Rd,uk}^{(22)})$.

B.2.3 Resistance of bolts on tension force

- Characteristic force of resistance of bolts on tension force

$$F_{t,Rk}^{(16)} = 0.9 \cdot f_{ub} \cdot A_s^{(16)} \tag{B.19}$$

$$= 0.9 \cdot 500 \cdot 70.7 \tag{B.20}$$

$$= 31.815 kN \tag{B.21}$$

- Resistance force per one bolt

$$F_{t,Rd}^{(16)} = \frac{F_{t,Rk}^{(16)}}{1.25} = 25.452 kN \tag{B.22}$$

- Sum resistance force per number of bolts on which tension force is acting

$$F_{t,Rd,uk}^{(16)} = 4 \cdot F_{t,Rd}^{(16)} = 101.81 kN \tag{B.23}$$

Sum resistance force per number of bolts on which tension force is acting is grater then the effect load $(F_{Ed} < F_{b,Rd,uk}^{(22)})$.

B.2.4 Resistance of welded parts

- Characteristic force of welded part

$$F_{w,Rk} = \frac{f_u}{\sqrt{3}\beta_w} \cdot \alpha_w \cdot L \tag{B.24}$$

$$= \frac{360}{\sqrt{3} \cdot 0.8} \cdot 3 \cdot 82 \tag{B.25}$$

$$= 63.913 kN \tag{B.26}$$

- Resistance force of a weld

$$F_{w,Rd} = \frac{F_{w,Rk}}{1.25} = 51.13 kN \tag{B.27}$$

- Sum resistance force per number of welded lines

$$F_{w,Rd,uk} = 2 \cdot F_{w,Rd} = 102.26 kN \tag{B.28}$$

Sum resistance force per number of welded lines is grater than the effect load $(F_{Ed} < F_{w,Rd,uk})$.

Appendix C

Seismic refraction

Seismic refraction method is based on the refraction of elastic waves of the boundary of two layers which velocities satisfy conditions $V_2 > V_1$ where V_1 is the velocity in upper layer media and V_2 is the velocity in lower layer media.

Elastic wave is generated on the surface and it starts to spread with the velocity in the upper layer. The most important wave is the one which strikes the boundary of layers at some critical angle, which is called *angle of total reflection*. According to Huygense's principle, the wave will come back to the surface after passing the lower level with velocity V_2, where it is registered by the geophones. From the geometry of geophones, ignition points on the surface and time of first arrival of elastic waves (figure C.1), *s-t* diagrams are developed, usually called dromochrones (figure C.2), which are used to establish depths and space arrangement of elastic discontinuities.

C.1 Field data aquisition

Seismic refraction testing is conducted in the longitudinal profile with the length *L* where equally spaced geophones are placed, whose distance is *d*. Various number of geophone can be placed (usually 12, 24 or 48) on a 2 to 5m spacing. Geophones are standing still while the ignition point is movable. Geometrical arrangement can be depicted from figure C.3.
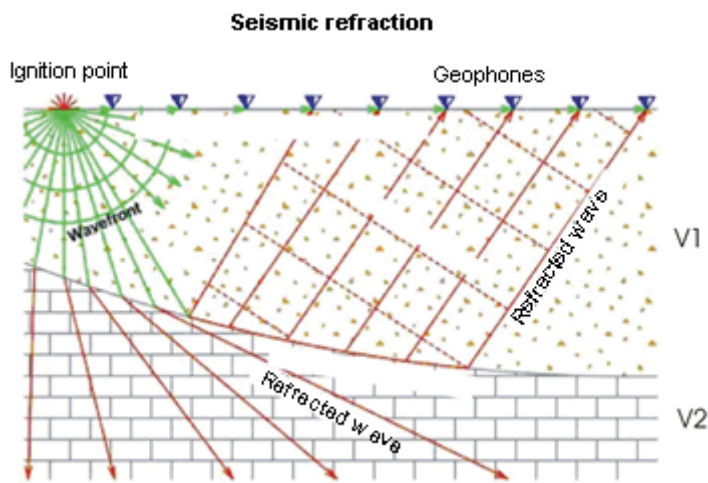
FIGURE C.1: Sketch of seismic refraction [95]
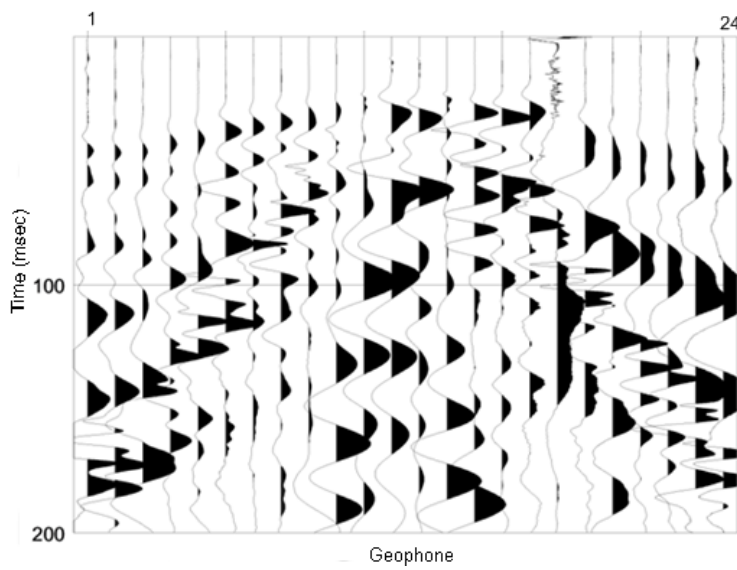
FIGURE C.2: Seismic refraction of P-waves from 24 geophones [95]
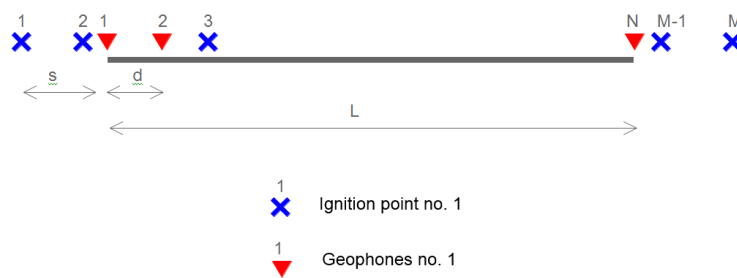
FIGURE C.3: Geometry of recording arrangement [95]

Total length of analysed profile, number of testing channels and their distance is determinate according to the need of researcher, and it is usually determined by the profile depth and resolution. Usually when the depth is set, the distance between geophones is acquired.

C.2   Delta ($\triangle$) - T - V Method

The delta ($\triangle$)-t-v method is the procedure of inverse modelling proposed by Gebrande and Miller [96]. It is based on assumption that the velocity is slightly changed with the change of the depth. The first arrival of waves are sorted for each common mid point and according to that, influence of readout error is reduced. Basic assumption of the method is that the gradient of velocity in each layer is constant [97]. The path od seismic beam on a horizontal distance $\triangle$ from the source of ignition to the receiver is defined by circular segments in each layer (figure C.4)
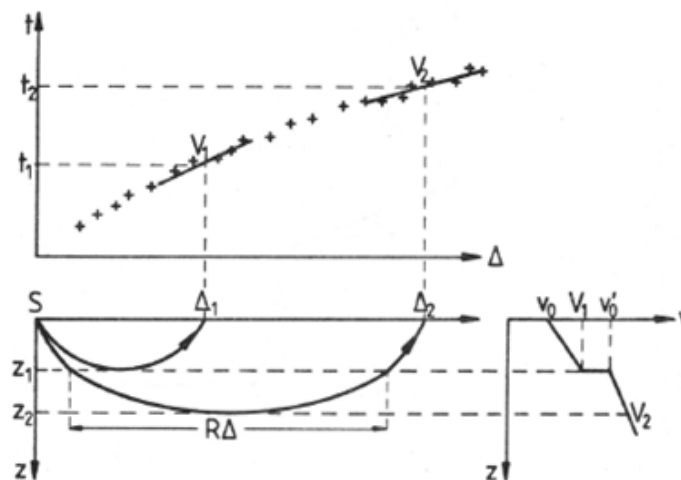
FIGURE C.4: Multilayered model [95]

For a simple model of horizontal layer showed with figure C.5 with the thickness h with the point of ignition and the receiver on a surface, and the belonging beam which path touches the bottom of layer, the following expressions arise according to Gebrande and Miller [96]:
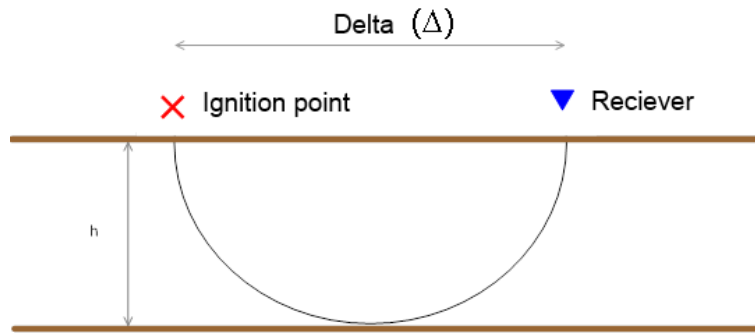
FIGURE C.5: Model of horizontal layer [95]

$$\Delta = \frac{2 \cdot \sqrt{1 - p^2 \cdot b^2}}{p \cdot \gamma} \qquad (C.1)$$

$$t = \frac{2}{\gamma} \log \left(1 + \frac{\sqrt{1 - p^2 \cdot b^2}}{p \cdot \gamma} \right) \qquad (C.2)$$

$$\beta = b + \gamma \cdot h \qquad (C.3)$$

$$p = \frac{1}{\beta} \qquad (C.4)$$

where:

- Δ is the distance between ignition point and geophone (receiver),

- p parameter of a beam,

- γ gradient of velocity inside layer,

- b velocity on the top of the layer,

- β velocity at the bottom of layer.

From equations C.1 - C.4 it can be obtained:

$$\Delta(\beta) = \frac{2}{\gamma} \cdot \sqrt{\beta^2 - b^2} \qquad (C.5)$$

$$t(\beta) = \frac{2}{\gamma} \arccos\left(\frac{\beta}{b}\right) \tag{C.6}$$

Procedure is iterative and defined as:

- The velocity at the bottom layer (β) is calculated directly from the curves of the first range,

- The velocity at the top of the layer (b) is calculated fro the equation C.5 and C.6,

- With knowing the Δ, β and b, equation C.7 gives the gradient of velocity inside layer,

$$\gamma = \frac{2}{\Delta}\sqrt{\beta^2 - b^2} \tag{C.7}$$

- The depth of the layer is calculated from equation C.3.

After the parameters of the first layer are established according to mentioned procedure, for each beam with the distance Δ grater then the one for upper layer, distance (Δ') and time t' are corrected for the effect of upper layer according to Gibson et al. [97]. The parameters of the next layer are calculated with the new iteration in which corrected values of Δ' and t' are taken into consideration.

Appendix D

Multichannel analysis of surface waves (MASW)

Multichannel Analysis of Surface Waves (**MASW**) is the seismic geophysics method developed at the University of Kansas, Kansas Institute of Geological Survey [98]. It is based on the analysis of surface waves and the fact that the surface waves are dispersive (the velocity is changed with the change of frequency). MASW method is used to obtain the layout of transverse waves with the depth of geological profile.

The procedure of obtaining the velocity od transversal wave from phase velocity of surface wave is following:

- Recording of surface wave on the field,

- Calculating the curve of dispersion of recorded surface wave,

- Calculating the profile of transversal wave velocity arrangement obtained from dispersion curve.

Dispersion curve represents the dependance of velocity of surface wave and wave length frequency. Surface wave is recorded at a specific number of geophones set at the field with the equal distance dx among them. From obtained seismic record, phase velocities are calculated (C_f) for different wave frequencies. The procedure is based on the expression D.1
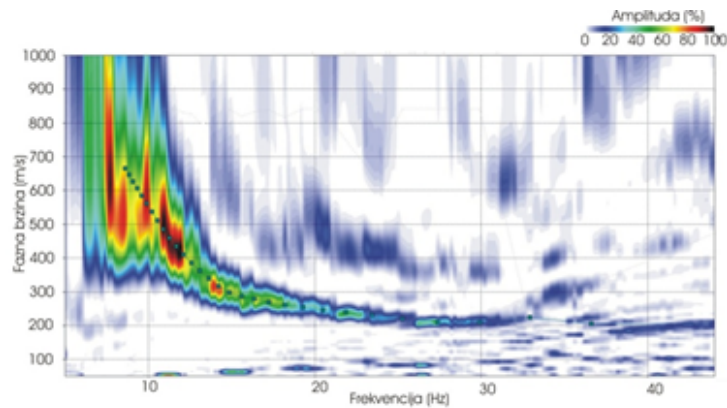
FIGURE D.1: Dispersion curve [95]

$$C_f = \frac{dx}{\Delta_{tf}} \tag{D.1}$$

where:

- C_f is the phase velocity for each frequency,

- dx is the distance between geophones,

- Δ_{tf} is the difference in time when surface wave arrives on neighbour geophones.

The procedure is repeated for every of N frequencies components. The values of obtained amplitudes are put in the graph where frequency is plotted on the abscise axis and phase velocity on ordinate. The following procedure results in a range of pairs of frequencies, f, and phase velocity, C_f, of different amplitudes (figure D.2).

The procedure of inverse modeling is used to obtain the model of change of velocity of transversal wave from dispersion curve. For every each record, after calculated dispersion curve and invert modeling procedure, a 1-dimensional profile of transversal velocity change versus depth is obtained, like this one presented on Figure D.2.
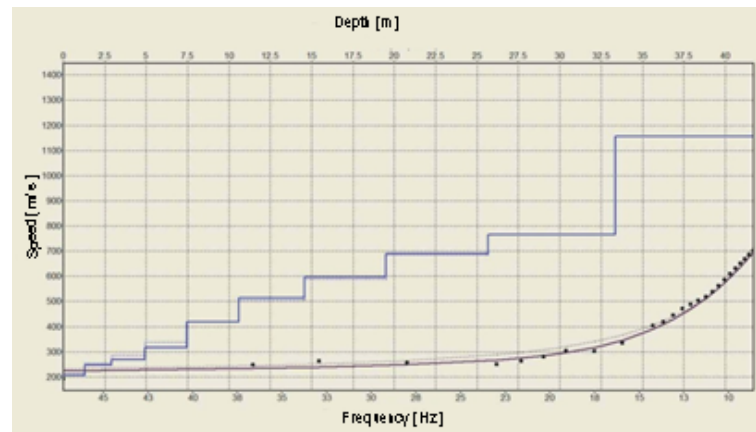
FIGURE D.2: 1-dimensional model of transversal wave velocity [95]

Bibliography

[1] M. Hetenyi. *Beams on Elastic Foundations*. University of MIT Press, 1967.

[2] H. Poulos. Behaviour of laterally loaded piles: I - single piles. *Journal of the Soil Mechanics and Foundation Engineering*, 97(5):711–731, 1971.

[3] H. Poulos. Behaviour of laterally loaded piles: Ii - pile groups. *Journal of the Soil Mechanics and Foundation Engineering*, 97(5):733–751, 1971.

[4] L.C. Reese, W.R. Cox, and F.D. Koop. Analysis of laterally loaded piles in sand. In *Proceedings of the VI annual Offshore Technology Conference*, volume 2, pages 473–485, Huston Texas, 1974.

[5] W.R. Cox, L.C. Reese, and B.R. Grubbs. Field testing of laterally loaded piles in sand. In *Proceedings of the VI annual Offshore Technology Conference*, pages 459–487, Huston Texas, 1974.

[6] L.C. Reese and W. van Impe. *Single piles and pile groups under lateral Loading*. Taylor and Francis, 1 edition, 2001.

[7] Z.Yang and B.Jeremić. Numerical analysis of pile behaviour under lateral loads in layered elastic - plastic soils. *International Journal for Numerical and Analytical Methods in Geomechanics*, 26(14):1385–1406, 2002.

[8] A. Wakai, S. Gose, and K. Ugai. 3-d elasto-plastic finite element analyses of pile foundations subjected to lateral loading. *Soils and foundations*, 39 (1):97–111, 1999.

[9] Y.K. Cheung and P.K.K. Lee. Elastoplastic analysis of soil-pile interaction. *Computers and Geotechnics*, 12(1):115–132, 1991.

[10] D.A. Brown and C.F. Shie. Numerical exploration into group effect response of pile to lateral loading. *Computers and Geotechnics*, 10(3):211–230, 1990.

[11] D.A. Brown and C.F. Shie. Three dimensional finite element model of laterally loaded piles. *Computers and Geotechnics*, 10(3):59–79, 1990.

[12] K.T.Brødbæk, M. Møller, S.P.H. Sørensen, and A.H. Augustsen. Review of p - y relationship in cohesionless soil. Research report, University of Aalborg, 2009.

[13] A.P. Kooijman. Comaparison of an elastoplastic quasi three-dimensional model of laterally loaded piles with field tests. In *Proceedings of the III International Symposium, Numerical Models in Geomechanics (NUMOG III)*, pages 675–682. Niagra Falls, Canada, Elsevier Applied Science, New York, 1989.

[14] E. Pavlovec. *Laterally loaded piles (in Croatian)*. Doctoral thesis, Faculty of Civil Engineering,University of Zagreb, 1985.

[15] A.R. Selby and M.R. Arta. Three-dimensional finite element analysis of pile groups under lateral loading. *Computers and Structures*, 40(5):1329 – 1336, 1991.

[16] Chia-Cheng Fan and James H. Long. Assessment of existing methods for predicting soil response of laterally loaded piles in sand. *Computers and Geotechnics*, 32(4):274 – 289, 2005.

[17] M. Mardfekri, P. Gardoni, and J.M. Roesset. Modeling laterally loaded single piles accounting for nonlinear soil-pile interaction. *Journal of Engineering*, 2013:7, 2013.

[18] S.P. Timoshenko. *Strength of material, Part 1: Elementary theory and problems*. Van Nostrand Reinhold, New York, 1958.

[19] V. Jagodnik, G.Jelenić, and Ž.Arbanas. On application of mixed finite element approach to beam soil interaction. *Acta Geotechnica Slovenica*, 10 (2):15 – 27, 2013.

[20] N.R. Patra and P.J. Pise. Ultimate lateral resistance of pile groups in sand. *Journal of Geotechnical and Geoenvironmental Engineering*, 127(6):481–487, 2001.

[21] G.G. Meyerhof, S.K. Mathur, and A.J. Valsangkar. Lateral resistance and deflection of rigid walls and piles in layered soils. *Canadian Geotechnical Journal*, 18(2):159–170, 1981.

[22] E. Absi and J. Kerisel. *Active and passive earth pressure tables*. Taylor & Francis, 1990.

[23] B. Broms. Lateral resistance of piles in cohesionless soil. *Journal of the Soil Mechanics and Foundation Engineering*, 90(3):123–156, 1964.

[24] M. McVay, R. Casper, and T.I. Shang. Lateral response of three-row groups in loose to dense sands at 3d and 5d pile spacing. *Journal of Geotechnical Engineering*, 121(5):436–441, 1995.

[25] C.S. Desai, K.G. Sharma, G.W. Wathugala, and D.B. Rigby. Implementation of hierarchical single surface δ0 and δ1 models in finite element procedure. *International Journal for Numerical and Analytical Methods in Geomechanics*, 15(9):649–680, 1991.

[26] G.W. Blaney, E. Kausel, and J.M. Roesset. Dynamic stiffness of piles. In *Proceedings of 2nd International Conference on Numerical Methods in Geomechanics*, pages 1001–1012, 1976.

[27] E. Kausel. Forced vibrations of circular foundations on layered media. Research Report R 74-11, Civil Engineering Department, MIT, 1974.

[28] J.L. Briaud. Sallop: Simple approach for lateral loads on piles. *Journal of Geotechnical and Geoenvironmental Engineering*, 123(10):958–964, 1997.

[29] S. Prakash. *Behavior of pile groups subjected to lateral load*. PhD thesis, University of Illinois, 1962.

[30] H.G. Schmit. Group action of laterally loaded bored piles. In *Proceedings of the X. International Conference, Soil Mechanics and foundation Engineering, Stockholm, Sweden*, pages 833–837, 1981.

[31] H.G. Schmit. Group action of laterally loaded bored piles. In *Proceedings of the XI. International Conference, Soil Mechanics and foundation Engineering, San Francisco, California*, pages 1569–1573, 1985.

[32] E. Franke. Group action between vertical piles under horizontal loads. In *Proceedings of the I. International Geotechnical Seminar on Deep Foundations on Bored and Auger Piles, Ghent, Belgium*, pages 83–93, 1988.

[33] D.A. Brown, C. Morrison, and L.C. Reese. Lateral load behavior of pile group in sand. *Journal of Geotechnical Engineering*, 114(11):1264–1276, 1988.

[34] K. Rollins, K. Peterson, and T. Weaver. Lateral load behavior of full-scale pile group in clay. *Journal of Geotechnical and Geoenvironmental Engineering*, 124(6):468–478, 1998.

[35] T. Shibata, A. Yashimi, and M.Kimura. Model tests and analysis of laterally loaded pile groups. *Soils and Foundations, Japanese Society for Soil Mechanics and Foundation Engineering*, 29(1):31–44, 1989.

[36] K.M. Rollins, J.D. Lane, and T.M. Gerber. Measured and computed lateral response of a pile group in sand. *Journal of Geotechnical and Geoenvironmental Engineering*, 1(131):103–114, 2005.

[37] S.A. Ashford, K.M. Rollins, California. Dept. of Transportation. Engineering Service Center, Structural Systems Research Project, and San Diego. Dept. of Structural Engineering University of California. *TILT: The Treasure Island Liquefaction Test*. Structural Systems Research Project. Division of Structural Engineering, University of California, San Diego, 2002.

[38] J.E. Bowles. *Foundation analysis and design*. McGraw-Hill, 2001.

[39] D.M. Wood. *Geotechnical modelling*. Spon Press, 2004.

[40] K. Terzaghi. Evaluation of coeddicients of subrade reaction. *Geotechnique*, 5(4):41–50, 1955.

[41] M.A. Biot. Bending of infinite beams on an elastic foundation. *Journal of Applied Mechanics*, 57(203):A1–7, 1937.

[42] A. Vesić. Beams on elastic subgrade and the Winkler's hypothesis. In *Proceedings of 5th International Conference on Soil Mechanics and Foundation Engineering*, volume 1, pages 845–850, Michigan, 1961. University of Michigan.

[43] J.S. Horvath. Modulus of subgrade reaction: new perspective. *Journal of Geotechnical Engineering*, 109(12):1591–1596, 1983.

[44] J.S. Horvath. Subgrade models for soil-structure interaction analysis. In *Foundation Engineering: Current Principles and Practices*, pages 599–612, Illinois, 1989. ASCE.

[45] A.T. Daloglu and C.V.G. Vallabhan. Values of *k* for slab on Winkler foundation. *Journal of Geotechnical and Geoenvironmental Engineering*, 126(5): 463–471, 2000.

[46] C.V.G. Vallabhan and Y.C. Das. Parametric study of beams on elastic foundations. *Journal of Engineering Mechanics*, 114(12):2072–2082, 1988.

[47] C.V.G. Vallabhan and Y.C. Das. Modified Vlasov model for beams on elastic foundations. *Journal of Geotechnical Engineering*, 117(6):956–966, 1991.

[48] E. Winkler. *Die Lehre Von Der Elastizizat Und Festigkeit*. Dominicus, Prague, 1867.

[49] A.M. Dodds and G.R. Martin. Modeling pile behavior in large pile groups under lateral loading. Technical report mceer-07-0004, University of Southern California, April 2007.

[50] American Petroleum Institute. Production Dept. *API Recommended Practice*. API Recommended Practice. The Institute, 1993.

[51] Det Norske Veritas. Foundation – clasification notes no 30.4. Technical report, Det Norske Veritas Classification, 1992.

[52] D. Mindlin. Force at a point in the interior of a semi-infinite solid. *Physics*, 7:195–202, 1936.

[53] G. Gazetas. *Foundation vibrations*, chapter 15, pages 553–593. Van Nostrand Reinhold, New York, 1991.

[54] T.G. Davies and M. Budhu. Non-linear analysis of laterally loaded piles in heavily overconsolidated clay. *Geotechnique*, 36(4):527–538, 1986.

[55] H.G. Poulos and T.G. Davies. *Pile foundation analysis and design*. Wiley, New York, 1980.

[56] M. Budhu and T.G. Davies. Analysis of laterally loaded piles in soft clays. *Journal of Geotechnical Engineering*, 114(11):1261–1276, 1988.

[57] N.M. Saḋon. *Full scale static and dynamic lateral Loading of a Single Pile*. PhD thesis, The University of Auckland, January 2012.

[58] P. Tong and J.N. Rossettos. *Finite element method: Basic technique and implementation*. Dover Publications, Incorporated, New York, 2008.

[59] K.J. Bathe. *Finite element procedures*. Prentice-Hall, New Jersey, 1985.

[60] O.C. Zienkiewicz and R.L. Taylor. *The finite element method for solid and structural mechanics*. Elsevier Butterworth-Heinemann, Oxford, 2005.

[61] C. Johnson. *Numerical solutions of partial differential equations by the finite element method*. Dover Publications, Incorporated, New York, 1987.

[62] C.S. Desai and T. Kundu. *Introductory finite element method*. Taylor and Francis, London, 2001.

[63] D.M. Potts and L. Zdravković. *Finite element analysis in geotechnical Engineering: Theory & Application*. Thomas Telford Limited, London, 2001.

[64] E.A. de Souza Neto, D. Peric, and D.R.J. Owen. *Computational methods for plasticity: Theory and applications*. Wiley, London, 2011.

[65] S. Nordal. Soil modeling. Technical report, NTNU Trondheim, 2012.

[66] M. Eisenberger and D.Z. Yankelevsky. Exact stiffness matrix for beams on elastic foundation. *Computers and Structures*, 21(6):1355–1359, 1985.

[67] O. C. Zienkiewicz and R. L. Taylor. *The finite element method. Its basis and fundamentals*. Elsevier Butterworth-Heinemann, Oxford, 2005.

[68] M. Šušnjara, J. Bukovac, L. Nikler, I. Crnolatac, A. Milan, and D. Šikić. Basic geological map 1:100000, in Croatian. Crikvenica part, Confederation gelogical department, Belgrade, 1970.

[69] D. Šikić, M. Pleničar, and M. Šparica. Basic geological map 1:100000, in croatian. Ilirska Bistrica part, Institute for geological research, Zagreb - Federal gelogical department, Belgrade, 1972.

[70] Ž. Vulić and B. Biondić. Seismic microrajonization of Rijeka. Book 2 - geological and engineering-geological works, in Croatian, 1974.

[71] Civil engineering institute. Engineering geological characteristic of rocks and soils in Primosko-Goranska district, in Croatian. IGH PC Rijeka, 1997.

[72] B. Biondić and F. Dukarić. Basic hydrogeological map of Croatia 1:100000, in Croatian. Rijeka part, Institute for geological research, Zagreb, 1997.

[73] V. Jagodnik. Field test planing for performing laterally loaded piles (in Croatian). Seminar, Faculty of Civil Engineering, University of Rijeka, 2011.

[74] BS EN. $933 - 1 : 2012$ - Tests for geometrical properties of aggregates. Determination of particle size distribution. Sieving method. Technical report, BSI, London, 2012.

[75] R.D. Holtz, W.D. Kovacs, and T.C. Sheahan. *An introduction to geotechnical Engineering*. Prentice Hall, New York, 2 edition, 2010.

[76] F. Azizi. *Applied analyses in aeotechnics*. Spon, London, 2000.

[77] B.M. Das. *Principles of geotechnical engineering*. Cengage Learning, 2010.

[78] E. Nonveiller. *Soil mechanics and foundation engineering (in Croatian)*. Školska knjiga, Zagreb, 2nd edition, 1990.

[79] V. Yazdanjou, S.N.S. Eshkevari, and A. Hamidi. Effect of gravel content on the shear behavior of sandy soils. In *The 4th National Conference on Civil Engineering*, Teheran, Iran, 2008. University of Teheran.

[80] I. Alpan. The geotechnical properties of soils. *Earth-Science Reviews*, 6 (1):5–49, 1970.

[81] U. Smoltczyk. *Geotechnical engineering handbook: Fundamentals*. Ernst and Sohn, Berlin, 2002.

[82] M.D. Bolton. The strength and dilatancy of sand. *Geotechnique*, 36(1): 65–78, 1986.

[83] G.T. Houlsby. How the dilatancy of soil affects their behaviour. Report 121/91, University of Oxford, 1991.

[84] D.M. Wood. *Soil behaviour and critical state soil mechanics*. Cambridge University press, 1991.

[85] A. Boghrat. Sound barrier wall foundations in granular material. *Transp.Res.Rec.*, 1288:158 – 167, 1990.

[86] S.S. Lin and J.C. Liao. Lateral response evaluation of single piles using inclinometer data. *Journal of Geotechnical and Geoenvironmental Engineeing*, 132(12):1566–1573, 2006.

[87] G.H. Hardy. *Divergent series*. American Mathematical Society, 1991.

[88] G.A.F. Seber and C.J. Wild. *Nonlinear regression*. Wiley Series in Probability and Statistics. Wiley, London, 2003.

[89] S. Wolfram. *The Mathematica ® Book, Version 4*. Cambridge University Press, Cambridge, 1999.

[90] A. Cividini, L. Jurina, and G. Gioda. Some aspects of characterization problems in geomechanics. *International Journal of Rock Mechanics and Mining Sciences & Geomechanics Abstracts*, 18(6):487 – 503, 1981.

[91] G. Gioda and G. Maier. Direct search solution of an inverse problem in elastoplasticity: Identification of cohesion, friction angle and in situ stress by pressure tunnel tests. *International Journal for Numerical Methods in Engineering*, 15(12):1823–1848, 1980.

[92] M. Reza Arta. *The behavior of laterally loaded two-pile groups*. PhD thesis, University of Durham, 1992.

[93] Rocscience. *RS 3 - Rock and soil 3D user's manual*. Toronto, 2013.

[94] I. Džeba, B. Andrioć, and D. Dujmović. *Steel constructions 3 - Fast calculations according to Eurocode3, (in Croatian)*. Školska knjiga, Zagreb, 1998.

[95] B. Padovan and M.Maričić. Geophyscal investigation report (in Croatian). Technical report, Geoarheo, Zagreb, 2013.

[96] H. Gebrande and H. Miller. Refraktionsseismik. In F.Bender, editor, *Angewandte Geowissenschaften II*, pages 226–260, Stuttgart, 1985. Ferdinand Enke.

[97] B. Gibson, M. Odegard, and G. Sutton. Nonlinear least-squares inversion of traveltime data for a linear velocity-depth relationship. *Geophysics*, 44 (2):185–194, 1979.

[98] C.B. Park. Characterization of geotechnical sites by multichannel analysis of surface waves. In *Proceedings of the Korean Ground Society*, Seoul, Korea, 1995.

Curriculum Vitae

Ime i prezime: Vedran Jagodnik
Datum i mjesto rođenja: 28. kolovoza 1983., Rijeka
Adresa: Put Bože Felkera 18, Rijeka
Telefon: 051 265 934/ 091 584 83 35
E-mail: vedran.jagodnik@gradri.uniri.hr

OBRAZOVANJE

2002. *Građevinski fakultet Sveučilišta u Rijeci*, Dodiplomski studij: Konstruktorsko usmjerenje, stečena diploma: Diplomirani inženjer građevinarstva

2007. *Građevinski fakultet Sveučilišta u Rijeci, Poslijediplomski doktorski studij*

2010. *International school for Landslide Risk assessment and Mitigation (LARAM)*, Salerno

2010. *E-učenje u nastavnom procesu, potvrda o završenom programu cijeloživotnog obrazovanja*, IT akademija Sveučilišta u Rijeci

2011. *Tromjesečni boravak na stranom sveučilištu*, University of California, Los Angeles, SAD

2012. *Kolegij **Soil Modeling** na NTNU, Norwegian Univeristy of Science and Technology*, Trondheim, Norveška

RADNO ISKUSTVO

2007. *Građevinski fakultet Sveučilišta u Rijeci*, Katedra za geotehniku, znanstveni novak, asistent

NAGRADE/POSTIGNUĆA

Gradska stipendija 2002. - 2007. g.

Diplomski rad: "*Analiza naprezanja i deformacije stambeno poslovog objekta Stari grad- Rijeka*", mentor: prof. dr. sc. Željko Arbanas

KOMPETENCIJE

Računalne: MS Office (Word, Excel, Power Point); AutoCAD; Programski paket Geostudio (SLOPE/W, SIGMA/W, SEEP/W, QUAKE/W); Programski paket Rockscience (Slide, Phase2, RocPlane, Swedge, RS3); LaTeX; Mathematica;

Strani jezici: engleski jezik (aktivno)

OSTALO

- znanstveni interesi iz područja mehanike tla, geotehničkog inženjerstva, dinamike tla, numeričkog modeliranja -dodatni podaci: www.gradri.uniri.hr

- rad na hrvatsko-japanskom bilateralnom znanstvenom projektu "Risk Identification and Land-Use Planning for Disaster Mitigation of Landslides and Floods in Croatia" od 2008. do 2013.g.

- sudjelovanje na brojnim domaćim i međunarodnim kongresima, radionicama i savjetovanjima, znanstvenim i stručnim susretima oralnim prezentacijama i poster prezentacijama; popis objavljenih radova: http://bib.irb.hr/